ABSTRACT

Power Distribution Feeder Response to the Asymmetric Saturation of
Substation Transformers Caused by Significant High-Side DC Currents

Christopher D. Weldy, Ph.D.

Mentor: Mack Grady, Ph.D.

High-altitude electromagnetic-pulse and geomagnetic disturbances can lead to asymmetric saturation of utility transformer cores by causing significant DC current to flow through the transformer windings. Transformer secondary voltage and current waveforms are distorted by core saturation and this distortion can be amplified at points on power distribution feeders where circuit topologies create series or parallel resonances. The performance of distribution feeders during asymmetric core saturation is explored in this work using harmonic powerflow simulation. A harmonic voltage source model is developed to represent steady-state transformer secondary terminal response during DC current flow in the primary windings. The model performance is compared to field test measurement data and then used to simulate the energization of realistic electric power distribution feeder models. The response of the feeder models is compared to industry standards of power quality.

Power Distribution Feeder Response to the Asymmetric Saturation of Substation Transformers Caused by Significant High-Side DC Currents

by

Christopher D. Weldy, B.S., M.S.

A Dissertation

Approved by the Department of Electrical and Computer Engineering

____

Kwang Y. Lee, Ph.D., Chairperson

Submitted to the Graduate Faculty of
Baylor University in Partial Fulfillment of the
Requirements for the Degree
of

Doctor of Philosophy

Approved by the Dissertation Committee

____

W. Mack Grady, Ph.D., Chairperson

____

Annette von Jouanne, Ph.D.

____

Scott Koziol, Ph.D.

____

Mike Thompson, Ph.D.

____

Alex Yokochi, Ph.D.

Accepted by the Graduate School

May 2023

____

J. Larry Lyon, Ph.D., Dean

Page bearing signatures is kept on file in the Graduate School.

TABLE OF CONTENTS

LIST OF FIGURES

LIST OF TABLES

ACKNOWLEDGMENTS

After several years of pursuing graduate education while working full time, I first and foremost thank my wife, Lydia. Despite my endless late nights, always carrying work along, and converting our house into a small library, she provided the encouragement that kept me going and the wisdom to correct my circular reasoning. Her sacrifice enabled me to succeed.

I thank my advisor, Dr. Mack Grady, for the opportunity to work on this project and for his guidance through the years. When I reached out looking to grow as an engineer, he brought me on to his team without hesitation and I would not have made it this far without him. I appreciate the assistance of, and discussions with, DTRA and ARA. I thank my committee for serving on this team and for the critical review and discussion of my work. I thank Dr. Annette von Jouanne for providing practical advice on doing research, and for sharing her insight on education and research as a career.

I thank Minnie Simcik for her tireless effort in working behind the scenes to keep me on a successful path. I am especially thankful for her never-failing positive attitude. Minnie's encouragement always seems to come at just the right time.

DEDICATION

To Otto, Meri, and Ned.

CHAPTER ONE

Introduction

Background

The electric power system plays a vital role in the economy, the daily lives of people, and the reliability of national infrastructure. Reliability is a primary driver for the design and operation of power systems, but power systems are exposed to threats including storms, natural disasters, and attacks. For example, a geomagnetic disturbance (GMD) in 1989 caused a blackout of the Hydro-Quebec power system and resulted in significant equipment damage [1]. More recently, winter storm Uri in 2021 caused major disruption of electric power generation in Texas that strained operation of the ERCOT power system [2].

The development of nuclear weapons presented a new threat to electric power systems through the effects of high-altitude nuclear detonation. The late-time component of high-altitude electromagnetic pulse (E3) causes a temporary change in the Earth's magnetic field and produces an electric field on the earth's surface that induces direct current in the electric power system through grounded points [3]. While E3 and GMD both produce fields that affect power systems in a similar way, GMD fields are usually treated as approximately uniform. E3 produces complex field patterns with higher intensity for a shorter duration, which can be seen in [4].

Asymmetric saturation of utility transformer cores can be caused by E3 and GMD and the distortion can be amplified at points on power distribution feeders where circuit topologies lead to resonances. This work explores the risk imposed to distribution feeders by the asymmetrical core saturation using harmonic powerflow simulation. The secondary terminal behavior of asymmetrically saturated transformers will be investigated, and then feeder response will be estimated using harmonic powerflow simulation. The simulated electrical response of the feeder models will be compared to industry standards of power quality to characterize their response.

Literature Review

AC Power Systems and DC Current

Transformers are used in the electric power delivery system (EPDS) to convert power from one voltage level to another. Power transformers couple one or more electrically separate windings on a common magnetic core. In the ideal case, the ratio of primary to secondary voltage is equal to the turns-ratio of the primary and secondary windings, and the ratio of primary to secondary current is equal to the reciprocal of the turns-ratio. Transformation is necessary because AC electric power is generated and consumed at lower voltages to minimize equipment cost, while it is transmitted at higher voltages to minimize power losses in the EPDS.

Magnetic cores are designed to use a minimum amount of material for economic reasons, so even a slight voltage offset can result in partial saturation of the core. When saturation occurs the voltage waveforms become distorted, which can be significant on the secondary winding [5]. Figure 1.1 shows an example secondary voltage waveform measured during asymmetric saturation of a wye-delta transformer during field tests, normalized to the pre-saturation crest peak value. The plot includes the secondary voltage for an ideal transformer for reference. The distorted secondary voltage is a source of harmonics in the downstream circuits.

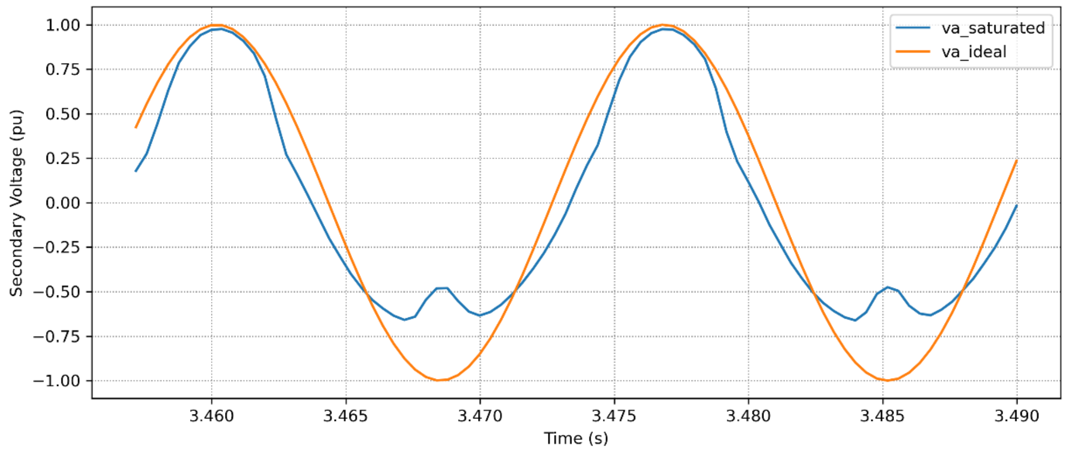

Figure 1.1.-Example asymmetrically saturated transformer secondary voltage waveform with ideal sinusoid for reference.

Transformer saturation occurs naturally in power systems during transformer energization, but the duration is typically much shorter than would be expected for an E3 event. DC current driven by E3 can last for over one minute and impact multiple transformers at the same time [4]. Similar transformer responses have been reported for transformers during GMD events [6].

A nuclear detonation at high altitude generates an electromagnetic pulse (HEMP) that produces electric and magnetic fields that interact with the EPDS [7]. HEMP interaction with the EPDS is driven by interaction of charged particles with the earth's magnetic field that produces an electric field at the surface of the Earth and induces voltage across the transmission lines. The electric field oscillates at a frequency much lower than the nominal frequency of the EPDS so the induced voltage can be treated as a

DC voltage for steady-state analysis [7]. Recent publications report that peak electric fields of 85 V/km may be expected for unclassified nuclear device detonation [4].

A DC voltage in series with a transmission line will drive a DC current in each conductor when there is a return path for the DC current to flow. The return path in practical three-phase power systems is through the earth, via points of the power system that are connected to ground. The most common ground points within the EPDS are the grounded neutral point of wye transformer windings. Two transformers with wye-grounded points and the associated return path through the earth are illustrated in Figure 1.2.

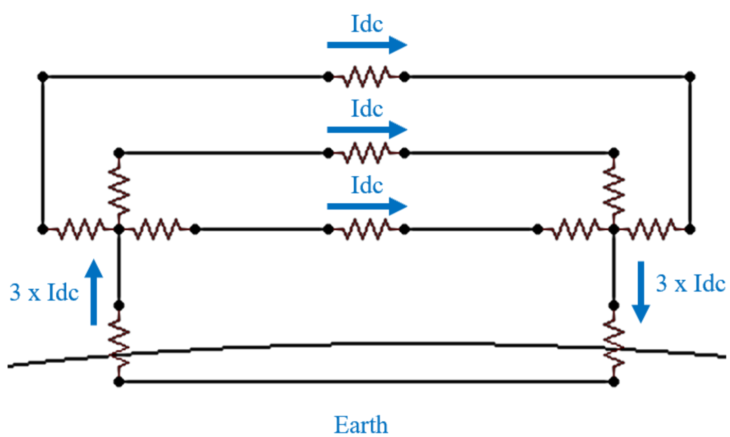

Figure 1.2.-GIC circuit diagram.

In practice, the line resistance is small and the two transformers may be separated by many miles, so large DC currents can be developed. The resistance of the ground point will influence the DC current magnitude. While the resistivity of soil is high compared to that of conductors used in the EPDS, the cross-sectional area of the earth is large enough that the effective resistance of the earth is relatively low at each connection point. Figure 1.3 shows the effective resistance of a ground connection with respect to return depth for two sizes of spherical ground connections and soil resistivities using the calculation presented in [8], represented by the following.

$$R(depth) = \frac{\rho}{2\pi}\left(\frac{1}{r_{ground-point}} - \frac{1}{depth}\right) \tag{1.1}$$

The plot shows that the size of the ground grid has a big impact on the effective resistance of the connection. However, even with a relatively high soil resistivity of 200 ohm-meters and a small ground grid, the resistance of the earth approaches an asymptote beyond a depth of about 100 meters.

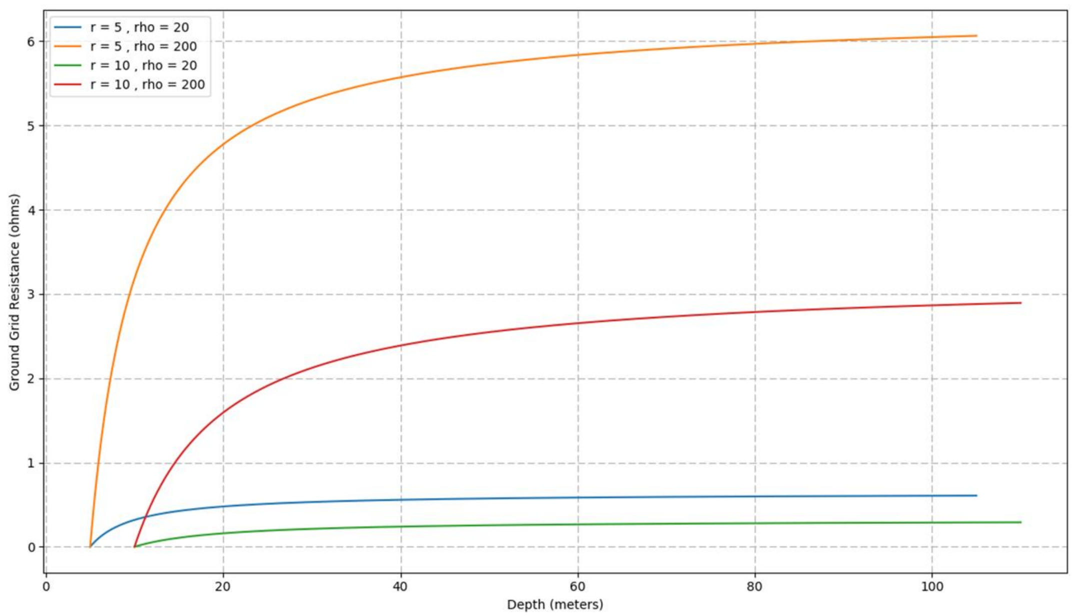

Figure 1.3.-Effective resistance of ground connection with respect to depth of earth.

The ground points allow the circuit to be closed through the earth so that DC current flows through the transmission line conductors. The DC current usually passes through a power system element that uses a magnetic core to function.

Research on the impact of GIC to transmission systems has included low transmission system voltages due to increased VAR demand of saturated transformers in [9], [10], overvoltage and interrupt capabilities of breakers in [11], and harmonic voltage distortion and its impacts in a nuclear power plant in [12]. EPRI research into the impacts of GIC resulting from geomagnetic storms, which cause similar but weaker electric fields, reported that the distribution system would contribute minor additional risk to the system and recommended to focus on transmission level evaluation [13]. However, it is reported in [7] that small GIC currents can have a significant impact on the distribution system, and even at 20V/km a reasonably short feeder can have enough GIC to cause harmonic distortion. Considering that the expected electric field strength in the earth during an E3 event peaks at 85V/km, the impact to feeders may be higher than considered previously. Since load plays a key role in transmission system stability, widespread impacts to the distribution system may have a meaningful impact to the state of the transmission system during an E3 event.

Power Transformers and Circuit Models

A power transformer is formed by two or more electrical windings that are coupled magnetically [14]. Power transformers are used to convert power from one voltage and current base to another. The transformer t-model was presented in [15] to represent the terminal behavior of a two-winding transformer. A diagram of the single-phase t-model is shown in Figure 1.4. The primed labels indicate secondary quantities that are referred to the primary winding in the diagram.

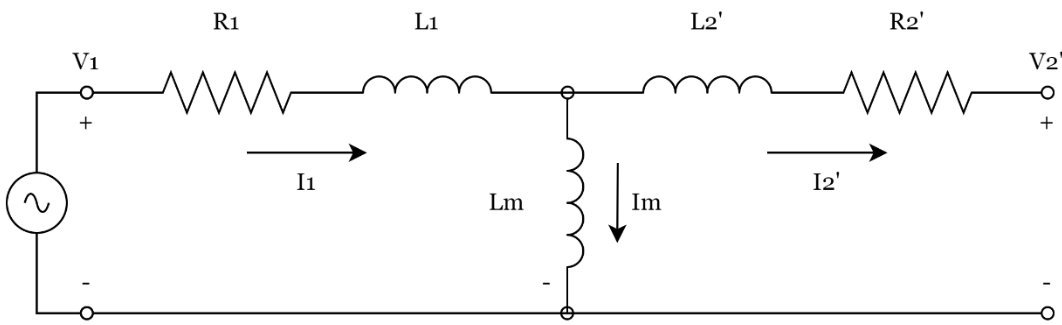

Figure 1.4.-Steinmetz t-model circuit diagram with secondary values referred to the primary.

The time-domain behavior of the t-model with an open secondary (V2’ terminal) is described by the following differential equation developed using KVL and the voltage relation of the resistor and inductor components [14].

$$\mathrm{V1(t)} - \mathrm{R1} \cdot \mathrm{I1(t)} - (\mathrm{L1} + \mathrm{Lm}) \cdot \frac{\mathrm{d}}{\mathrm{dt}} \mathrm{I1(t)} \ = \ 0 \tag{1.2}$$

If the transformer is energized on the primary (V1 terminal) by an ideal voltage source, the differential equation can be solved for the primary current I1(t). The exact solution of this differential equation was obtained using Mathematica software as the following, where V1(t) is assumed to be an ideal cosine function at system frequency.

$$I1(t) = \frac{\mathrm{V1}\, e^{-\frac{\mathrm{R1}\, t}{\mathrm{L1}+\mathrm{Lm}}}\left(\mathrm{L1}\; w \sin(tw) e^{\frac{\mathrm{R1}\, t}{\mathrm{L1}+\mathrm{Lm}}} + \mathrm{Lm}\; w \sin(tw) e^{\frac{\mathrm{R1}\, t}{\mathrm{L1}+\mathrm{Lm}}} + \mathrm{R1} \cos(tw) e^{\frac{\mathrm{R1}\, t}{\mathrm{L1}+\mathrm{Lm}}} - \mathrm{R1}\right)}{\mathrm{L1}^2\, w^2 + 2\, \mathrm{L1}\; \mathrm{Lm}\; w^2 + \mathrm{Lm}^2\, w^2 + \mathrm{R1}^2} \tag{1.3}$$

To solve the differential equation approximately using the fourth-order Runge-Kutta (RK4) algorithm [16], the equation is rearranged into the following form.

$$\mathrm{I1}'(t) = \frac{\mathrm{V1} \cos(wt) - \mathrm{R1}\; \mathrm{I1}(t)}{\mathrm{L1}+\mathrm{Lm}} \tag{1.4}$$

Figure 1.5 compares the exact and approximate solutions of the primary current, I1(t) for the t-model with an open secondary terminal and nominal parameters. The RK4 algorithm provides a reasonable estimate of the solution.

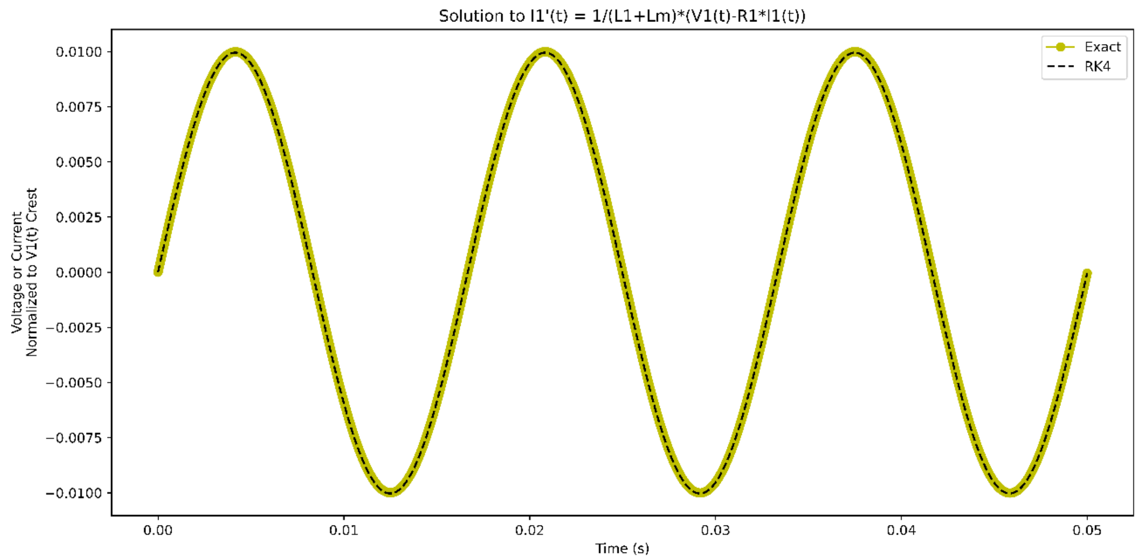

Figure 1.5.-Exact versus RK4 approximation of I1(t) for Steinmetz t-model with open secondary terminal.

An applied voltage across the winding causes magnetizing current to flow, which produces the flux-linkage (λ) necessary to balance the applied voltage, according to the following relation [17].

$$V_{\mathrm{m}} = \frac{\mathrm{d}}{\mathrm{dt}}\lambda_m \tag{1.5}$$

Flux-linkage is the product of the number of turns and the magnetic flux [8]. Since the transformer winding can also be treated as an inductor, Equation 1.5 can be equated with the inductor voltage-current relation and solved for the inductance, as shown here.

$$\mathrm{L} = \frac{\mathrm{d}\lambda_m}{\mathrm{dI}_m} \tag{1.6}$$

Equation 1.6 can be used to estimate the magnetizing current of a transformer given the excitation voltage and inductance of the core, including transformers that have nonlinear inductance.

If the magnetizing component of the t-model is replaced by a nonlinear element, the circuit becomes more difficult to solve. Nonlinear circuit solution techniques have been explored widely in the electronics discipline, and methods similar to those found in [18], [19], and [20] will be used to approximate the steady-state solution to the nonlinear t-model circuit later. These methods combine time-domain and frequency-domain circuit solution techniques in attempt to estimate the steady-state behavior.

In large scale power systems, both three-phase and single-phase transformers are commonly used. There are several types of transformers covering a range of electric and magnetic configurations. Wye-grounded and delta electrical connections are common and core-form and shell-form magnetic cores are common. Wye-grounded transformers electrically connect the power system to the earth. Under normal balanced conditions, very little current flows through this connection.

The diversity of equipment in electric power systems makes comprehensive studies across all configurations impractical. Instead, some typical parameter ranges will be used during this assessment. Reference [21] reported a typical reactance range of 5% to 15% and a typical X-over-R ratio range of 5 to 50. Reference [22] reported a typical nominal exciting current range of 0.3% to 1% for large power transformers. Reference [23] reported a typical core saturation knee point range of 1.15 per unit to 1.25 per unit, and a rule of thumb that the air core reactance is twice the leakage reactance, for when the value is not known. A range of 1.7 to 2.3 times the leakage reactance will be used for the air core reactance in this work to account for variation. It will also be assumed that the per unit impedance of the transformer is split equally between the primary and secondary windings, following [21].

Asymmetric Saturation of Transformers

The permeability of a material determines its influence on the magnetic flux density in the vicinity of an electric current [17]. A higher permeability produces higher flux density for a given current, so the flux produced by a current is more concentrated in the surrounding material that has higher permeability. Transformer windings are typically wrapped around a core with high permeability so that the magnetic flux is confined to a specific area [17]. This allows a high degree of magnetic coupling between the transformer windings. While the magnetic core improves the coupling, it can introduce complications if the core saturates. Transformer saturation occurs when the atomic dipoles inside the magnetic core have fully aligned with the applied magnetic field [24]. Beyond this point, the core no longer provides improved magnetic field density over that of air. Asymmetric saturation is saturation that occurs on either the positive or negative half-cycle, but not both.

Reference [25] presented a fundamental method for estimating the transformer exciting current response to GIC current flowing in the transformer neutral, which was validated against measured response for an occurrence of 10 amps per phase of GIC in the BC Hydro System. Reference [26] summarized the boundary conditions of this method, per unitized the calculations, and calculated response values up to 0.3 per unit GIC per phase, where the highly non-linear harmonic magnitude variation as a function of GIC is visible for the first five harmonics. These provide a method for estimating the steady-state transformer exciting current in response to DC current flowing through the transformer windings, using a straight line approximating the air-core inductance. In later chapters, the flux-linkage current relationship provided in [5] is combined with the method in [25] and [26] to produce a magnetizing current response to DC current that is more favorable for the numerical computations that will be used to solve the nonlinear t-model circuit. DC current flowing in the transformer windings biases the flux linkage and causes asymmetric saturation of the core.

Waveform Distortion and Harmonics

Distortion of power system signals is a deviation from the ideal sinusoid that is desired and can be interpreted as the superposition of multiple sinusoids of different frequencies that are integer multiples of the fundamental frequency. Large power systems are designed to provide sinusoidal voltage at several voltage levels with a fixed frequency. In the ideal case, the voltage provided at any point in the power system can be represented by a sine or cosine function such as the following.

$$V_{inst} = \sqrt{2} \times V_{rms} \times cos(\omega t + \theta) \tag{1.7}$$

Figure 1.6 shows three cycles of instantaneous line-to-ground voltage for one phase of a 25 kV line-line 60 Hz system created using the cosine function.

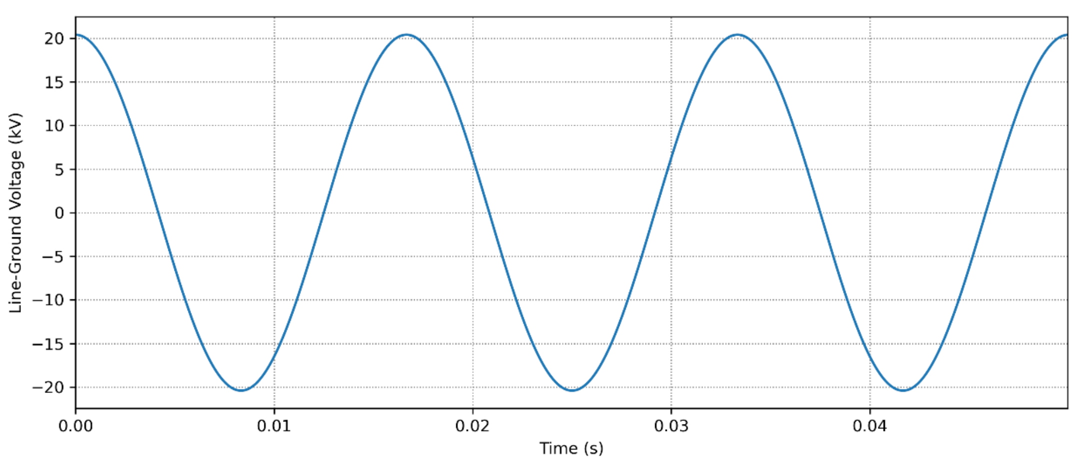

Figure 1.6.-Ideal 60 Hz voltage signal.

Harmonics can be understood as sinusoids within a signal oscillating at frequencies that are integer multiples of the nominal frequency of the signal. For example, consider the two signals in Figure 1.7. The blue signal shows the line-ground voltage for the 25 kV line-line 60 Hz system computed by the following.

$$V_1 = \sqrt{2} \times \frac{25}{\sqrt{3}} \times cos(2\pi 60t) \tag{1.8}$$

The orange signal shows a 2nd harmonic that is 25% of the fundamental frequency voltage with a phase shift of thirty degrees computed by the following.

$$V_2 = 0.25 \times \sqrt{2} \times \frac{25}{\sqrt{3}} \times cos(2\pi 120t \ + \ 30°) \tag{1.9}$$

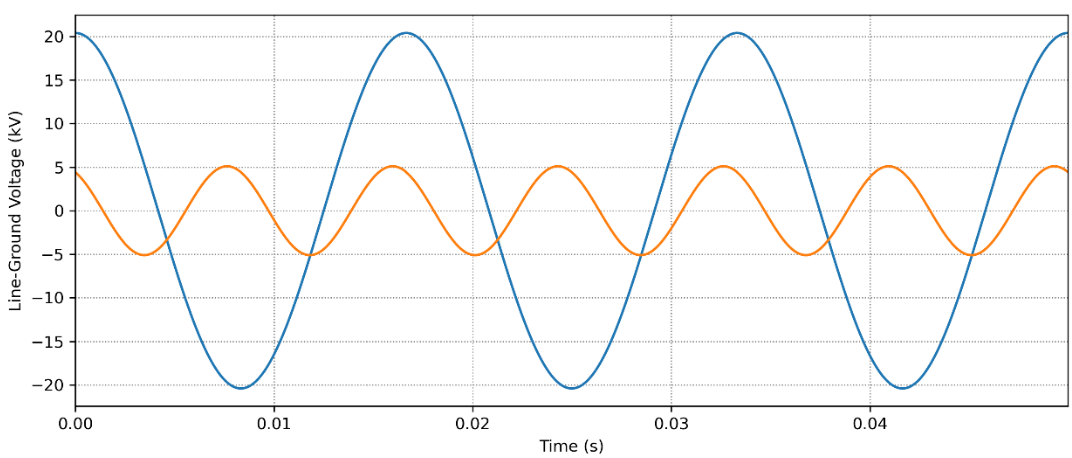

Figure 1.7.-Ideal 60 Hz and 120 Hz voltage signals.

Even though the plots in Figure 1.6 and Figure 1.7 appear to be continuous, each line is formed by a collection of samples at discrete times. Superposition of the two signals produces the signal shown in Figure 1.8. This signal could represent the line-to-ground voltage of a single phase within a 25 kV feeder where 25% 2nd harmonic voltage is present. The signal is visibly distorted as compared to the single-frequency sinusoid.

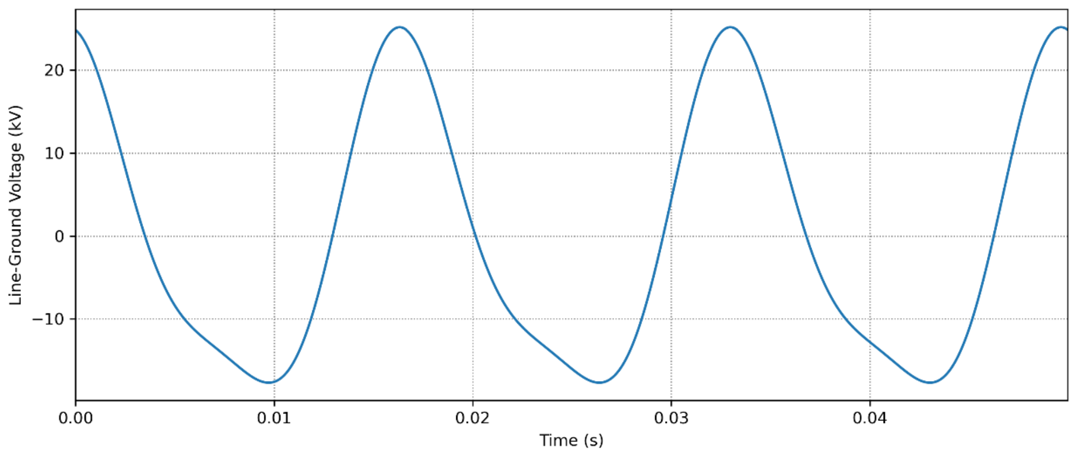

Figure 1.8.-Distorted voltage signal.

Since the signal is comprised of discrete samples, the individual harmonics can be extracted using the Discrete Fourier Transform (DFT) [27]. Taking the sampled signal x[n], the harmonic components X[k] can be computed by the following.

$$X[k] = \sum_{n=0}^{N-1} x[n] W_N^{kn} \tag{1.10}$$

$$W_N = e^{-j(2\pi/N)} \tag{1.11}$$

Application of the DFT to the signal shown in Figure 1.8 for harmonics zero through four produces the spectrum shown in Table *1.1* and summarized Figure 1.9. The values calculated using the DFT match the components used to generate the original signal.

Table 1.1.-Calculated harmonic spectrum of distorted signal.

Harmonic No.	Magnitude (kV Peak)	Angle (Degrees)
0	0	0
1	20.41	0
2	5.1	30
3	0	0
4	0	0

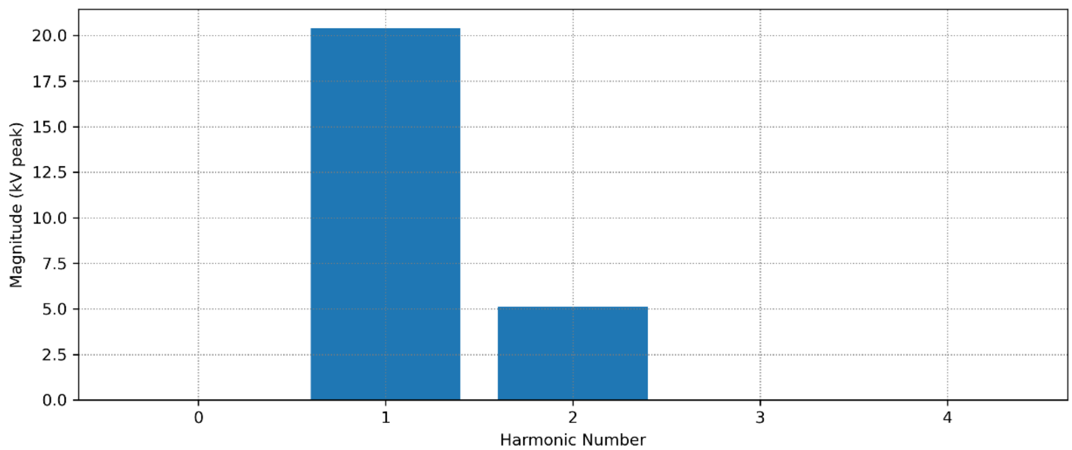

Figure 1.9.-Calculated harmonic magnitudes of distorted voltage signal.

The original signal can be recreated using the Inverse Discrete Fourier Transform (IDFT) [27], computed as follows.

$$x[n] = \frac{1}{N} \sum_{k=0}^{N-1} X[k] W_N^{-kn} \tag{1.12}$$

$$W_N = e^{-j(2\pi/N)} \tag{1.13}$$

Application of the IDFT to the spectrum shown Table *1.1* produces the signal shown in Figure 1.10, where every 30th sample of the original signal is shown as orange dots for reference. The IDFT recreation matches the original signal with no visible difference, where the largest absolute error within the samples computed in this example was 4e-14. The NumPy Python package [28] has forward and inverse Fast-Fourier-Transform functions that will be used to perform the DFT and IDFT in this work.

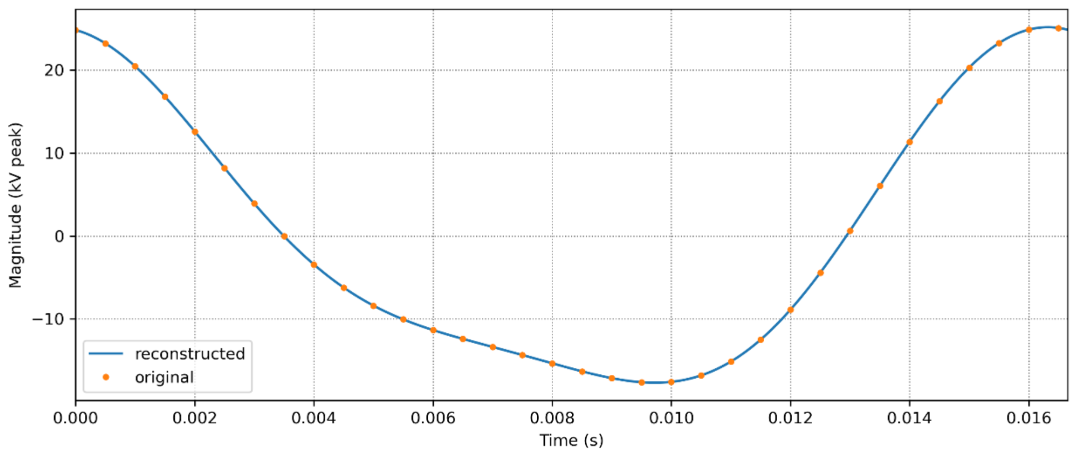

Figure 1.10.-Reconstructed voltage signal and original signal.

Harmonic analysis is one application of the DFT and IDFT commonly used to study distortion in power systems. Harmonic analysis is accomplished by using the DFT to decompose a distorted time-domain signal into harmonic components, using phasors to perform circuit analysis in the frequency-domain for each harmonic, and then using the IDFT to transform the resulting circuit quantities back into the time domain. Harmonic analysis is used in the power industry due to the size of commercial power grids and the significant computation time required for time-domain simulations.

The presence of harmonics in a power system presents the opportunity for resonance issues, especially where capacitor banks are applied. Resonance occurs in a circuit when the inductive reactance and capacitive reactance effectively cancel for a given frequency. For the series RLC circuit shown in Figure 1.11, the current for a given voltage source magnitude will be maximized at the frequency where inductive and capacitive impedances cancel, and this large current will cause maximum opposite-polarity voltages across each of the two elements. In practical power systems the circuit resistance tends to be small, so the current at resonant frequencies can be very high.

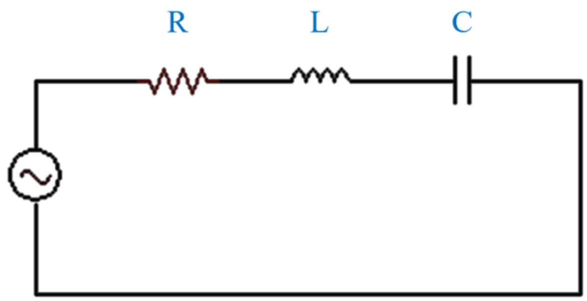

Figure 1.11.-RLC circuit diagram.

Although the total voltage drop in the circuit does not exceed that of the source, the voltage drop across an individual element can exceed the source magnitude. Therefore, resonance can amplify certain voltages within a circuit beyond the magnitude of the source.

Distribution feeders have the potential for resonance and associated voltage amplification in the presence of voltage harmonics because the feeders are primarily inductive and shunt capacitor banks are applied along the feeder to resolve fundamental frequency voltage issues. Resonances within distribution feeders during asymmetric transformer core saturation could lead to equipment damage and load loss.

Power System Simulation and Models

Power system simulation uses numerical solution techniques to solve simultaneous equations that represent the power system. This is done to estimate the behavior of a system under different scenarios. Steady-state analysis, which consists of numerical solution of the power system circuits during a state of periodic equilibrium, will be used for this research. The powerflow equations representing the balance of real and reactive power at each node in the system are used to form a matrix representation of a power system [29].

Solution of the matrix equations is attempted using a numerical method. The powerflow equations are non-linear due to the product of variables and the presence of variables inside of transcendental functions. Analytic solution of non-linear equations is often difficult, so numerical methods are applied in practice. Numerical methods typically involve choosing an estimate for each variable, evaluating the equations at this estimated operating point to quantify the error, and then developing a new estimate based on the observed error. The Newton-Raphson method is commonly used in practice to solve the powerflow equations due to its convergence properties, although some use a hybrid approach by combining multiple techniques.

Harmonic powerflow is an extension of this method for frequencies other than the fundamental. It is computed using the same powerflow formulation, but the network parameters are recomputed for each harmonic frequency and the representation of loads and sources are changed to reflect the expected behavior at each frequency. The resistance, inductive reactance, and capacitive reactance must be recomputed for each network element at the frequency being simulated. The parameter values at the nominal power system frequency are stored in a powerflow database by utilities, and other entities. The constant P, Q values of a load are translated into resistance and inductive reactance at the study frequency. The network is solved for each harmonic independently and the IDFT can be used to obtain time domain signals if necessary.

OpenDSS is an open-source program developed to enable frequency domain simulation of electric power systems and is freely available under the BSD license [30]. OpenDSS uses many of the same representations as other powerflow software, but uses a fixed-point method of solving the equations by default, which is suited to the radial circuits found in distribution systems [31]. The OpenDSS powerflow solution was evaluated for consistency using textbook cases and an alternative program, PCFLO harmonic powerflow software [32]. This was necessary to ensure reasonableness of the numerical solution of OpenDSS and to better understand its general usage.

The load model used by OpenDSS during harmonic simulation is represented as a combination of series RL and parallel RL circuits. When a load is added to an OpenDSS model one available setting is the %SeriesRL parameter, which defines the proportion of the total load that is assigned to the series RL portion of the load circuit. The remaining portion of the load is assigned to a parallel representation. OpenDSS assumes a default setting of 50, which will equally split the load between the series and parallel circuits. The default OpenDSS harmonic load model includes a harmonic current source with a default harmonic spectrum that is injected by the load during a harmonic simulation. To avoid mixing transformer driven harmonics and default load model harmonics, each load harmonic injection is set to zero in this work. Therefore, the current source portion of the OpenDSS load model is open circuited for this work.

The load model assumptions are expected to have a large impact on the powerflow solution. To illustrate this, the harmonic current flowing into a load was evaluated against the range of settings for the %SeriesRL parameter. The impact of the %SeriesRL setting was evaluated using the test circuit shown in Figure 1.12, where the load value was selected to draw 100 amps at nominal voltage and frequency. The voltage source is set to provide 1 per unit voltage at each harmonic frequency. The line impedance is selected to be sufficiently small to avoid influencing the harmonic current flows.

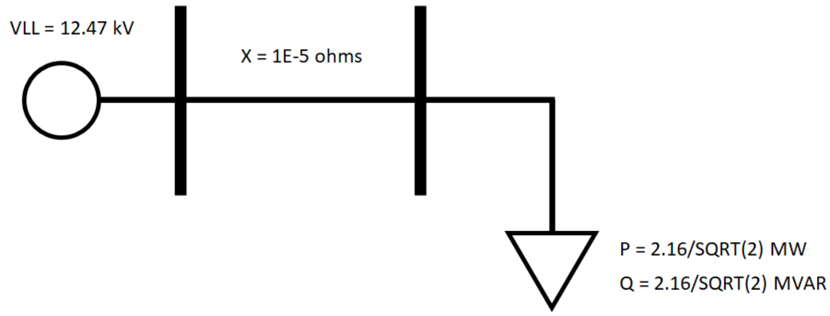

Figure 1.12.-Oneline diagram of a load with real and reactive power.

The load current for this circuit was simulated across the range of %SeriesRL settings for harmonic numbers 1 through 20 and the simulation results are shown in Figure 1.13. The simulation results show that the current flowing into the load decreases with increasing harmonic number, and that a lower %SeriesRL setting results in more harmonic current flowing into the load.

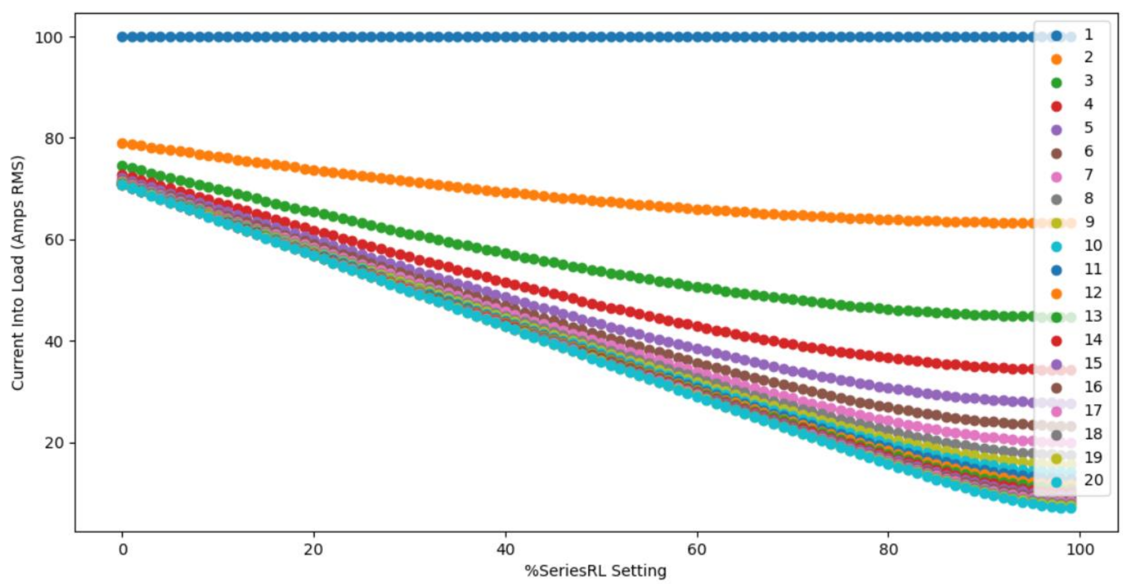

Figure 1.13.-OpenDSS simulated load current for harmonics 1 through 20 with respect to %SeriesRL setting.

Distribution feeders are the circuits that connect most electric loads to the EPDS with exceptions including industrial and commercial loads that connect to the transmission system. A distribution feeder consists of three-phase primary conductors that originate in a substation on the secondary side of a power transformer. The three-phase conductors then spread out geographically to reach consumers that require three-phase power. Single-phase laterals further spread out to reach consumers that only require single-phase power. One goal of the distribution system designer and operator is to balance the load across the three-phases.

Some realistic power system models have been developed and released publicly to support power systems research. The analysis will focus on three publicly available distribution system models. These include the EPRI CKT5, CKT7, and CKT24 models that are included during installation of OpenDSS, in OpenDSS format within the software examples. These distribution system models provide a three-phase representation of their respective distribution systems. A geographical oneline diagram for each distribution model is shown in Figure 1.14 through Figure 1.16.

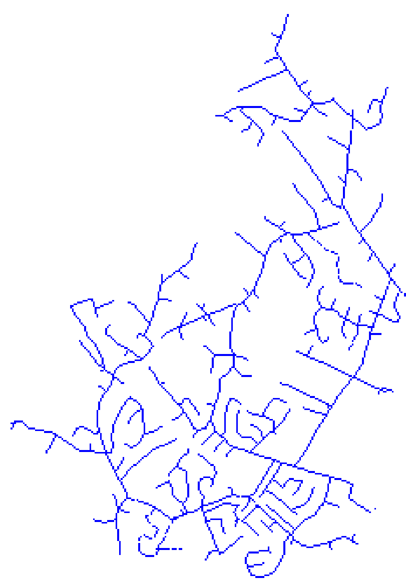

Figure 1.14.-Oneline diagram of the EPRI CKT5 model generated using OpenDSS.

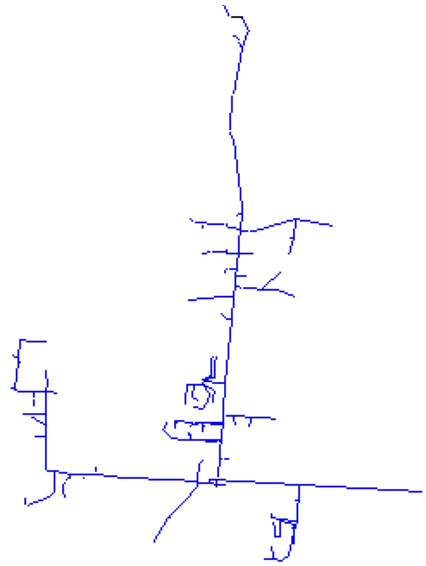

Figure 1.15.-Oneline diagram of the EPRI CKT7 model generated using OpenDSS.

Figure 1.16.-Oneline diagram of the EPRI CKT24 model generated using OpenDSS.

Normal System Operating Boundaries

Each electrical device has limits to the voltage it can withstand. This includes end-use equipment and the equipment comprising the power system. Equipment design and construction varies widely, and a single limit does not apply to all devices. Detailed analysis of all equipment to identify voltage limits is impractical. Therefore, industry standards have been established to guide utility engineers in designing a system that is useable for the power consumers. These standards also enable equipment developers to understand the range of conditions to which their equipment may normally be exposed. The standards do not determine whether a piece of equipment will fail [13], so the limits will serve as a baseline for comparison against thresholds commonly used in industry.

For voltages above 1 kV up to 69 kV, IEEE 519-2022 [33] specifies a limit of 3% for individual harmonic voltage and a limit of 5% for voltage total harmonic distortion. IEEE 446-1995 [34] provides generalized design goals for computer manufacturers regarding tolerance to voltage transients. Voltage limits for successful operation of computer equipment are specified by a curve provided in the standard, which is sometimes referred to as the Computer and Business Equipment Manufacturers Association (CBEMA) curve. In summary, the curves suggest that computer equipment experiencing voltages below the minimum limit of 0.87 per unit for more than two seconds may be expected to drop out, while those experiencing voltages above the maximum limit of 1.06 per unit for more than two seconds may be damaged.

IEEE Standard 18-2012 [35] provides standard limits for capacitor bank capability beyond the nominal rating. While normal operation of the capacitor bank is limited to voltages less than or equal to its rated voltage, a capacitor bank can operate under contingency conditions given certain assumptions are met, including the maximum voltage limit of 1.2 per unit. If automatic control is applied on the capacitor, it is expected to be disconnected for voltages well below the defined limit to prevent damage.

Loss of capacitor banks may reduce harmonic amplification within the feeder but may contribute to reactive power deficits during the event.

The power system is designed to provide voltages within five percent of nominal voltage under normal conditions. For short-term emergency conditions, the grid can be operated within ten percent of the nominal voltage. Some systems may have more restrictive limits, for example [36]. Since the normal limits are basic assumptions used during system design, operation outside of these limits may require special attention to ensure protection of equipment and stability of the grid.

Summary and Research Motivation

The motivation for this research is to explore the performance of distribution feeders during asymmetric saturation of the substation transformer. If the feeder performance during such operation is far outside of normal operating boundaries, then the assumptions underlying more large-scale transmission system analysis may be compromised. A comprehensive assessment of the overall power system response to an E3 event cannot be fully realized without an understanding of the distribution response to the saturated transformer cores, even if only to rule out any concern. This research aims to contribute to the efforts of other researchers performing DC current impact studies for the power system, and for those evaluating critical infrastructure systems other than the EPDS by simulating the energization of realistic feeder models using a harmonic voltage source model that represents the harmonic distortion expected during asymmetric transformer saturation.

CHAPTER TWO

Transformer Field Test Measurement Data and Harmonic Powerflow Simulation Comparison

Introduction

The advising professor provided spreadsheets [37] containing terminal measurements of a three-phase power transformer during field experiments where DC current was injected into the transformer neutral [38]–[40]. Field test measurement data of transmission connected transformers during deep asymmetric saturation are essential for the model efforts undertaken here, but it is important to note that the current author did not take part in the tests and that only limited supporting information about the tests was received. For example, the transformer nameplate, test report, and magnetic core information were not available. Some understanding was developed through discussion with the advising professor, who participated in some of the field tests. This data is used to understand and approximate the character of substation transformer response to DC current flow in the windings.

The data provided included three-phase voltages and currents at both terminals of the transformer and the DC current flowing in the transformer neutral. The transformer was connected to an operating transmission grid during the tests. One important detail about this transformer is the grounded-wye winding configuration on the high-side terminal. This ground point is what would enable DC current to flow through the transformer winding and into the earth. The field tests were performed to examine this condition.

The effects of asymmetric transformer core saturation for this transformer are evident in Figure 2.1, which shows three cycles of the measured voltage waveform several seconds after the DC current injection began in one of the tests. The voltages are normalized to the rated crest voltage of the transformer secondary and have been down sampled for practical handling of the large data sets. Due to the similarities observed across the three phases once approximate steady-state conditions were reached, this work will focus on using single-phase representation to approximate the saturated transformer response.

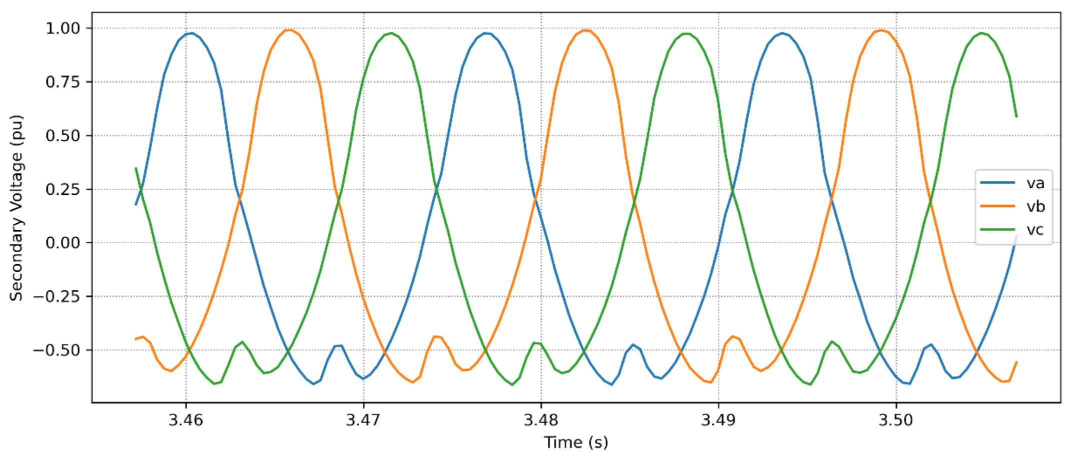

Figure 2.1.-Example secondary voltage of a three-phase transformer during DC current drive asymmetric core saturation.

Analysis of Test Data

The sample rate of the provided data is 100 kHz, which is about 1667 samples per power system frequency cycle. The first twenty harmonics were calculated for each cycle across the entire test using the DFT. The fundamental component of phase-A voltage on the high-side was used as the phase angle reference for the harmonic phasors, by subtracting the product of the phase-A voltage angle and the harmonic number from the angle of each harmonic. The product of the harmonic number is necessary to conserve the waveshape when shifting the reference angle [32]. The magnitude of the fundamental voltage relative to its initial value is shown for one of the tests in Figure 2.2.

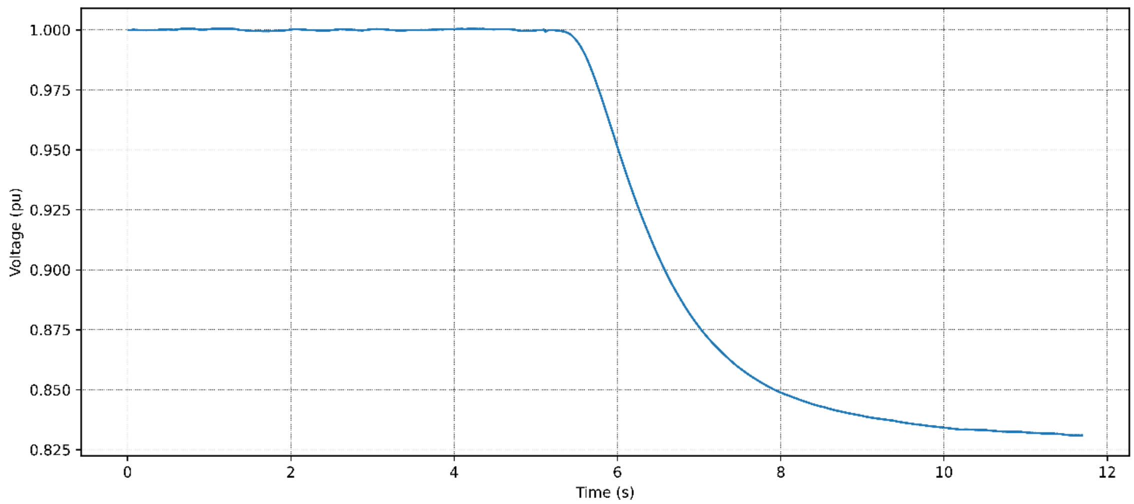

Figure 2.2.-Fundamental component of example secondary voltage of a three-phase transformer during DC current drive asymmetric core saturation.

The magnitude of harmonic voltages 2 through 5 as a percentage of the fundamental component of voltage for the same test is shown in Figure 2.3.

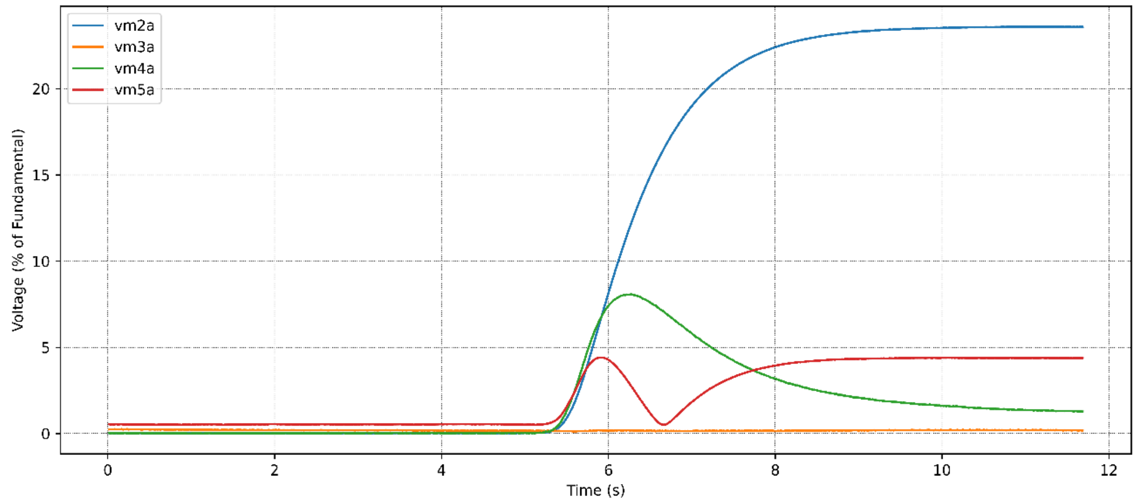

Figure 2.3.-Harmonic components 2 through 5 of example secondary voltage of a three-phase transformer during DC current drive asymmetric core saturation.

The voltage harmonic profile of this test was divided according to Table *2.1*.

Table 2.1.-Time division of test measurements.

Division Label	Start Time (s)	End Time (s)
Pre-Test	0	5
Initial Saturation	5	8
Final Saturation	8	~12

Figure 2.4 through Figure 2.6 show statistical summaries of the harmonic spectrum for each period in the three divisions for the same test.

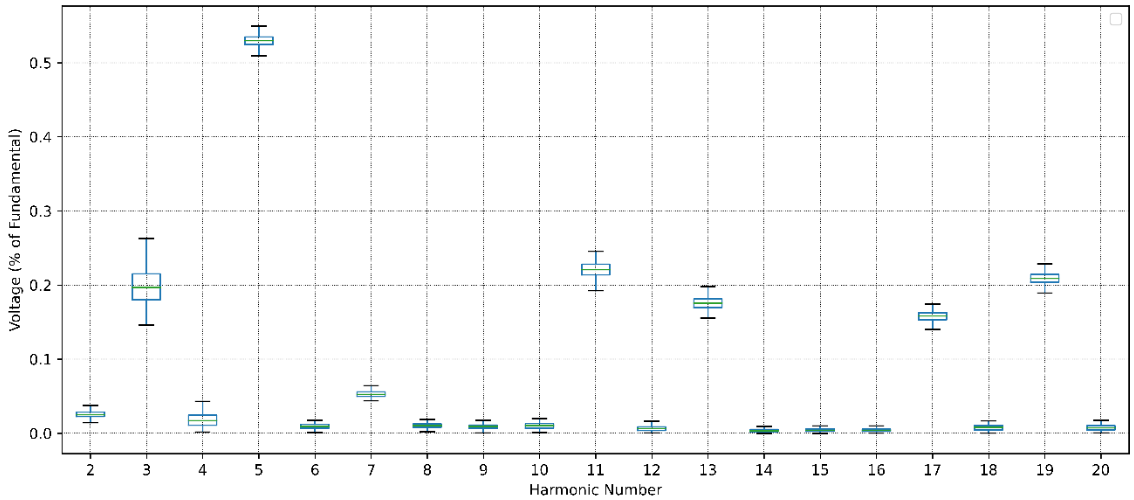

Figure 2.4.-Boxplot of the pre-test division (0 seconds to 5 seconds).

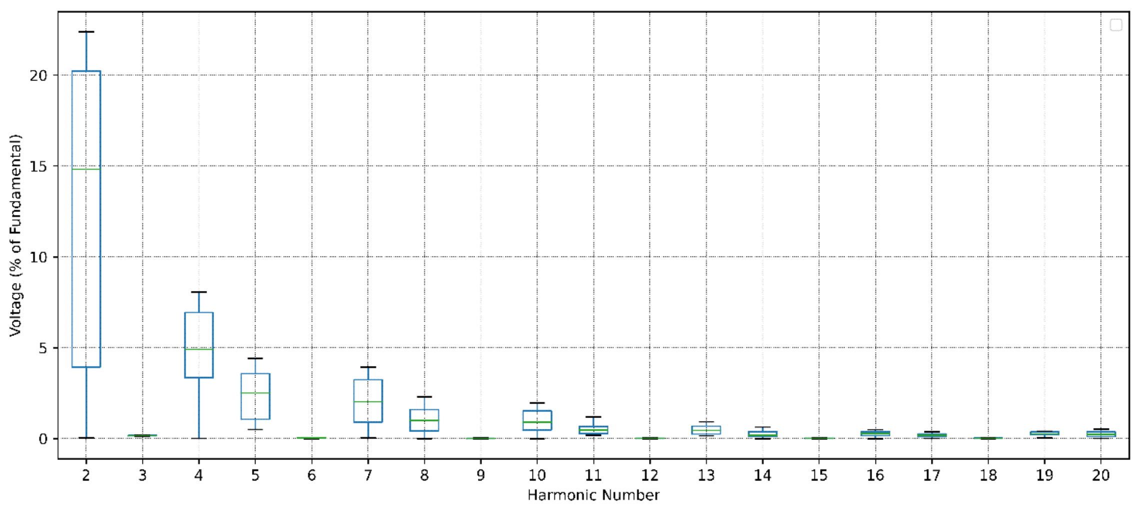

Figure 2.5.-Boxplot of the initial saturation division (5 seconds to 8 seconds)..

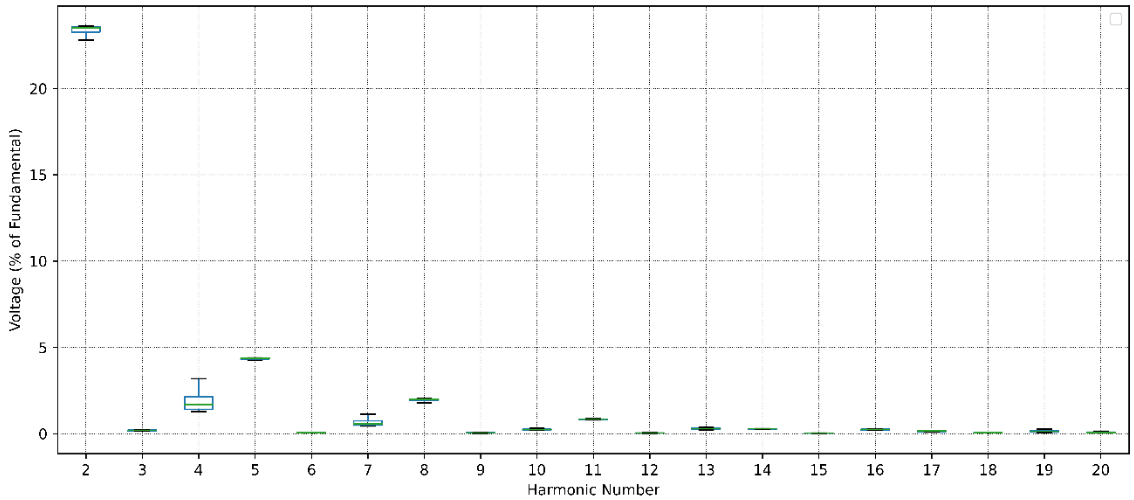

Figure 2.6.-Boxplot of the final saturation division (8 seconds to 12 seconds)..

Less than one percent harmonics are present in the signal during the Pre-Test division. During the Initial Saturation division, the harmonics experience the widest range of values and some experience their peak values. The harmonics have settled to steady values during the Final Saturation division, where the second harmonic holds very near to its peak value while the core remains saturated.

The field tests included separate tests to consider the impacts of resistive and inductive loading. Figure 2.7 through Figure 2.10 show statistical summaries of the harmonic voltages and currents during the Final Saturation division for resistive and inductive load conditions for a similar magnitude of DC current injection.

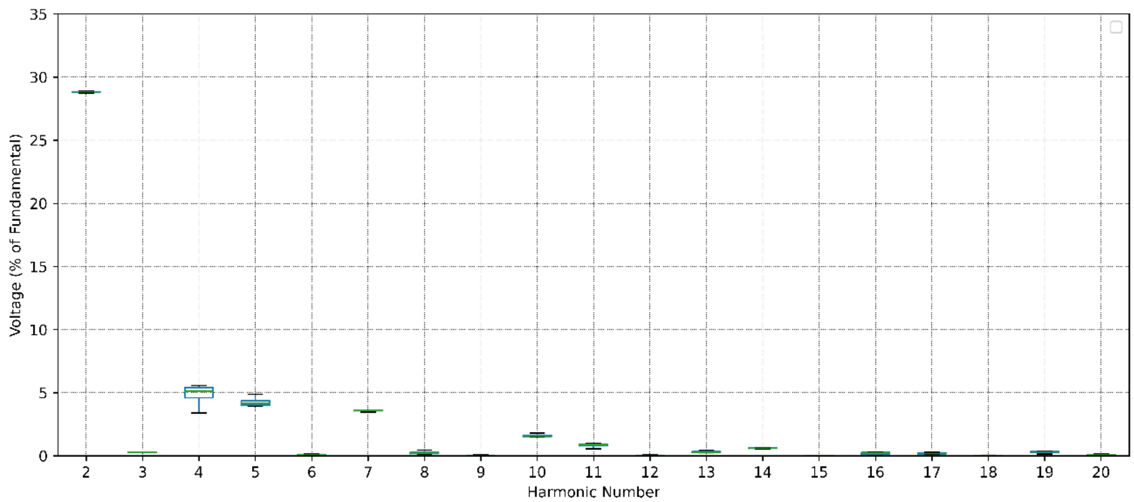

Figure 2.7.-Boxplot of resistive test voltage harmonics during the final saturation division.

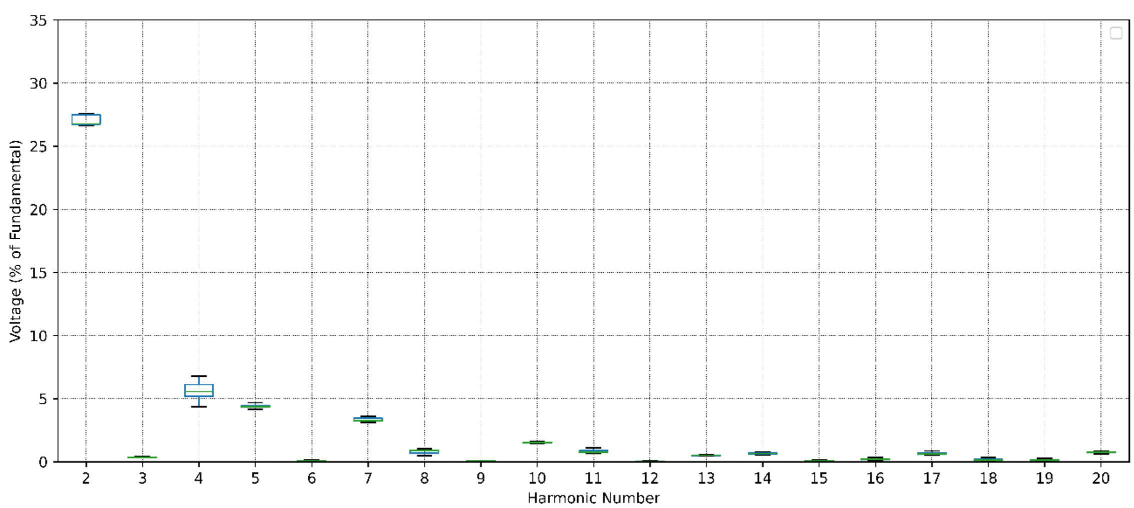

Figure 2.8.-Boxplot of inductive test voltage harmonics during the final saturation division.

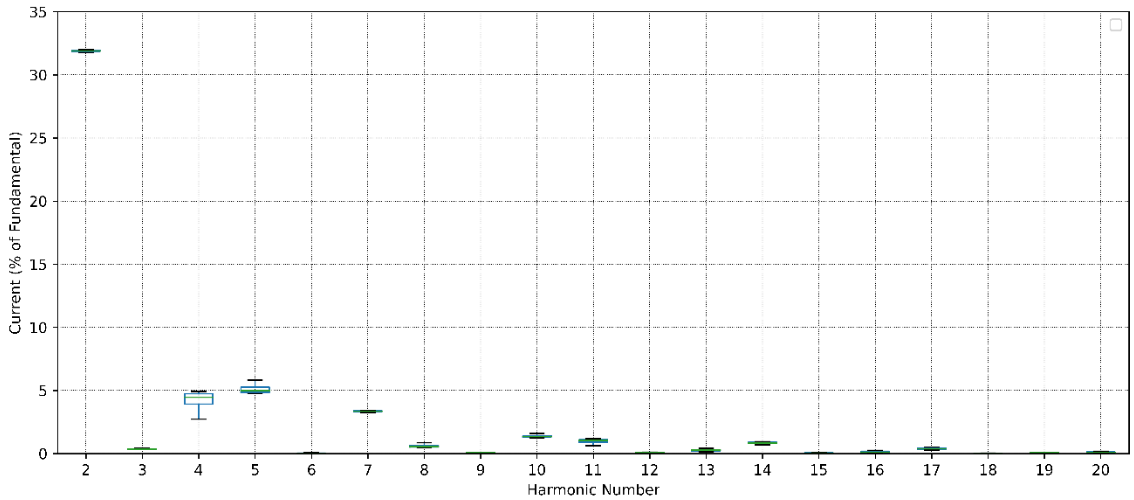

Figure 2.9.-Boxplot of resistive test current harmonics during the final saturation division.

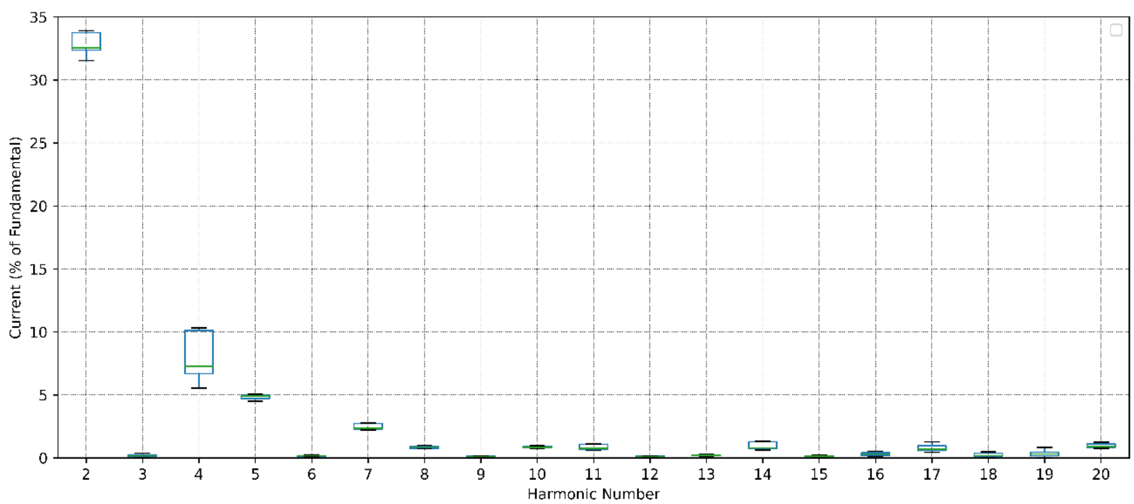

Figure 2.10.-Boxplot of inductive test current harmonics during the final saturation division.

Comparing the measurements between the two loading conditions revealed that the voltage harmonics have less variation between the loading conditions than the current harmonics. In addition, the plots shown in Figure 2.11 and Figure 2.12 show that the fundamental and second harmonic voltages experience little impact to large changes in the fundamental and second harmonic current during the tests.

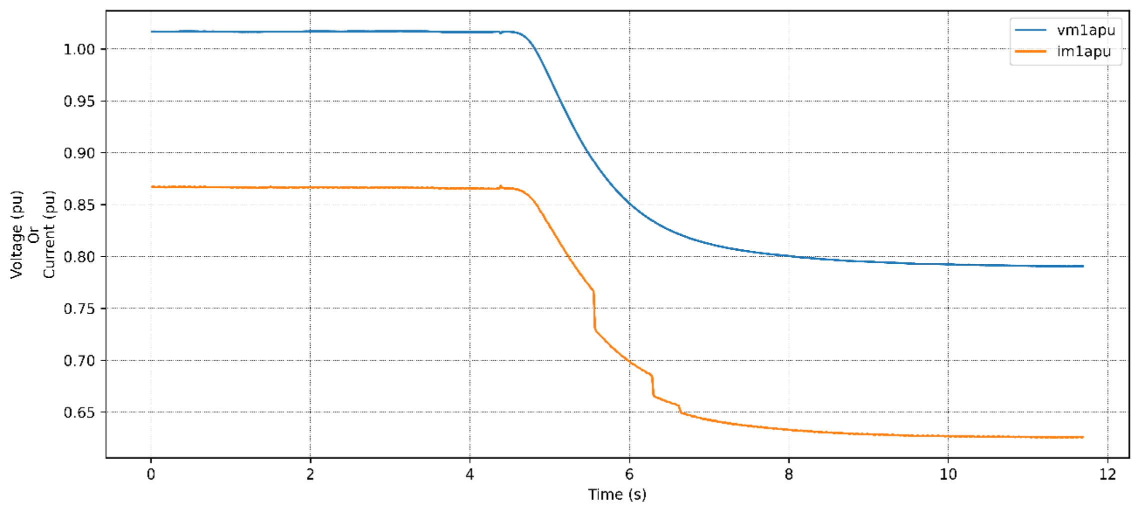

Figure 2.11.-Fundamental component of voltage and current for one test.

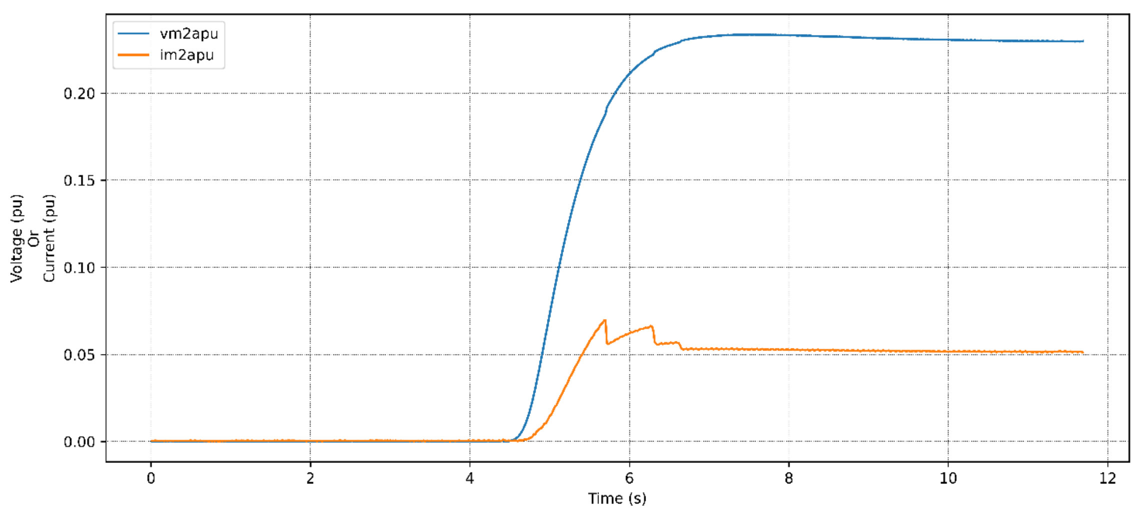

Figure 2.12.-Second harmonic of voltage and current for one test.

Figure 2.13 shows the fundamental component of per unit secondary voltage for multiple tests with similar DC current injection but different loading. This plot shows the entire range of samples in the tests, including the release of DC current.

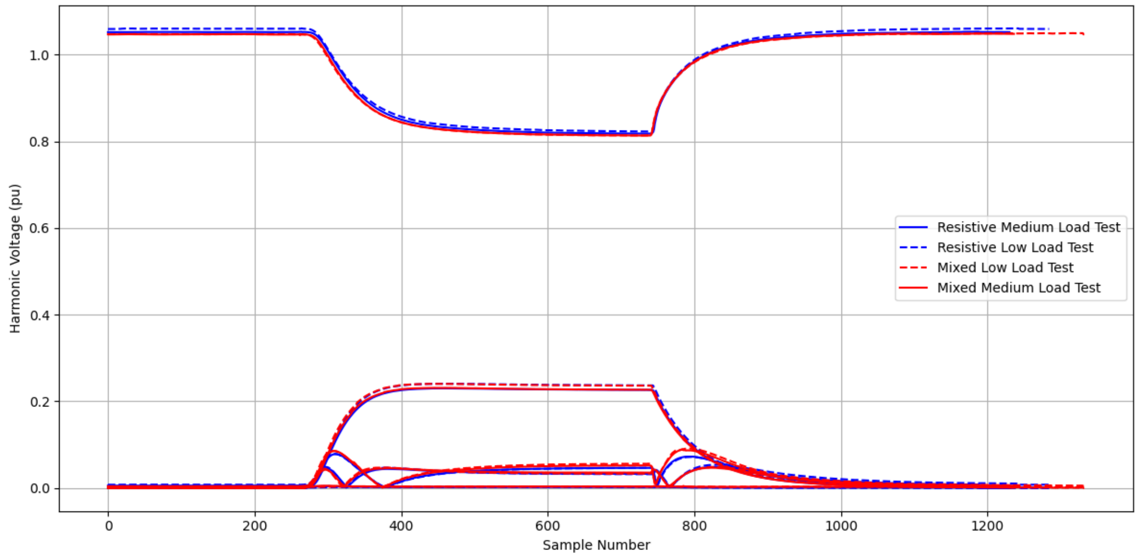

Figure 2.13.-Fundamental component of voltage measurement for four tests.

Upon injection of DC current, each voltage harmonic traverses a nonlinear curve before settling at a steady-state value. The delay is determined by the circuit of the transformer, power system, and the earth connection [41]. Some load tripped during some of the tests. The effect is visible in Figure 2.14 which shows steep changes in the fundamental component of per unit secondary current. The load trip caused a large response in current but only a minor response in voltage.

Since the voltage harmonics remained consistent regardless of the transformer secondary load content, this work will approach modeling of the saturated substation transformer as a harmonic voltage source (HVS), which is used when the source of harmonics behaves as a voltage source [42].

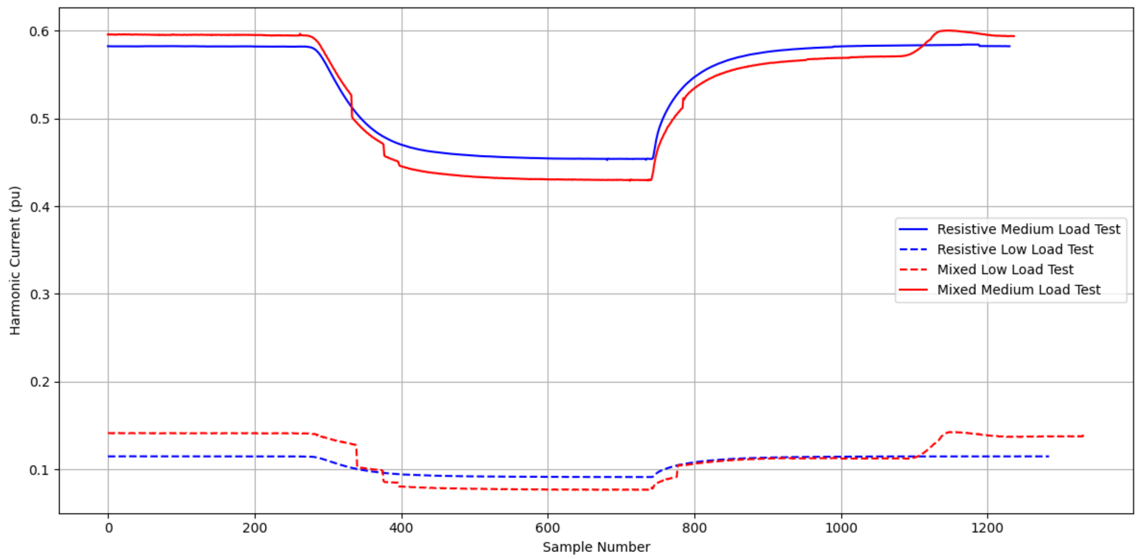

Figure 2.14.-Fundamental component of current measurement for four tests.

Harmonic Powerflow Simulation and Comparison

The harmonic voltage spectrum was modeled in OpenDSS using a spectrum file that includes the harmonic magnitudes as a percentage of fundamental and the phase angles in degrees. The voltage source model is not treated as a Thevenin equivalent since the equivalent source impedance for the field test configuration is unknown. Instead, the source is modeled with a very small impedance such that the source is approximately infinite. One weakness of this approach is that the harmonic powerflow solution at resonant conditions can be overly pessimistic [43]. However, the harmonic voltage spectrum obtained from the measurements already includes the effects of a finite source, and this is included directly in the harmonic voltage source model as the per unit voltage of the fundamental component of voltage at the source.

A feeder model is needed to simulate the test conditions. The field tests were performed under various loading conditions. Since each test included measurements before the DC current injection began, these measurements supply information about the pre-test steady-state loading of the transformer. The feeder model developed consists of a load model connected to the substation bus through a zero-impedance branch which is used to monitor the voltage of the source and the current supplied to the load. The load active and reactive power is determined using the initial measurement of a test by taking the fundamental RMS voltage and current phasors of each phase and computing the complex power. Load is typically modeled as constant power in powerflow simulations, and as a constant impedance in harmonic powerflow simulations. The power of a constant power load is approximately independent of its terminal voltage, while the power of a constant impedance load is dependent on its terminal voltage. The fundamental frequency component of load observed in the field test data was better represented with a constant impedance load model, so this change was made in the model.

OpenDSS software was used to simulate harmonic powerflow of the feeder model. Figure 2.15 shows a oneline diagram of the simple system model used to compare the performance of the harmonic voltage source model against the test measurements.

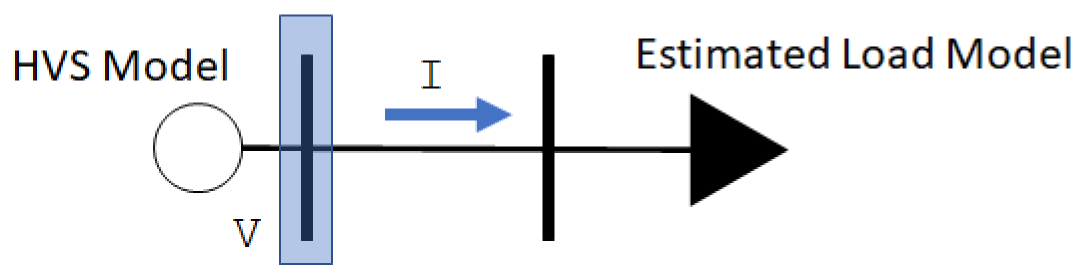

Figure 2.15.-Oneline diagram of simple system model for harmonic powerflow simulation of the field tests.

This system combines the harmonic voltage source model and estimated load models described earlier, connected by a zero-impedance line. The voltage at the bus highlighted in blue and labeled with "V" is used to measure the simulated voltage from the harmonic voltage source. The zero-impedance line provides a dedicated way of measuring the current supplied by the HVS during each simulation. This is necessary because the OpenDSS harmonic load model has an optional current source component, and monitoring the load directly appears to monitor this current source component. Simulations were performed across the range of harmonic spectrums obtained from the field test data.

The goal of these simulations is to monitor the harmonic current spectrum flowing from the source for a given voltage spectrum to determine whether the harmonic voltage source produces reasonable harmonic currents as compared to the field test measurements. Comparison of the simulated and measured current spectrum gives an assessment of the reasonableness of the harmonic modeling and simulation process.

Figure 2.16 shows the test measurement harmonic voltages with an "o" marker and the simulated harmonic voltages with an "x" marker. Each marker represents a single cycle of the field test and the corresponding steady-state harmonic powerflow simulation result. While the figure shows a single curve, it is comprised of several separate harmonic simulations and time-domain simulation was not performed. The field test and simulation results are almost identical. This is expected because the voltage source model is specified with the measurement voltage harmonics directly. The point of this figure is to check that the voltage source model is parameterized correctly and performing as expected.

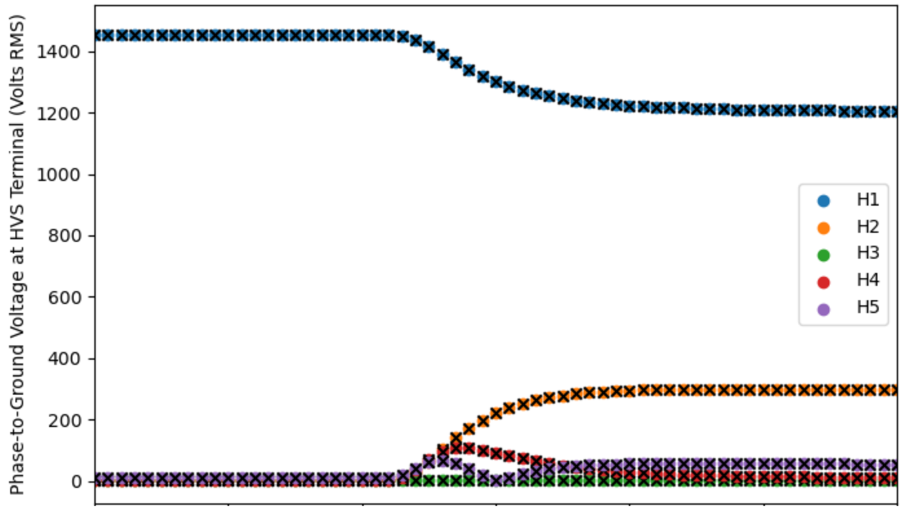

Figure 2.16.-Comparison of voltage between field test and harmonic simulation.

Figure 2.17 shows the test measurement harmonic currents with an "o" marker and the simulated harmonic currents with an "x" marker. They closely match, although the model slightly underestimates the second harmonic current for this test. The response shape characteristics match is reasonable.

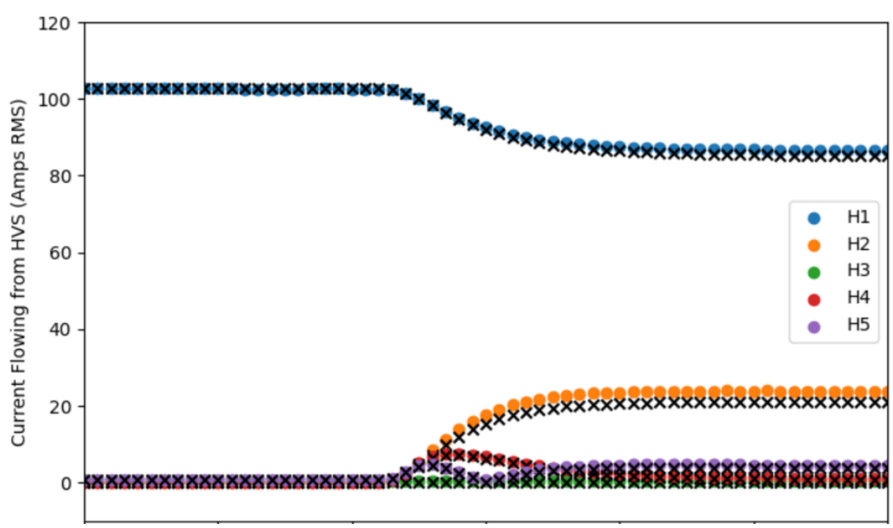

Figure 2.17.-Comparison of current between field test and harmonic simulation.

Load model parameters can be varied to get a very close match across the test duration, as shown in Figure 2.18. While this modification is possible, it is not necessary for carrying out the objective of this work, which is to estimate a reasonable range of feeder responses. Therefore, the unmodified harmonic load model will be used for subsequent harmonic simulations in this work and sensitivity analysis will be used to understand the impacts of load model assumptions.

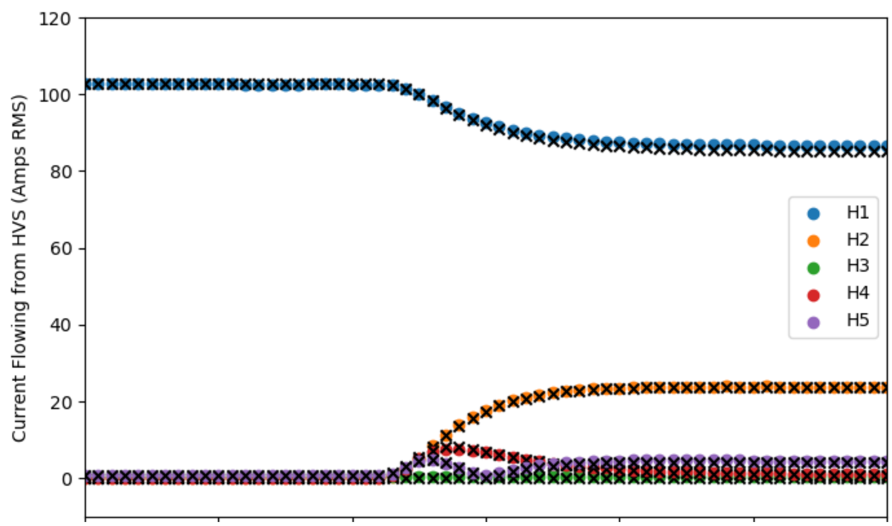

Figure 2.18.-Comparison of current between field test and harmonic simulation with adjusted harmonic load model options.

Summary

Test measurement data provided for this work were analyzed to characterize the response of substation transformers to the flow of DC current in the windings. The secondary voltage and current waveform distortion increased with increasing magnitudes of DC current. Decomposition of the time domain waveforms into harmonic spectra using the DFT revealed distinct nonlinear harmonic patterns.

The secondary voltage and current harmonics obtained from the measurement data were used to evaluate the ability of harmonic powerflow simulation to represent the energization of loads by the saturated transformer using a harmonic voltage source located at the substation. The harmonic powerflow simulations produced a reasonable estimate of the harmonic response of the feeder as compared to the field test measurements.

One limitation of the data used here is that the measurements provided cannot represent the complete variety of power transformers in operation today. Significant second harmonic content during asymmetric transformer core saturation is reported across the literature regardless of transformer type, but the higher order harmonic content is less consistent. Transformer core and winding configuration influence the transformer response to asymmetric core saturation, so the studies performed in this research may only be representative of a subset of the possible outcomes in an actual grid. For example, harmonic content reported in [7] shows significant 3rd and 6th harmonics for various transformers during asymmetric core saturation, which are not present in the test measurement data used in this work. In addition, substation transformers with a delta winding configuration on the high-side do not offer a path for DC current to flow between the earth and the power transmission system, so are not subject to asymmetric saturation in response to DC current flowing on the high-side.

CHAPTER THREE

Approximate Steady-State Model of Secondary Terminal Voltage for Asymmetrically Saturated Substation Transformer

Introduction

This chapter will develop a method to approximate the secondary terminal response of a substation transformer to the flow of DC current in the primary winding, with the aim of generalizing the response observed in the test measurement data summarized in Chapter 2. First a current source model will be developed to represent the magnetizing branch current following the method outlined in [25] and [26], but with a modified relationship between flux-linkage and current as reported in [5]. Then the current source model will be used as the magnetizing branch of the t-model [15], where the resulting differential equation will be solved numerically using the RK4 algorithm. The approximate solution for the magnetizing current and the t-model circuit will be repeated, while carrying portions of the solution from one step forward as the initial condition for the next step until the change in estimated states from one step to the next is small. This solution process is like those used in the electronics field to determine the steady-state behavior of nonlinear electronic circuits, for example in [18], [19], and [20].

Approximate Magnetizing Current Source Model

Solution of the transformer t-model with a linear core was summarized in the Literature Review section. For the linear case, the relationship between flux-linkage and magnetizing current is illustrated in Figure 3.1.

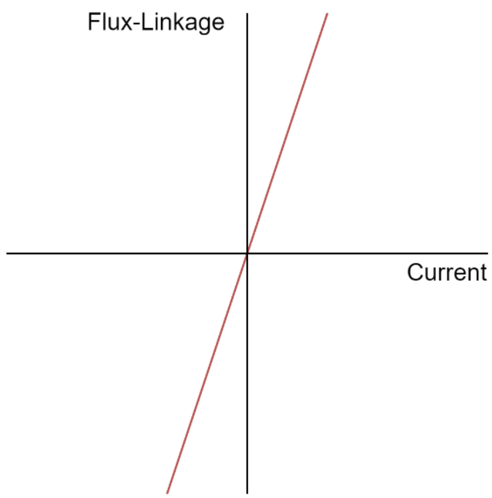

Figure 3.1.-Relationship between flux-linkage and current for a single-slope transformer core model.

Assuming sinusoidal flux-linkage the resulting magnetizing current will be sinusoidal, with a DC offset that is proportional to the flux-linkage offset. When operating in this linear region, the core behaves as a linear inductor, where the core inductance is equal to the slope of the flux-linkage current curve.

The magnetizing current can be determined by calculating the magnetizing current for each value of flux-linkage using the following equation. The result is shown visually in the diagrams that follow.

$$\mathrm{Im}(t) = \frac{1}{L} \cdot \lambda_m(t) \tag{3.1}$$

A linear transformer energized by an ideal sinusoidal voltage source produces linear magnetizing current. An example is shown in Figure 3.2 and Figure 3.3, where the waveshape of the magnetizing current remains sinusoidal regardless of the offset in flux-linkage and magnetizing current.

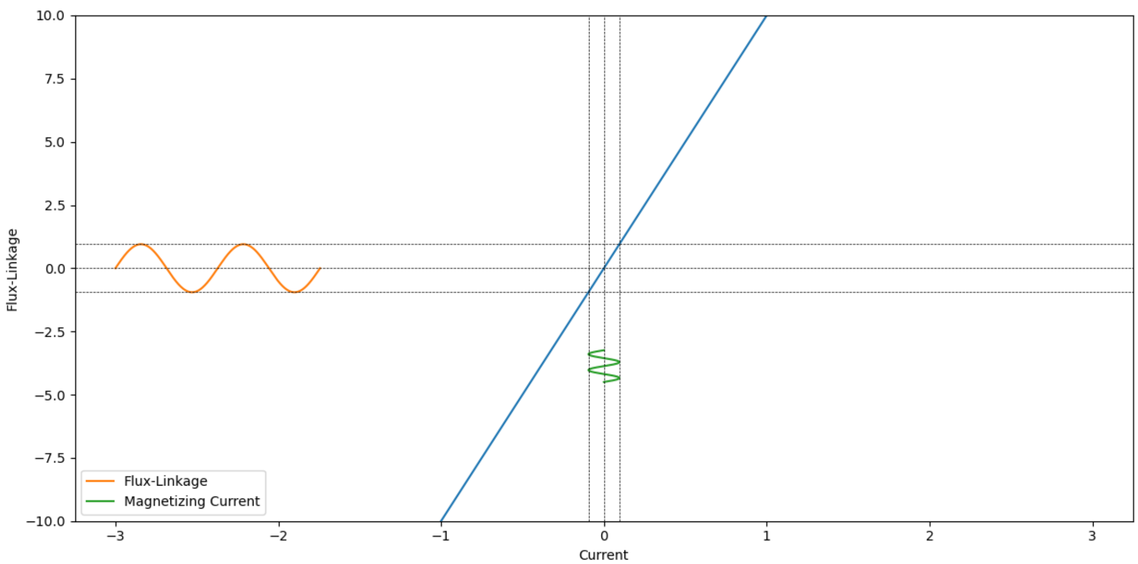

Figure 3.2.-Flux-linkage current relationship for single-slope core without offset.

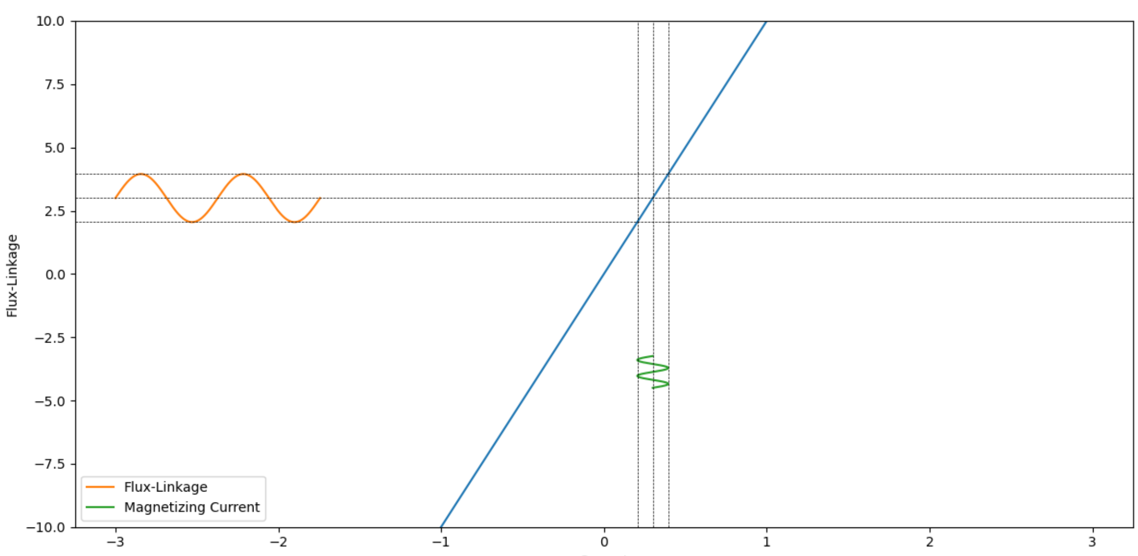

Figure 3.3.-Flux-linkage current relationship for single-slope core with offset.

Since an iron core transformer can saturate, a modification to the straight-line core model is necessary. Even after the core material is saturated, the inductance does not collapse to zero. Instead, it approaches what is referred to as the air-core inductance [5]. Using two slopes to represent the flux current relationship for a saturable magnetic core gives a relationship as shown in Figure 3.4. The intersection point of the two slopes is referred to as the knee of the curve.

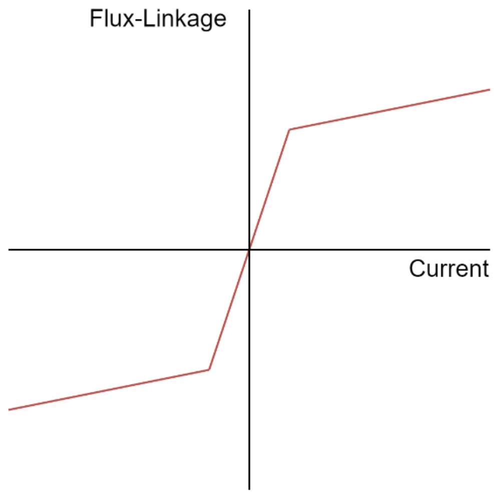

Figure 3.4.-Relationship between flux-linkage and current for a dual-slope transformer core model.

Figure 3.5 delineates the air core region from the iron core region with respect to the flux-linkage axis. The flux-linkage will produce magnetizing current proportional to the slope of the curve in each region.

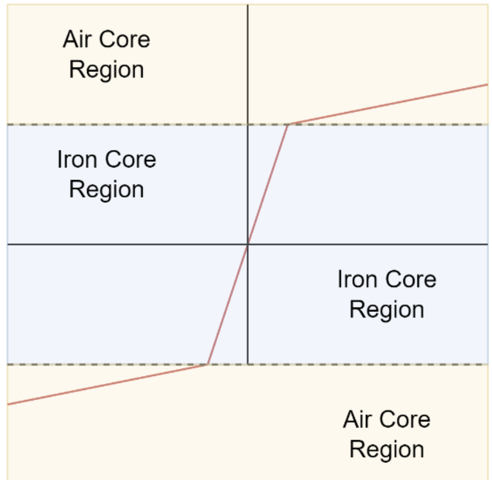

Figure 3.5.-Relationship between flux-linkage and current for a dual-slope transformer core model with region labels.

This model is nonlinear, and it is therefore possible for the flux-linkage to cross the boundary between the two slopes. The magnetizing current will become distorted when the flux-linkage wave overlaps the knee of the curve because of the change in slope, or inductance, between the two regions.

When the flux-linkage wave is entirely within the iron core region, the magnetizing current is relatively small and sinusoidal, as shown in Figure 3.6. Under this condition, the relationship between flux-linkage and magnetizing current is linear, as in the single slope core example.

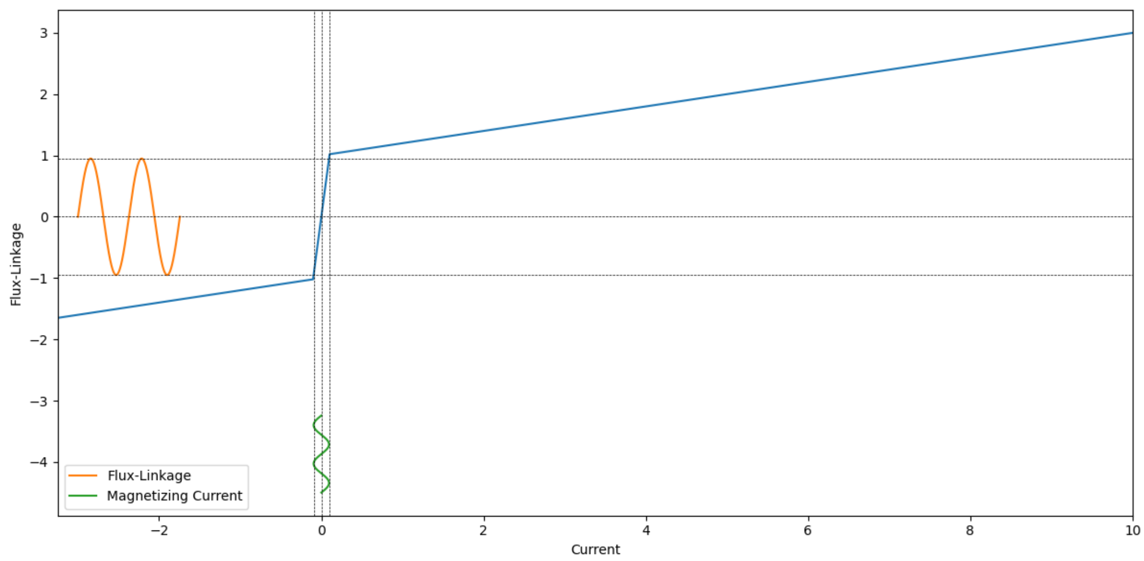

Figure 3.6.-Flux-linkage current relationship for dual-slope core without offset.

Introducing a small offset in the flux-linkage, the magnetizing current becomes distorted by spikes corresponding to the portion of flux-linkage that exceeds the knee point of the curve. This is illustrated in Figure 3.7. The magnetizing current is distorted even while the flux-linkage remains purely sinusoidal.

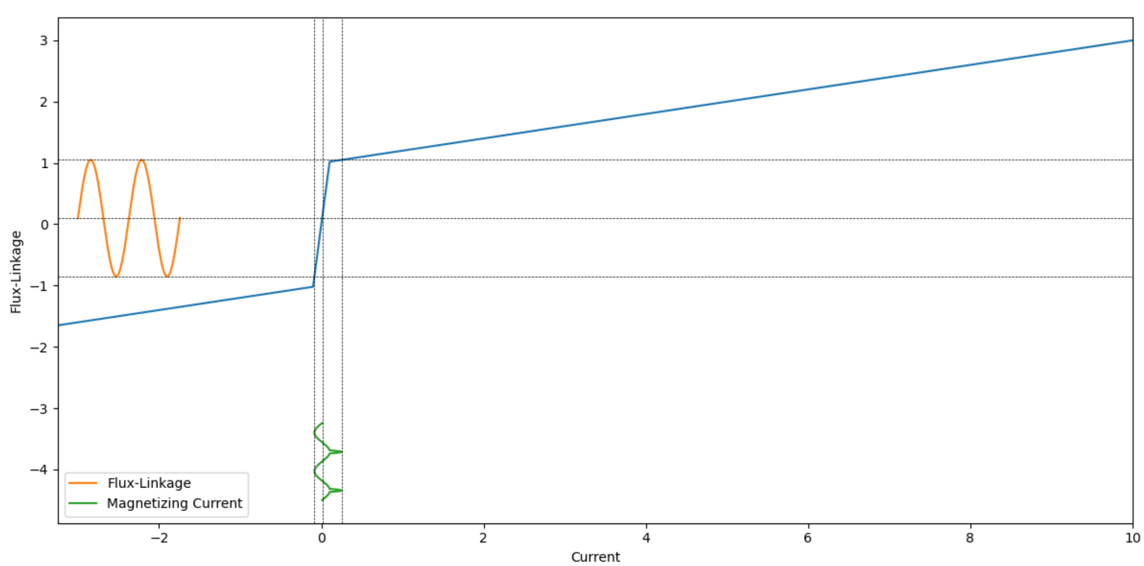

Figure 3.7.-Flux-linkage current relationship for dual-slope core with a small offset.

The magnetizing current spikes become larger for increasing offset in flux-linkage, as illustrated in Figure 3.8. The magnitude of the spikes is significant compared to normal operation where there is no offset in flux-linkage.

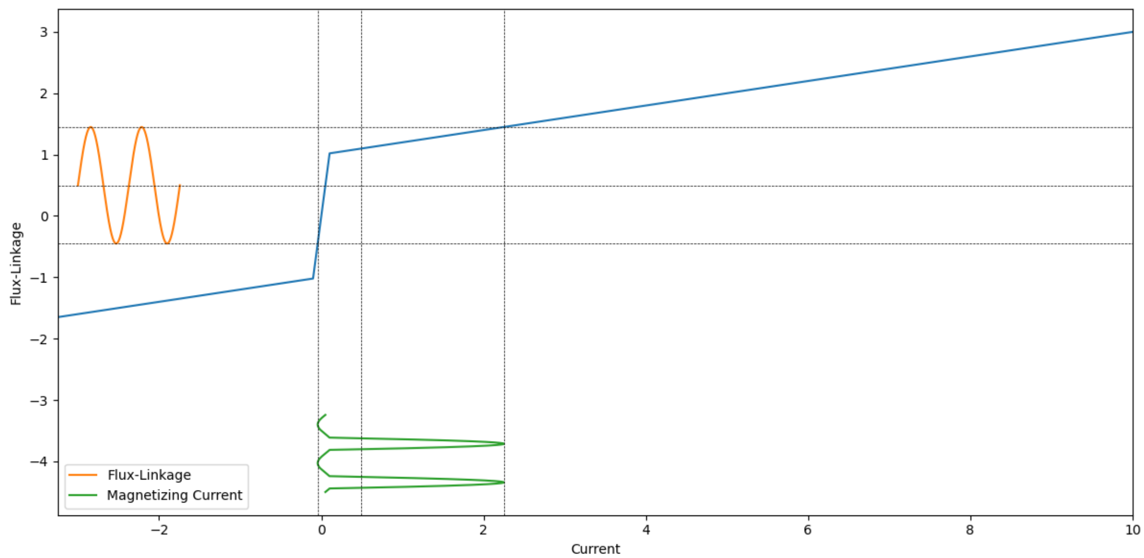

Figure 3.8.-Flux-linkage current relationship for dual-slope core with a large offset.

Finally, the magnetizing current becomes sinusoidal again when the flux-linkage is so far offset that it is entirely within the air core region of the curve, as shown in Figure 3.9. Although the magnetizing current is no longer distorted, the magnitude is extremely high as compared to nominal operation. A practical transformer may be damaged before this condition is met, but these potential limitations are not considered in this work.

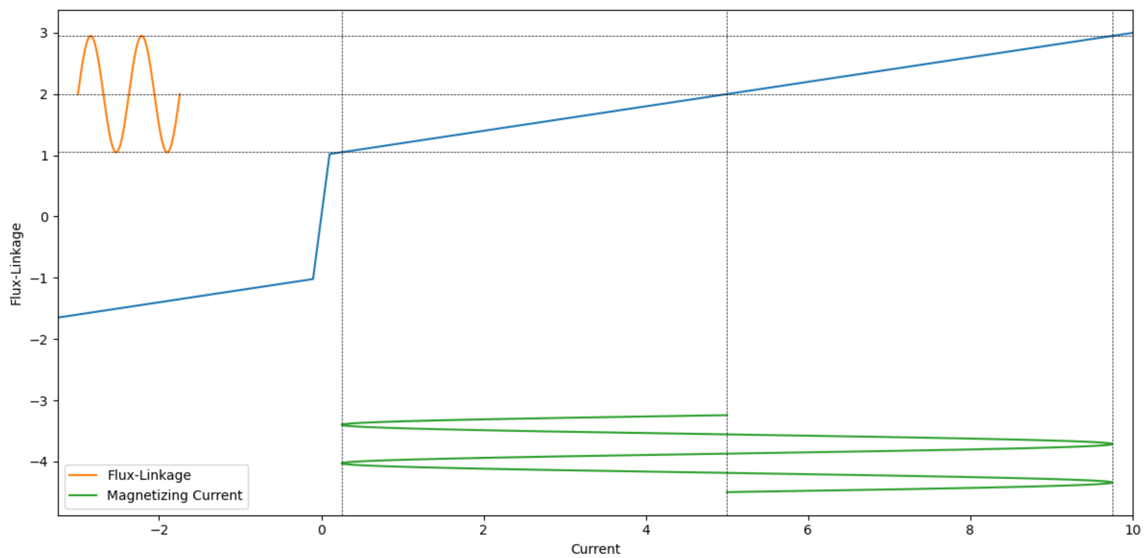

Figure 3.9.-Flux-linkage current relationship for dual-slope core while operating entirely within the air core region.

The magnetizing current waveshapes for the different flux-linkage offsets considered in this example are shown more clearly in Figure 3.10.

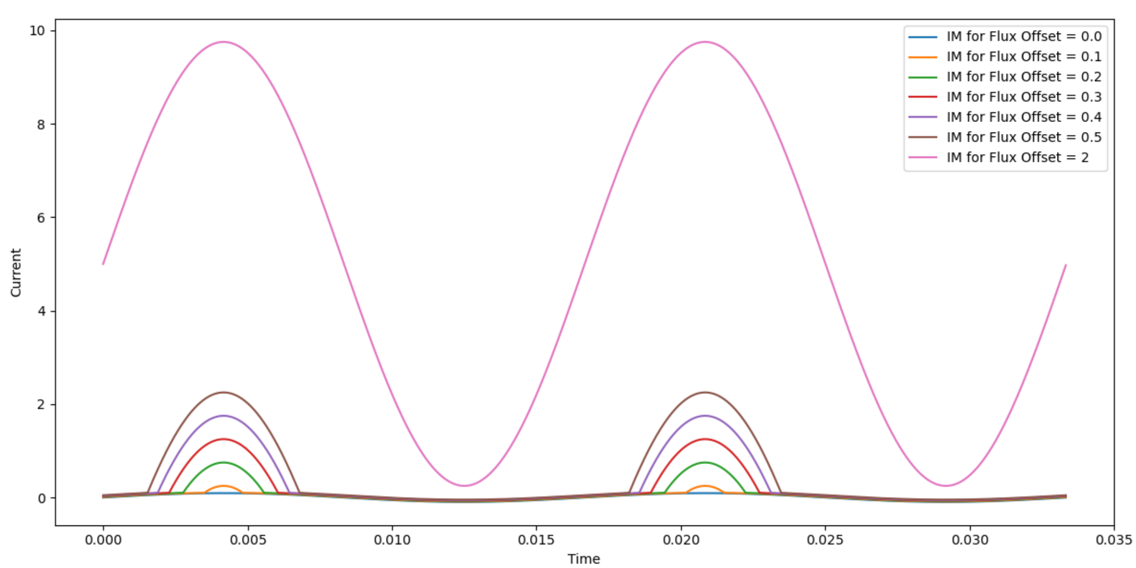

Figure 3.10.-Magentizing current waveshapes for increasing flux-linkage offset.

The average values of flux-linkage and magnetizing current intersect on the flux-linkage current curve when the waves are entirely within one of the linear regions. Otherwise, their means do not intersect at a point on the curve. The mean values of flux-linkage and magnetizing current are not linearly related when either wave overlaps the knee of the curve, so knowledge of the offset value in the magnetizing current does not enable direct solution of the flux-linkage offset. Analytic solution of nonlinear problems like asymmetric core saturation are difficult. However, to estimate the level of distortion that results from a specific amount of DC current flowing in the transformer winding, the corresponding flux-linkage offset must be found. The solution to this problem is approximated numerically by adjusting the flux offset iteratively and recomputing the magnetizing current until the average value of the magnetizing current is approximately equal to the DC current in the winding [26]. For simplicity the flux linkage is assumed to remain undistorted in this work. Improving this is left for potential future work.

Applying the DFT to each distorted magnetizing current wave calculated using the dual slope core model produces the harmonic spectrum shown in Figure 3.11 with respect to the flux-linkage offset value. This qualitatively resembles the shape of harmonic response observed in the field test data.

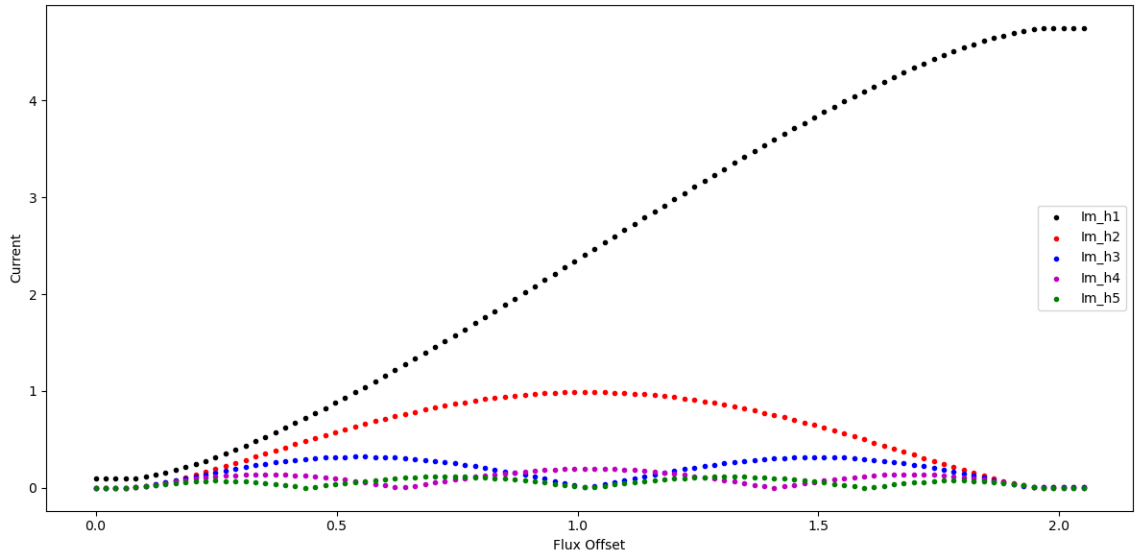

Figure 3.11.-Harmonic spectrum of magnetizing current for dual-slope core model with respect to increasing flux-linkage offset.

Various aspects of the output calculations developed here, as shown in Figure 3.12 through Figure 3.17, were compared to those published in [26] and found to be in close agreement.

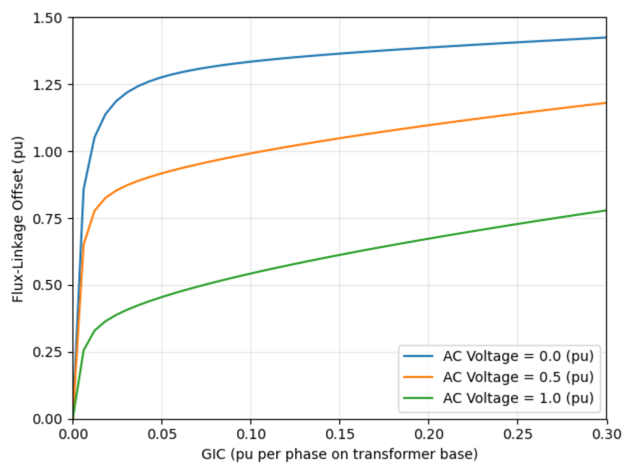

Figure 3.12.-Flux-linkage offset with respect to DC current for different AC voltage magnitudes for comparison with [26].

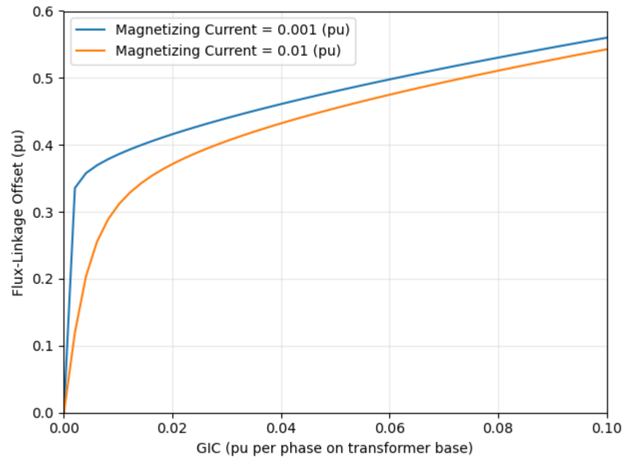

Figure 3.13.-Flux-linkage offset with respect to DC current for different nominal magnetizing current magnitudes for comparison with [26].

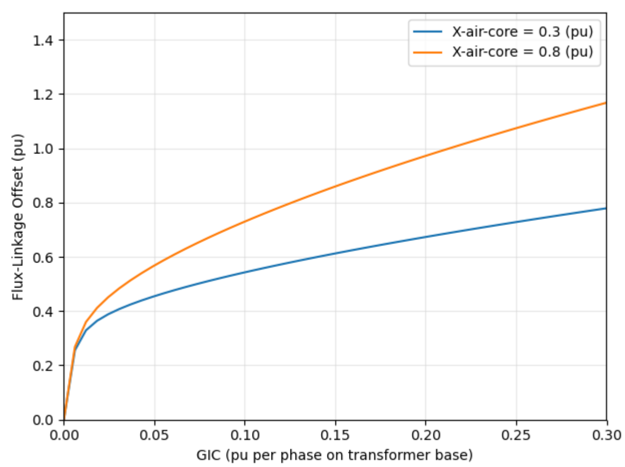

Figure 3.14.-Flux-linkage offset with respect to DC current for different air core reactance magnitudes for comparison with [26].

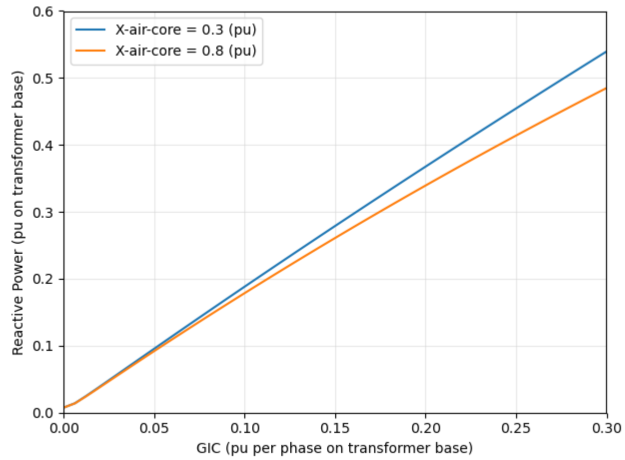

Figure 3.15.-Reactive power with respect to DC current for different air core reactance magnitudes for comparison with [26].

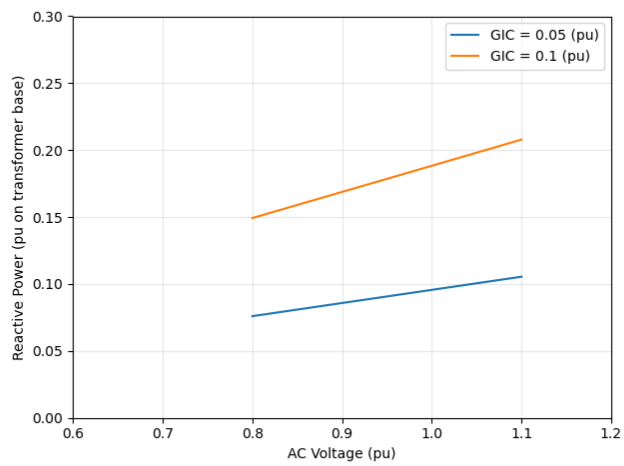

Figure 3.16.-Reactive power with respect to AC voltage for different DC current magnitudes for comparison with [26].

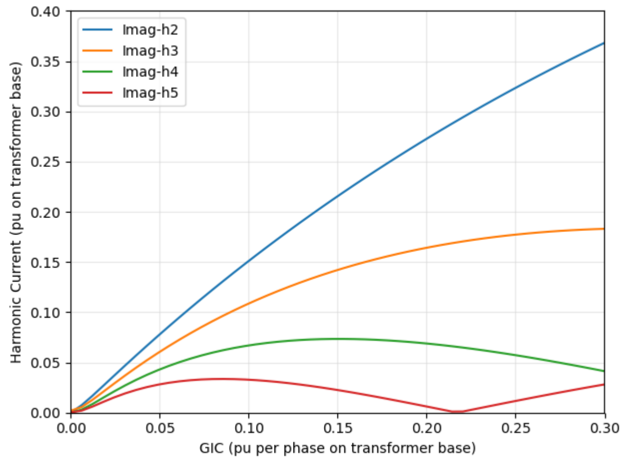

Figure 3.17.-Magnetizing current harmonics with respect to DC current for comparison with [26].

The sharp bend at the knee point in the two-slope core model may present numerical challenges when solving the t-model circuit later, so the dual slope core model was replaced with the magnetizing current function presented in [5]. This function reduces sharp edges and allows the flux-linkage current curve to be parameterized using a conventional form. The effect is illustrated generically in Figure 3.18, where the sharp bend at the knee is replaced by a smooth curve. Sharp changes in the magnetizing current near the knee become smooth curves with this function.

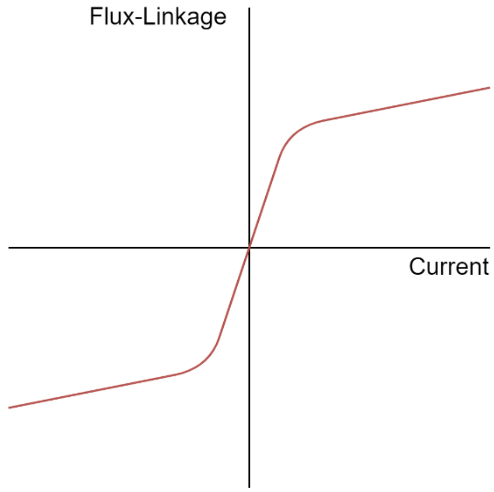

Figure 3.18.-Generic flux-linkage and current for a transformer core model with a curved knee.

Although retaining a small magnitude during nominal operation with the improved core model, the nominal magnetizing current changes from a sinusoidal waveform to one that is distorted, as shown in Figure 3.19. This is because the bend of the knee extends into the normal operating range, which is consistent with actual substation transformers in practice.

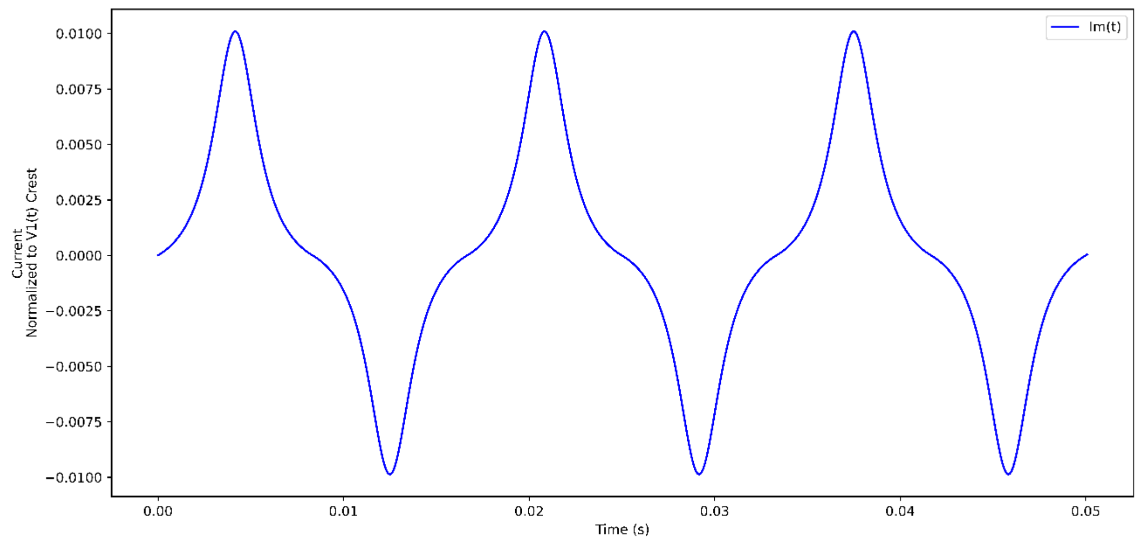

Figure 3.19.-Nominal magnetizing current waveshape for the updated core model.

The algorithm used to the compute the magnetizing current is summarized in Figure 3.20. After computation, the calculated data is used as a current source model for the magnetizing branch of the transformer t-model, explained in the next section.

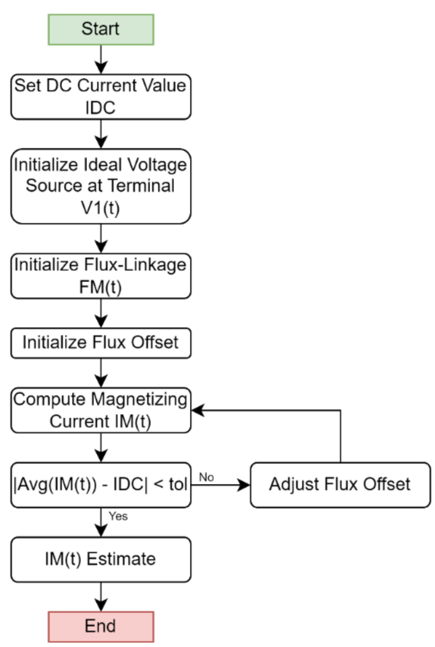

Figure 3.20.-Block diagram of the algorithm used to approximate the magnetizing current by implementing the method presented in [26].

Approximate Secondary Terminal Voltage Source Model

A t-model circuit with a current source magnetizing branch is shown in Figure 3.21. The current source is parameterized with the distorted magnetizing current values computed earlier. Notice that the secondary values are not primed in the diagram, but they still refer to secondary values referred to the primary. This is done to avoid confusion with time derivatives.

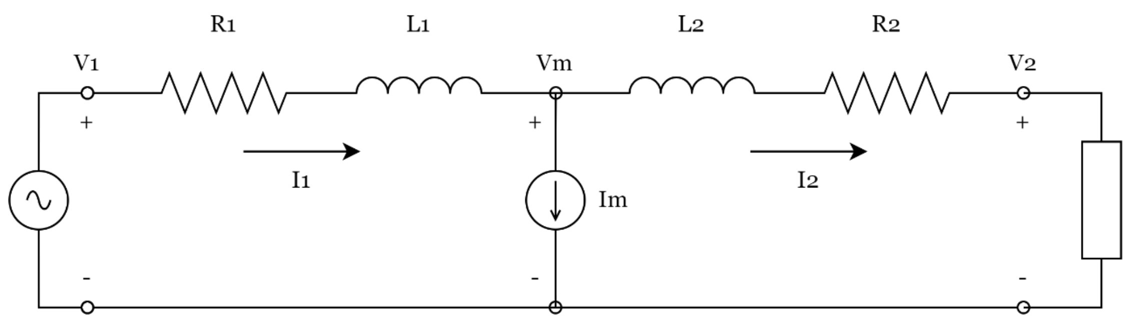

Figure 3.21.-Circuit diagram of the t-model with a current source magnetizing branch.

The differential equation for this circuit is the following, where the primes signify a derivative with respect to time.

$$I2'(t) = \frac{1}{(L1+L2)} \cdot [V1(t) - R1 \cdot [Im(t) + I2(t)] - L1 \cdot Im'(t) - R2 \cdot I2(t)] \quad (3.2)$$

The equation is simplified by assuming a series RL load and lumping the load resistance with R2 and the load inductance with L2. The solution with 50% of rated load and zero DC current is estimated using the RK4 algorithm and plots for three cycles of V1(t), V2(t), and I2(t) are shown in Figure 3.22, and the solution with rated load on the secondary and zero DC current produces the terminal quantities shown in Figure 3.23.

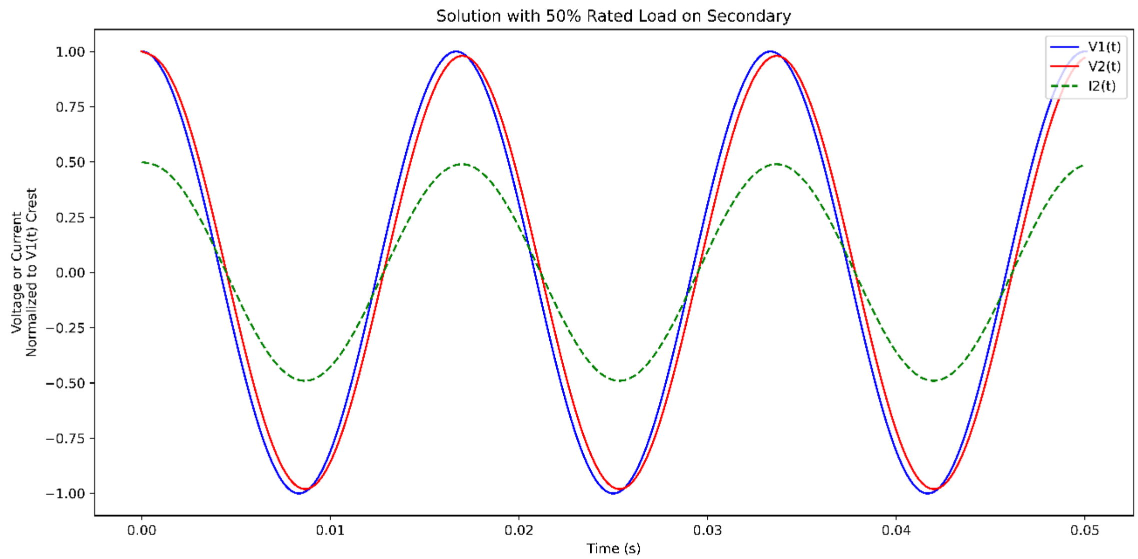

Figure 3.22.-Solution of t-model circuit with 50% of rated load and zero DC current.

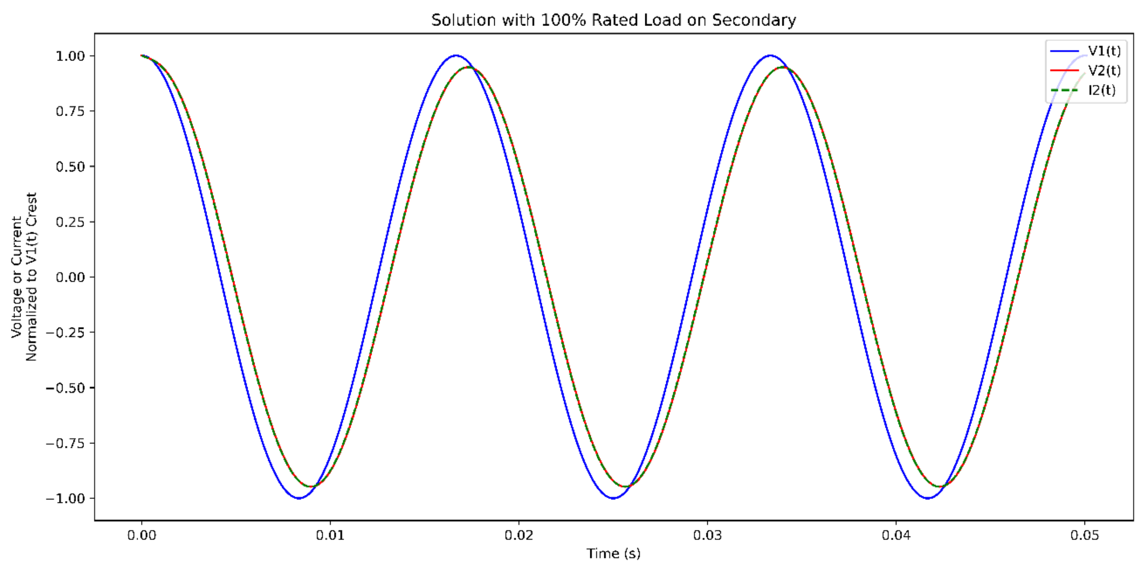

Figure 3.23.-Solution of t-model circuit with 100% of rated load and zero DC current.

The solution method used here is similar to hybrid circuit solution techniques used to estimate steady-state behavior of nonlinear electronic circuits, for example as in [20]. These methods combine time-domain and frequency-domain techniques, in attempt to rapidly converge to a steady-state periodic solution where pure time-domain simulation is too computationally burdensome [18]. In the method presented here, harmonic zero, the DC component of the signal, is used to iteratively estimate the distorted magnetizing current. The magnetizing current estimate is combined with the t-model that is energized by an ideal voltage source on the primary terminal so that an estimate for the time-domain secondary current can be obtained through numerical solution of the resulting differential equation. The estimation is computed repeatedly until the quantity Vm(t) ceases to change appreciably between iterations. The solution algorithm is summarized in Figure 3.26.

In the calculations performed in this work, the flux-linkage waveshape is not updated after the original initialization. Updates to the method to account for flux-linkage distortion is left as future work. To accommodate this development, the solution algorithm is arranged to allow for this update without significant change in form. Should this method be extended to update the flux-linkage with distortion, the change can be applied after the Vm(t) estimate is calculated and contribute an update to the initial conditions on the following iteration.

After V2(t) is estimated, the single-phase result is converted to three-phase by accounting for the relation between the primary and secondary voltages in a wye-delta transformer [44], which results in a phase shift, the elimination of triplen harmonics, and a change in the waveshape. Three cycles of secondary voltage computed for DC current between 0 and 2 per unit is shown in Figure 3.24 and the corresponding harmonic spectrums in Figure 3.25. The calculated waveform distortion characteristics are like those seen in the measurement data, which was shown in Figure 2.1 of Chapter 2. This illustrates that the general kind of waveform obtained from the method developed here is like the response measured in the field test data.

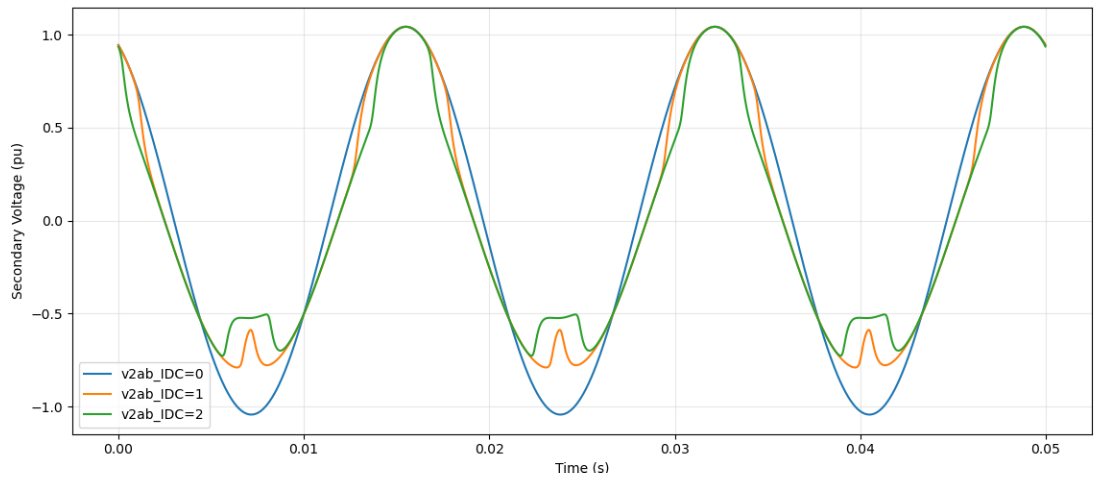

Figure 3.24.-Example secondary voltage waveform calculated using the method developed for asymmetrically saturated substation transformers.

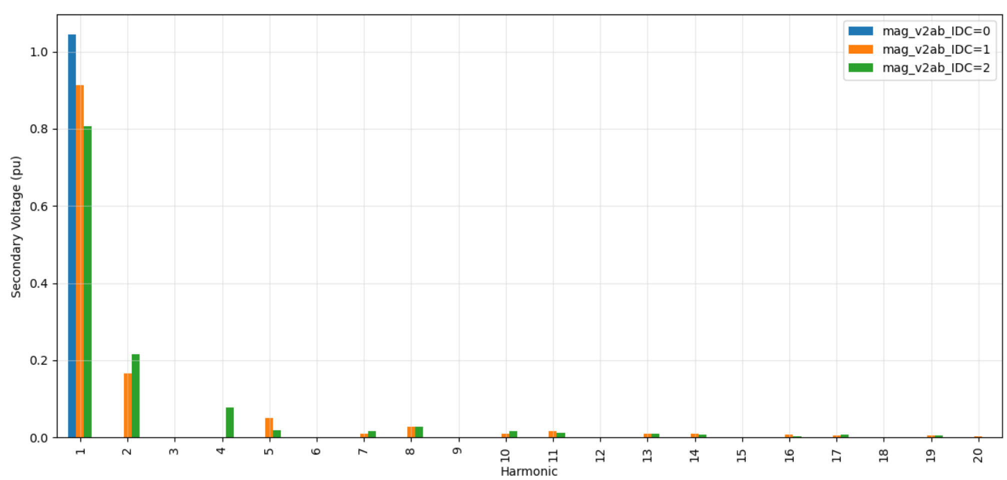

Figure 3.25.-Example secondary voltage harmonic spectrum calculated using the method developed for asymmetrically saturated substation transformers.

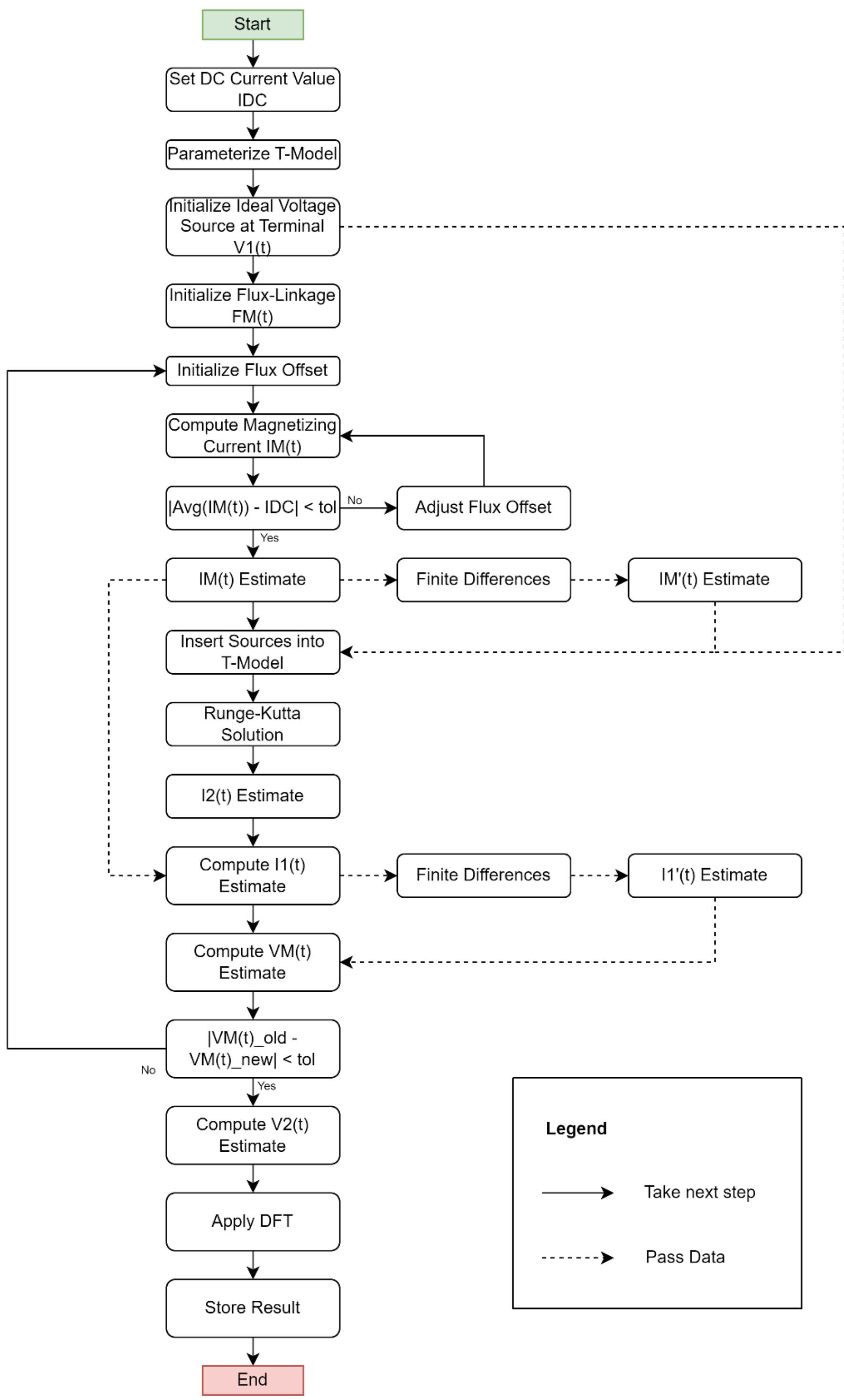

Figure 3.26.-Block diagram of the algorithm used to approximate the transformer secondary voltage in response to DC current flow in the winding.

Secondary voltage response values were computed for inputs spanning the range of transformer parameters presented in the Literature Review section for per-phase DC current values from zero to five per unit. The minimum and maximum of resulting fundamental secondary voltages across the entire parameter set is shown in Figure 3.27, while the same is shown for voltage harmonics two through eight in Figure 3.28. The higher order harmonics up to twenty were computed but are not shown here, as their behavior is qualitatively like those shown. Due to the significant number of combinations required to span the range of parameters, the number of DC current values was limited to 150 points, which causes some choppiness in the plots. The wide range of parameters also resulted in secondary voltages below 0.95 per unit with zero DC current. In practice, voltage on the secondary of a transformer is regulated with taps that allow the ratio of primary to secondary turns to be modified as needed to maintain acceptable voltage, but transformer taps are not considered in this work.

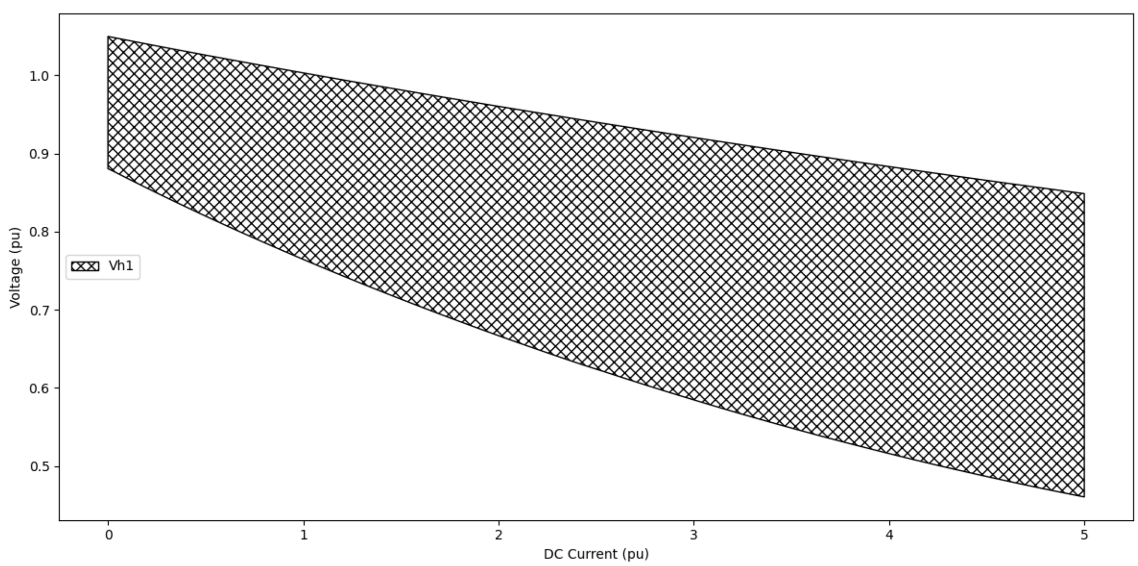

Figure 3.27.-Range of fundamental component of transformer secondary voltage with respect to DC current in the high-side winding.

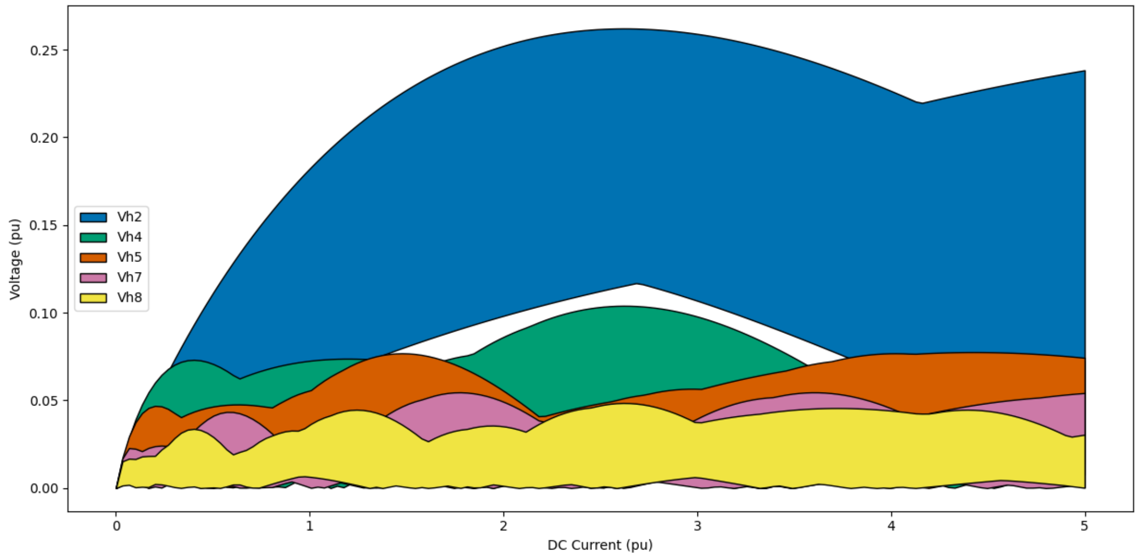

Figure 3.28.-Range of harmonics of transformer secondary voltage with respect to DC current in the high-side winding.

The corresponding minimum and maximum range of total harmonic distortion of the secondary voltage across the parameter set is shown in Figure 3.29.

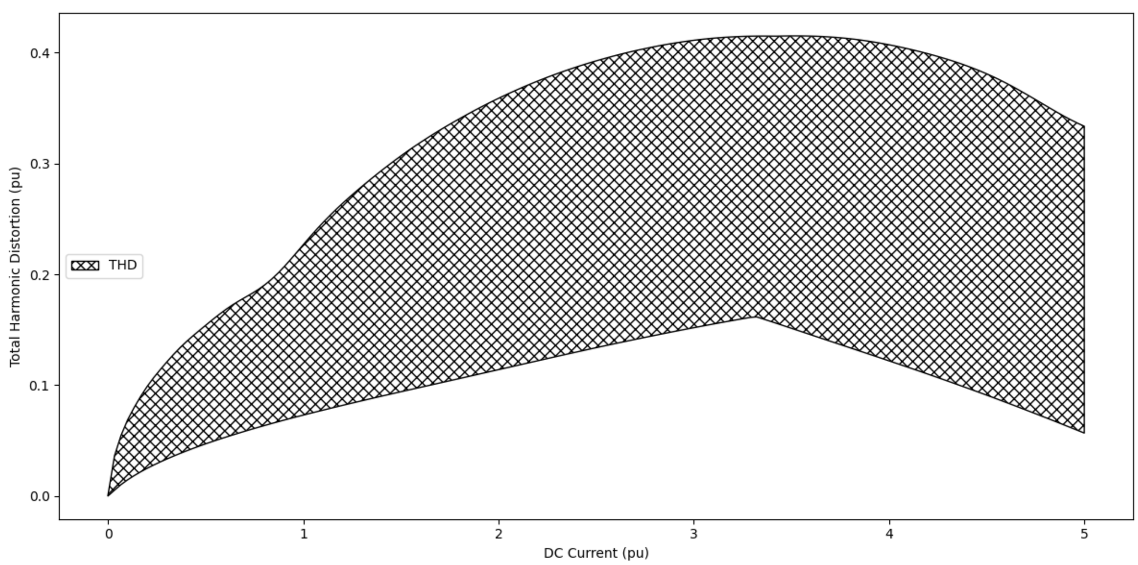

Figure 3.29.-Range of total harmonic distortion of transformer secondary voltage with respect to DC current in the high-side winding.

Comparison of Approximate Secondary Terminal Voltage Source Model and Field Test Measurements

In this section the field test measurements and model calculation responses are compared. The transformer power rating, operating voltage, and the winding configurations are known. However, other parameters of the test transformer are unknown to the present author, as mentioned before. Therefore, the comparison here is to examine the model harmonic responses within a range of realistic transformer parameters against the measured response of an actual transformer. Without the actual parameters of the test transformer, a direct comparison cannot be made, but the qualitative comparison is still useful for validating the model characteristics. Unknown transformer parameters were estimated iteratively using the first five harmonics to produce a similar steady-state settling value during saturation as observed in the test measurements, with respect to the DC current used during the field test. The parameter estimates were within the range of parameters listed in the Literature Review.

Figure 3.30 is a plot of the harmonic current versus the per phase DC current in per unit. It appears that the transformer does not respond until the DC current reaches a high value. However, there is a delay due to the saturation time of the transformer [41]. The model developed in the previous section was used to calculate steady-state harmonic currents across the same range of DC current as shown in Figure 3.31. This result appears qualitatively different than the measurement plot. For each DC current magnitude, the model is producing an estimate of the steady-state settling point, while the field test provides measurements of the time-domain dynamic transition from normal operation to an asymmetric steady-state operating point.

The same field test harmonic currents are plotted versus time in Figure 3.32. The time is adjusted so that time zero is approximately when the DC current injection began. Using the saturation time calculation presented in [41], the DC current values of the model were converted to estimated time values. A plot of the model estimates of harmonic current versus the estimated time is shown in Figure 3.33. From this perspective, the model values more closely resemble the test measurements.

The same series of plots is shown for the secondary voltage harmonics in Figure 3.34 through Figure 3.37. A similar level of correlation is observed between the field measurements and the model estimates when using the estimated time axis computed from the DC current values.

The key observation in this test is that the transformer secondary voltage and current harmonics each traverse a curve as the transformer transitions from zero DC current to a particular non-zero value of DC current. The steady-state model produces harmonic values with the same kind of characteristics seen in the field test data, although the curves have some differences. The observed differences support the need to evaluate a range of transformer parameters in this work.

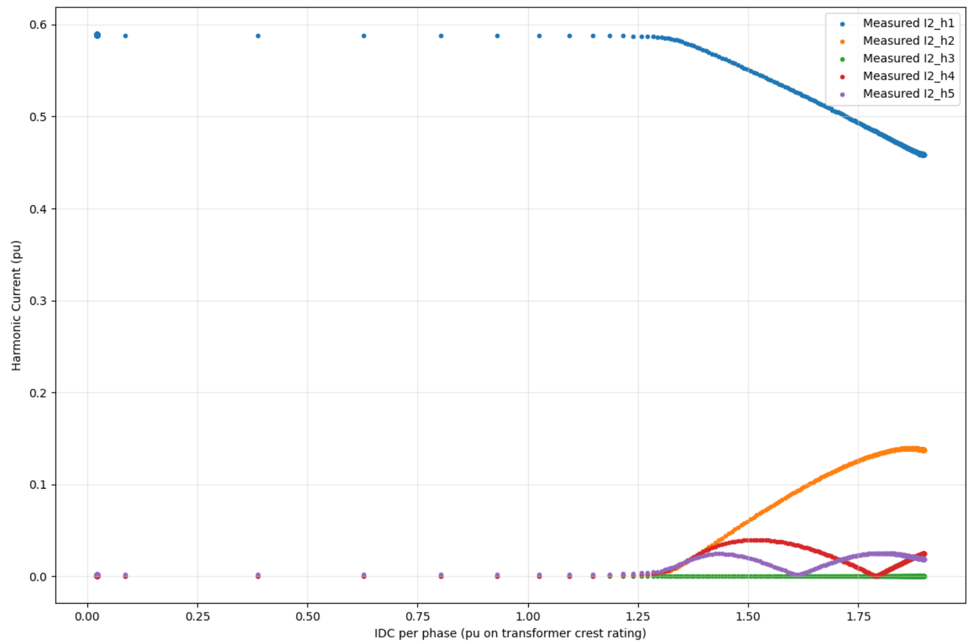

Figure 3.30.-Field test measurement harmonic current with respect to per-phase DC current in the high-side winding.

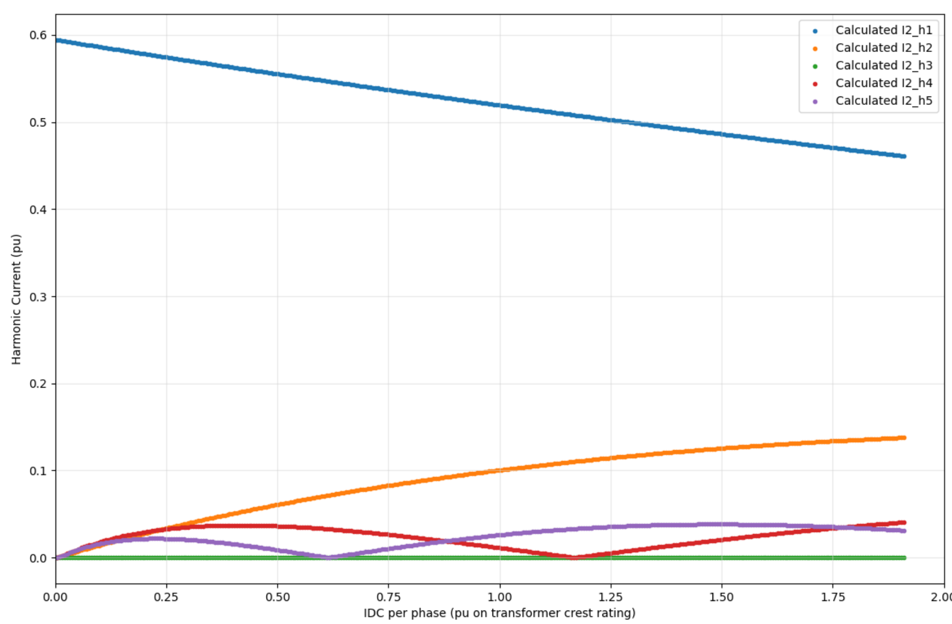

Figure 3.31.-Calculated harmonic current with respect to per-phase DC current in the high-side winding.

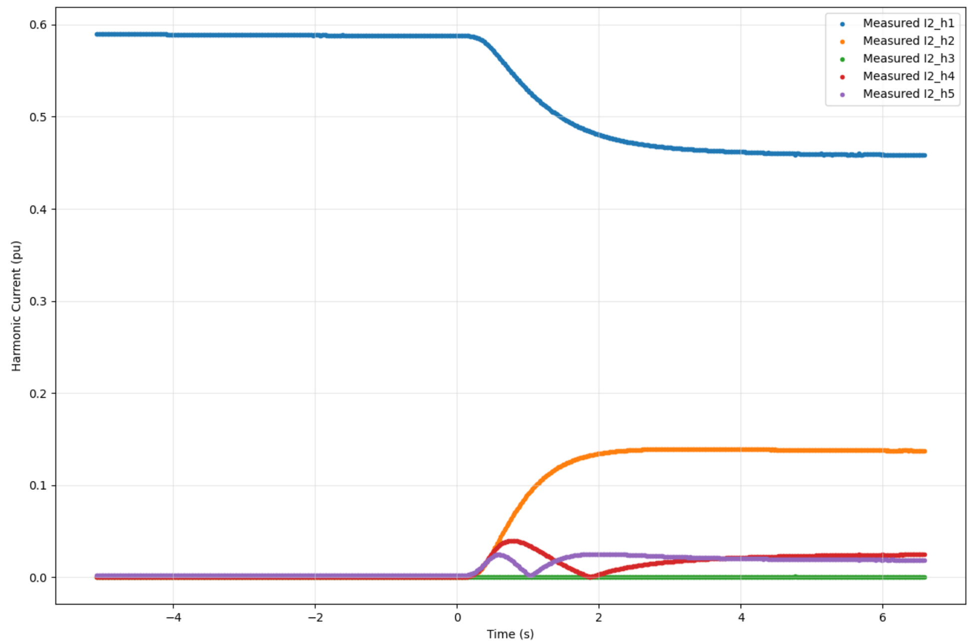

Figure 3.32.-Field test measurement harmonic current with respect to time.

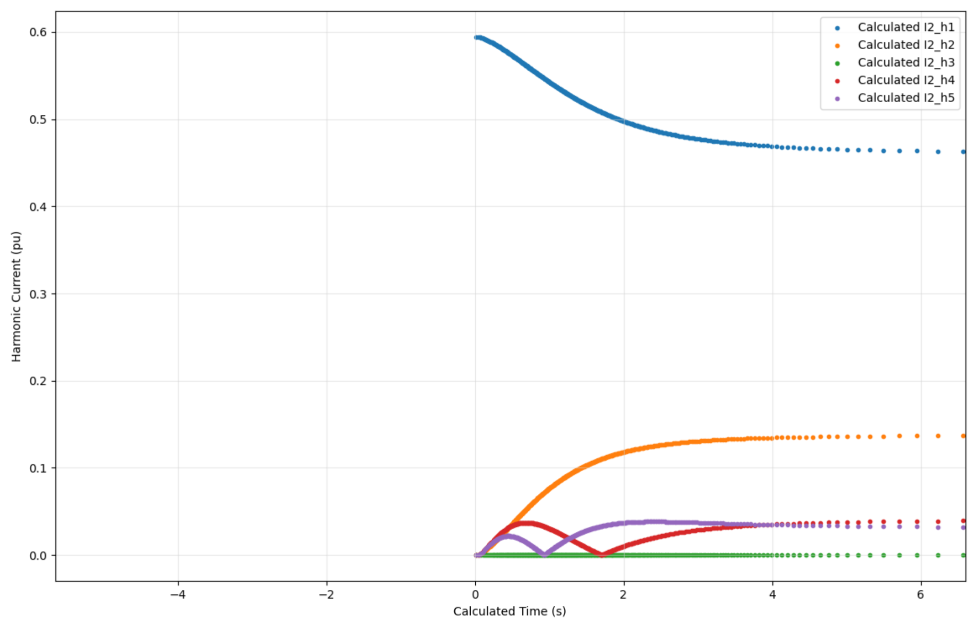

Figure 3.33.-Calculated harmonic current with respect to calculated time estimated using [41].

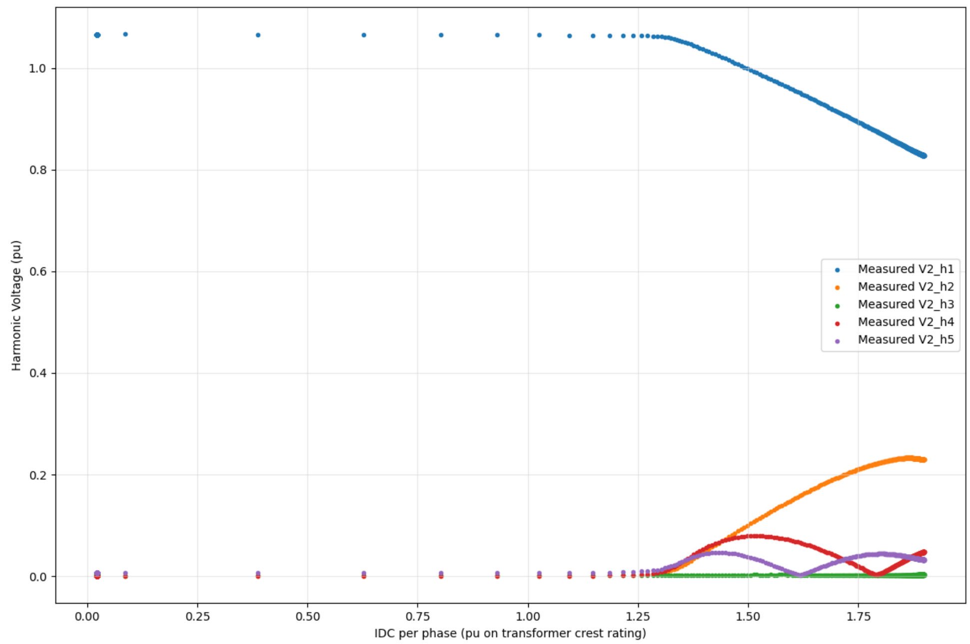

Figure 3.34.-Field test measurement harmonic voltage with respect to per-phase DC current in the high-side winding.

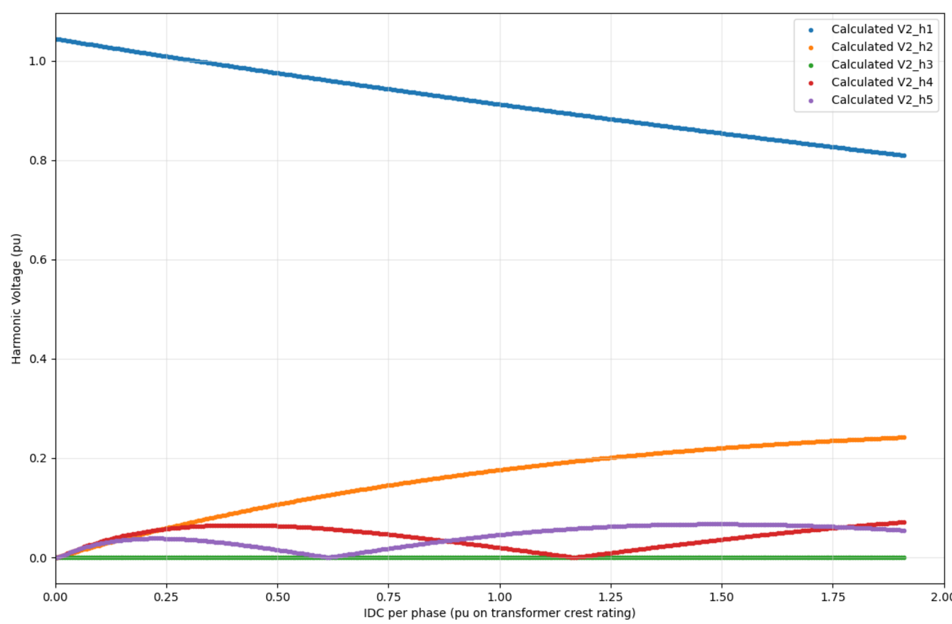

Figure 3.35.-Calculated harmonic voltage with respect to per-phase DC current in the high-side winding.

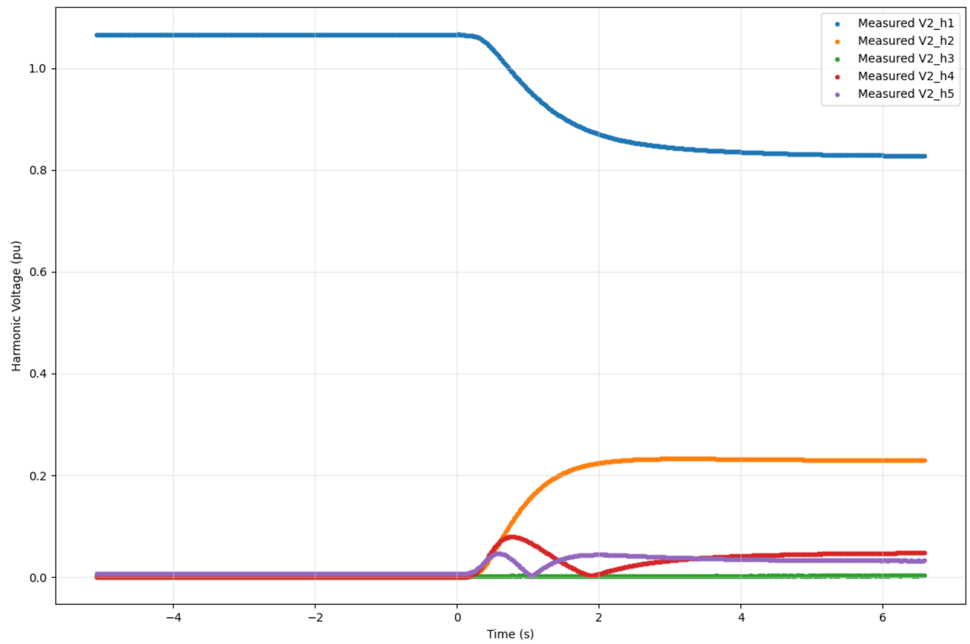

Figure 3.36.-Field test measurement harmonic voltage with respect to time.

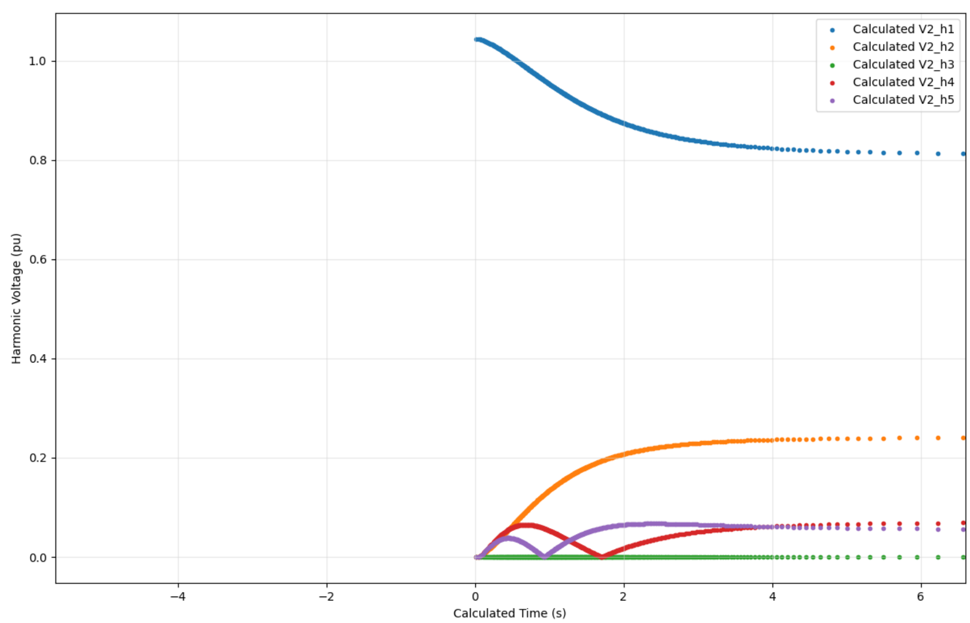

Figure 3.37.-Calculated harmonic voltage with respect to calculated time estimated using [41].

Summary

Using the basic relationships between voltage, current, and inductance and combining the method published in [25] and [26] with the flux-linkage current relationship in [5], a model has been developed to approximate the steady-state non-linear transformer magnetizing current as a function of DC current flowing in the transformer winding. The magnetizing current source was combined with the transformer t-model to approximate the steady-state secondary terminal response of the transformer. The model response was evaluated parametrically across a range of realistic input parameters for utility transformers and a range of responses were plotted. Finally, the model response was qualitatively compared with field test measurements for an actual substation transformer. The model provides responses that are characteristic of the response observed in the field test data.

The method and response results developed here will not apply equally to all transformer types. Since some magnetic cores have asymmetric saturation characteristics on different portions of the core, the magnetic saturation response must be determined simultaneously for the three-phase circuit by solving the magnetic circuits [26], [45]. Therefore, the results obtained using the model developed here are unable to represent the variety of transformer responses that may occur in an actual power system but are instead confined to transformers similar in type to the field test transformer. In addition, many substation transformers have a delta configuration of the high-side windings, and therefore do not offer a ground connection for DC current flow between the earth and the high-voltage transmission system.

CHAPTER FOUR

Harmonic Powerflow Simulation of Distribution Feeders Energized by an Asymmetrically Saturated Substation Transformer

Introduction

In this chapter, the steady-state behavior of realistic feeders energized by asymmetrically saturated transformers will be approximated using harmonic powerflow simulations. The DC current flow at transformer nodes during a simulated E3 event with a synthetic grid and a realistic earth model were reported to approach 75 amps per phase in [46]. Although more work is needed to determine realistic boundaries of transformer DC currents during an E3 event, 75 amps will be used in this evaluation of feeder response. The transformer secondary terminal voltage source model will be used to approximate a range of steady-state harmonic spectrums for DC current values between 0 and 75 amps per phase based on substation transformer high-side power and voltage ratings. Within the simulations, the harmonic voltage source model is used to energize the substation bus while voltage at points along the distribution feeder model are monitored. The response will be summarized and compared to the normal system operating boundaries summarized in the Literature Review.

Distribution System Models and Harmonic Powerflow Simulation Process

The EPRI CKT5, CKT7, and CKT24 models are included with the OpenDSS software installation. These models represent different distribution systems and are made available for research. The harmonic spectrums are based on the per unit values of DC current on the substation transformer base for each of the EPRI CKT models. The substation transformers in each model had a delta high-side winding configuration, which would not experience DC current flow during an E3 event. Therefore, the results obtained here assume that the feeders are energized by a substation transformer that has a grounded-wye winding configuration on the high-side.

To accommodate harmonic powerflow simulation, some modifications were made to the EPRI distribution system models that were included with the OpenDSS software installation. Circuit elements with nominal voltages higher than the substation bus were removed, including the substation transformer. The substation bus is energized by the harmonic voltage source developed earlier, as the model was developed to produce the steady-state secondary terminal behavior directly.

After updating the model, the standard powerflow simulation is performed to check for convergence of the model and initialize for harmonic simulation. Then a frequency scan is performed by sweeping an equal voltage magnitude across each harmonic while monitoring the current response at each frequency. The technique used is similar to that described in the OpenDSS examples [47], but here using a voltage source instead of a current source. Finally, harmonic powerflow simulations are performed for each of the computed harmonic voltage spectrums. The simulation process is summarized in Figure 4.1.

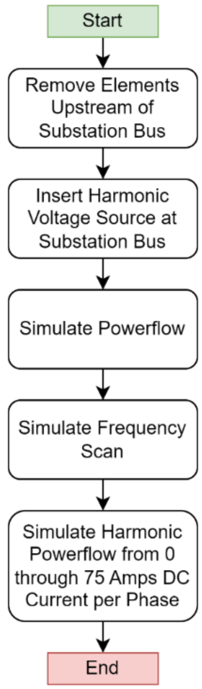

Figure 4.1.-Block diagram of the harmonic powerflow simulation process.

THD and RMS values were computed using the equations from [48], which are below.

$$THD = \frac{\sqrt{\sum_{h>1}^{hmax} M_N^2}}{M_1} \tag{4.1}$$

$$\text{RMS} = \sqrt{\sum_{h=1}^{hmax} M_N^2} = M_1\sqrt{1 + THD^2} \tag{4.2}$$

The voltage peak values are computed by applying the IDFT to the harmonic spectrum outputs of the simulation and then taking the waveform sample with the largest magnitude from the resulting waveform.

Model Setup and Harmonic Frequency Scans

The EPRI CKT5 substation transformer model has the lowest high-side base current rating among the three distribution system models, which is about 50 amps. The

75 amps of DC current being considered here will be about 1.5 per unit on the transformer base. One important note is that large power transformers typically employ special cooling techniques to increase the power rating, which means that the per unit values of DC current calculated here may be lower than for the actual transformer. Since the base rating of the transformer was not in the model, the provided rating was assumed as the base. This means that the actual transformers may go deeper into saturation for 75 amps of DC current per phase than evaluated here.

Referring to Figure 3.27 and Figure 3.28, an approximate estimate can be obtained for the full range of harmonic voltages to expect from the model for 1.5 per unit DC current. To reduce the volume of harmonic powerflow simulations that follow, the only transformer primary voltage considered was 1.05 per unit. This will provide some offset for the fact that voltage regulating taps are not considered in the harmonic voltage source model. In addition, two parameters that were observed to have less impact during deep saturation were limited to a single value instead of the range listed in the Literature Review. The nominal magnetizing current considered was 1 percent and the core saturation knee point considered was 1.15 per unit. Therefore, the range of values simulated at the substation bus will be narrower than the model response shown in Figure 3.27 and Figure 3.28.

After removing the substation transformer and inserting the harmonic voltage source at the substation bus, the standard powerflow was simulated to check that the fundamental solution is converged and to initialize for harmonic simulation. Then a harmonic frequency scan was performed assuming peak loading conditions where available capacitor banks were online. Figure 4.2 shows the corresponding current flowing out of the substation bus. The plot shows that the CKT5 distribution system will absorb more current for a given voltage at certain frequencies, especially between 600 Hz and 800 Hz. This indicates that harmonic voltages produced by the asymmetrically saturated transformer between 600 Hz and 800 Hz at the substation bus may be amplified at points within the distribution system.

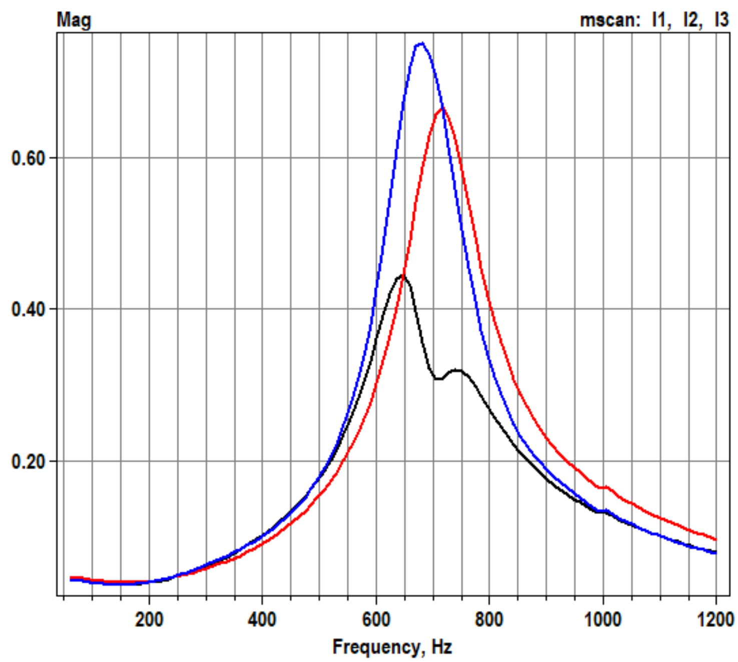

Figure 4.2.-Frequency scan results for EPRI CKT5 model with all capacitor banks online.

If the capacitor banks are offline, the frequency scan changes to that of Figure 4.3. Without capacitor banks, the harmonic currents are significantly less than before, and the resonant points disappear. A distribution system may have some or all capacitor banks offline to prevent high voltages during light load conditions. The frequency scans show that capacitor banks will have significant influence on the harmonic response of a distribution system during asymmetric saturation of the substation transformer.

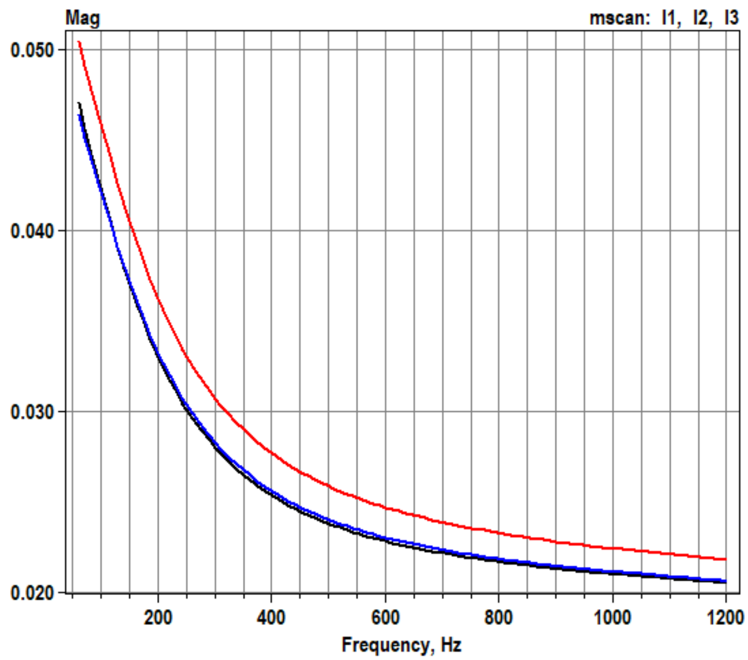

Figure 4.3.-Frequency scan results for EPRI CKT5 model with all capacitor banks offline.

After making the necessary model changes, the frequency scan was produced for the EPRI CKT7 model with all capacitor banks online, and the resulting harmonic currents are shown in Figure 4.4. The resonant point for this distribution system under this condition occurs between 500 Hz and 700 Hz. Again, without capacitor banks the amplified currents disappear as seen in Figure 4.5.

The same analysis was performed for the EPRI CKT24 model, and the frequency scan results are shown in Figure 4.6 and Figure 4.7. The resonant points for this system occur between 700 Hz and 1000 Hz, but with much lower magnitudes than seen in the CKT5 and CKT7 systems.

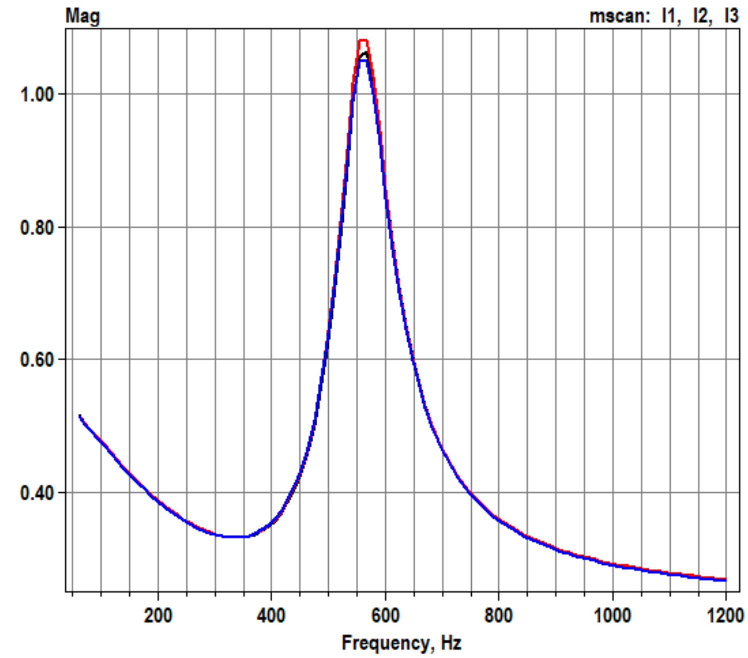

Figure 4.4.-Frequency scan results for EPRI CKT7 model with all capacitor banks online.

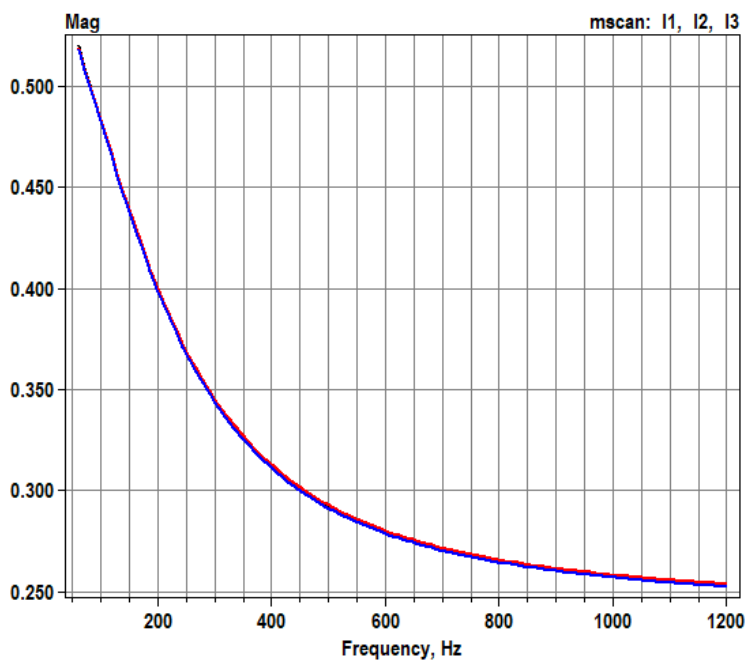

Figure 4.5.-Frequency scan results for EPRI CKT7 model with all capacitor banks offline.

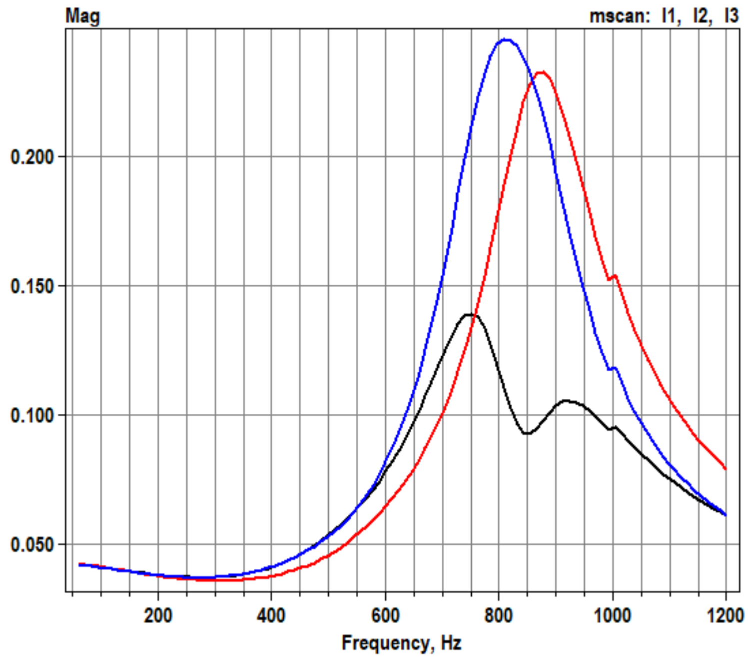

Figure 4.6.-Frequency scan results for EPRI CKT24 model with all capacitor banks online.

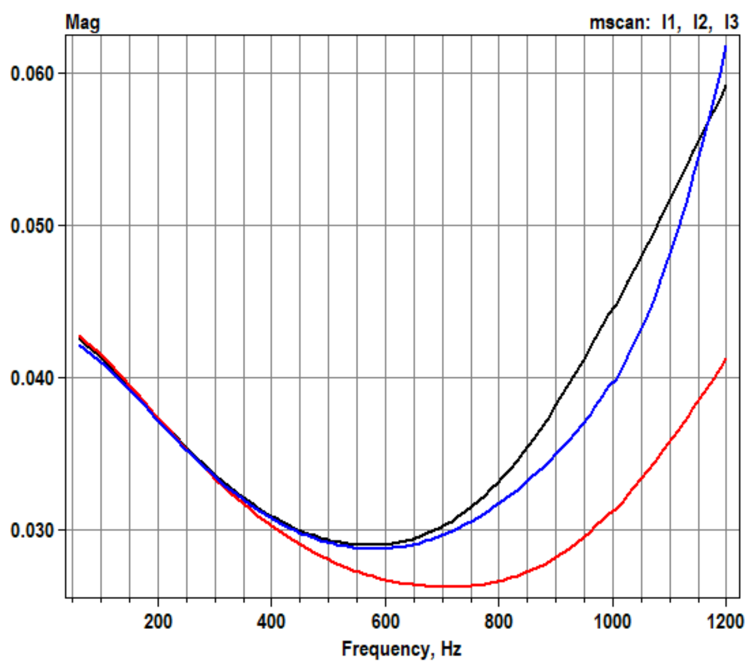

Figure 4.7.-Frequency scan results for EPRI CKT24 model with all capacitor banks offline.

Harmonic Powerflow Simulation of the EPRI CKT Models

A sequence of harmonic powerflow simulations was performed to examine feeder response to high-side DC currents between 0 and 75 amps. Due to practical space and time limits for the high volume of simulations needed to cover a wide range of transformer parameters, voltage was only monitored at the substation and the capacitor banks for these simulations. Other nodes within the feeder model can experience values outside of those identified in this section but will not be visible in the simulation outputs. That limitation will be addressed in the next section.

The range of total harmonic distortion for the CKT5 model is shown in Figure 4.8, along with a red line showing the upper THD limit of 5%. Only about 25 amps of DC current per phase was required for the distribution system to exceed the THD limits for the entire transformer parameter range. At 75 amps per phase of DC current flowing in the high-side winding of this transformer, the THD on the distribution side is far beyond the defined limit. One contributing factor is the extremely low fundamental component of voltage, which appears in the denominator of the THD equation.

The range of waveform peaks is shown in Figure 4.9, along with a red line showing the upper voltage limit of 1.2 per unit for capacitor banks. The limit is exceeded beginning at 10 amps of DC current, but only for transformer parameter combinations leading to the worst case peaks. Many of the simulated transformer parameters did not result in peaks exceeding the limit. Trips or damage to capacitor banks could occur for voltage peaks that are high but below the limit and capacitor banks may be lost based on criteria that are not considered in this work, such as overcurrent protection. Therefore, sensitivity analysis will be performed later to assess the impact of losing capacitor banks during an event.

The range of RMS voltages is shown in Figure 4.10 with the upper CBEMA voltage limit shown in red and the lower CBEMA voltage limit shown in blue. The upper limit was not exceeded by any of the monitored nodes across the range of parameters tests. The lower limit was exceed beginning at about 20 amps of DC current. Some load loss may be expected at feeder nodes experiencing voltages this low. About half of the scenarios resulted in RMS voltages below the typical emergency limit of 0.90 per unit at 75 amps of DC current. The fundamental frequency component of voltage in Figure 4.11 is shown for reference, since many devices in the power system, such as protective relays, respond to fundamental frequency components by applying a 60 Hz filter to their measurement signals.

Finally, the range of harmonic voltages observed at the 75 amp DC level is shown in Figure 4.12. Low 60 Hz voltages and high second harmonic are visible. The 3% individual harmonic limit is exceeded at multiple frequencies. The CKT5 circuit frequency scan indicated that some amplification around the 11^{th} harmonic might be expected, and this is visible in the plot. The 11^{th} harmonic response will be explored further in the next section.

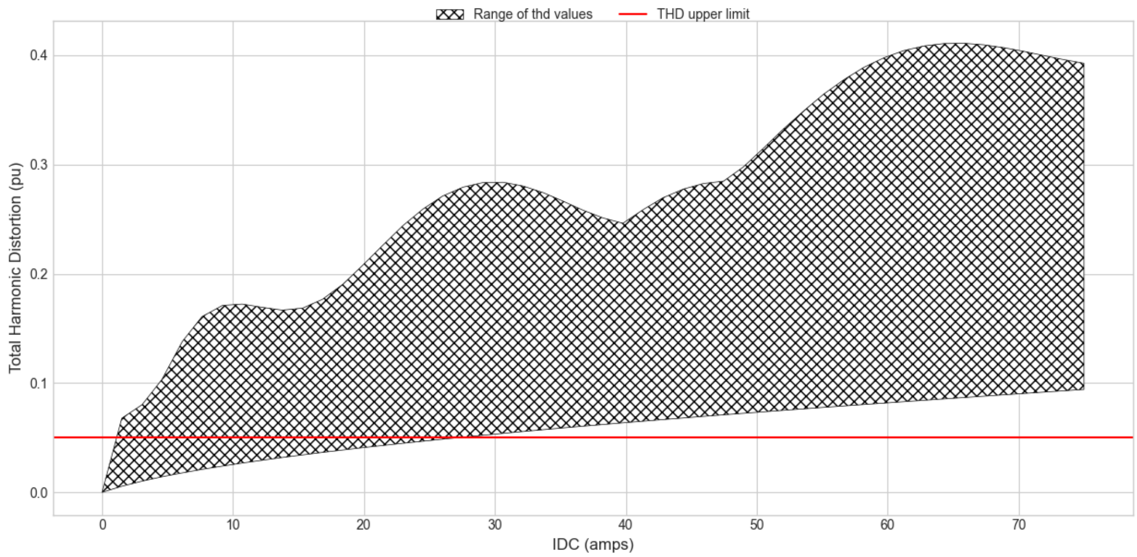

Figure 4.8.-Range of total harmonic distortion observed across substation and capacitor bank nodes within the EPRI CKT5 model.

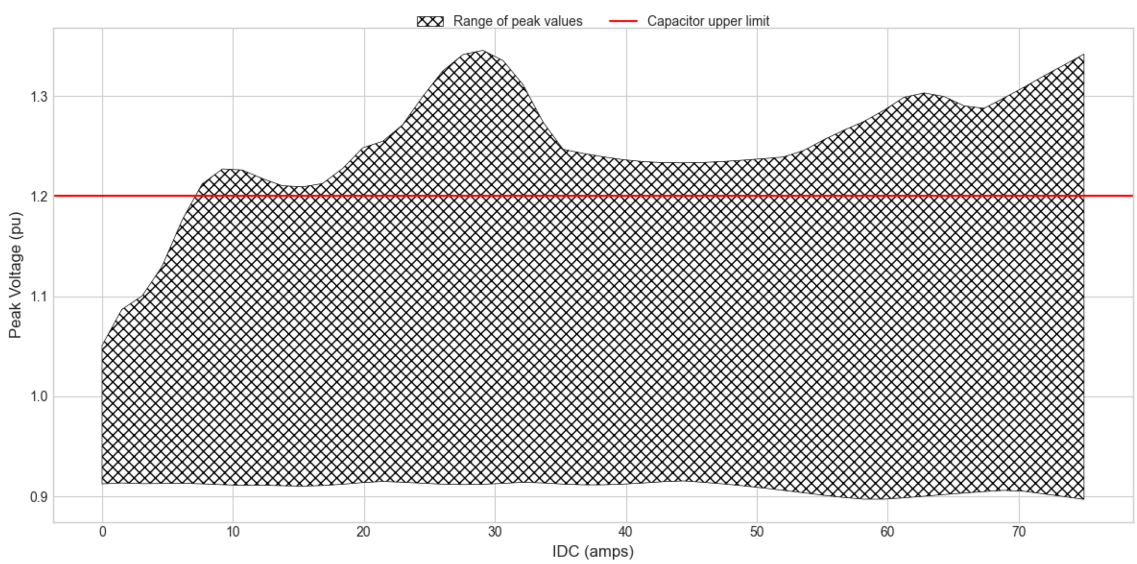

Figure 4.9.-Range of voltage waveform peaks observed across substation and capacitor bank nodes within the EPRI CKT5 model.

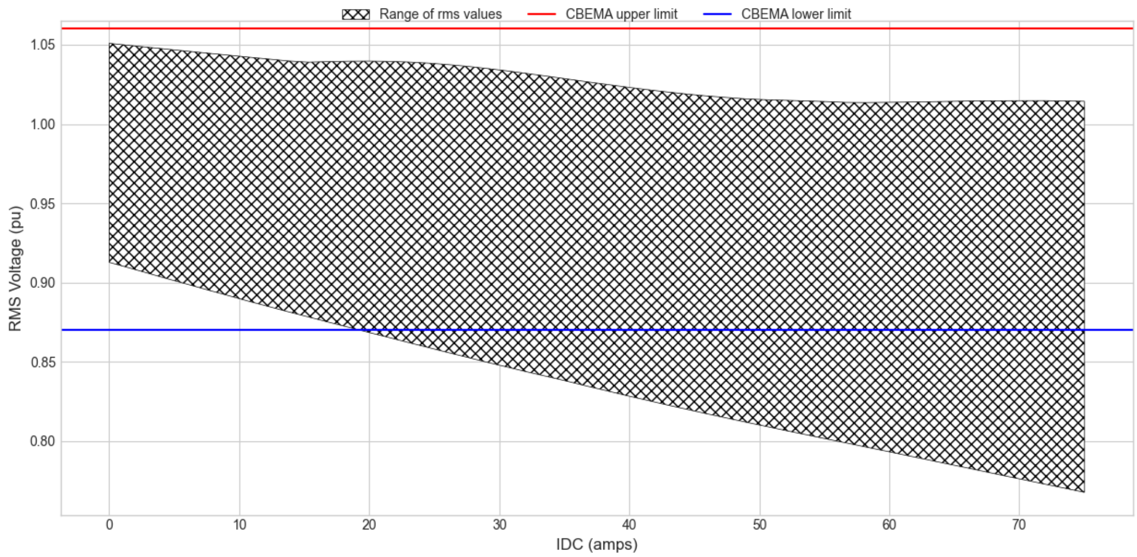

Figure 4.10.- Range of RMS voltage observed across substation and capacitor bank nodes within the EPRI CKT5 model.

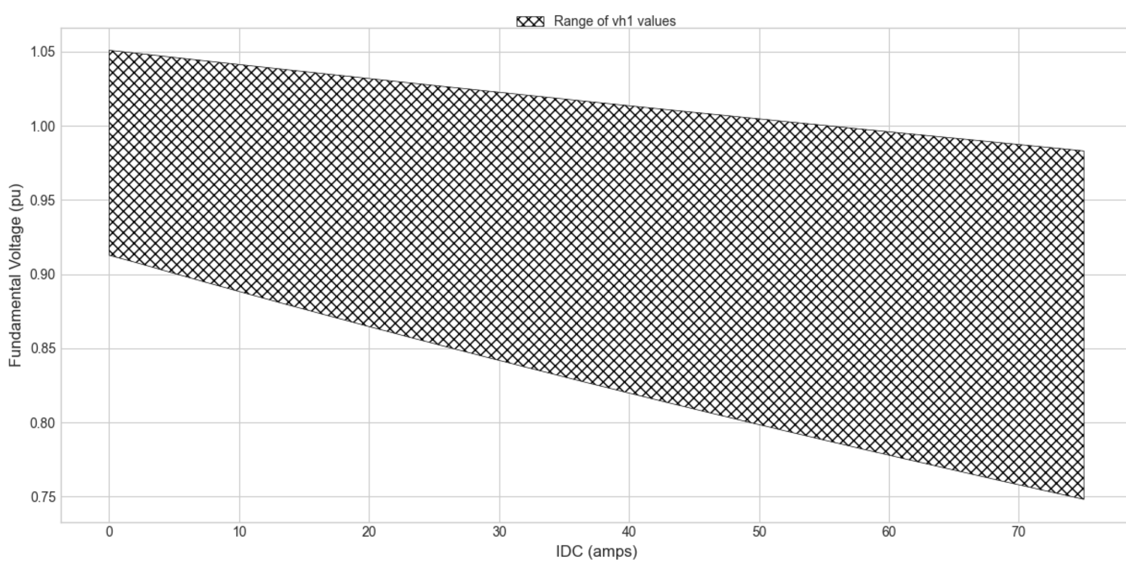

Figure 4.11.- Range of fundamental component of voltage observed across substation and capacitor bank nodes within the EPRI CKT5 model.

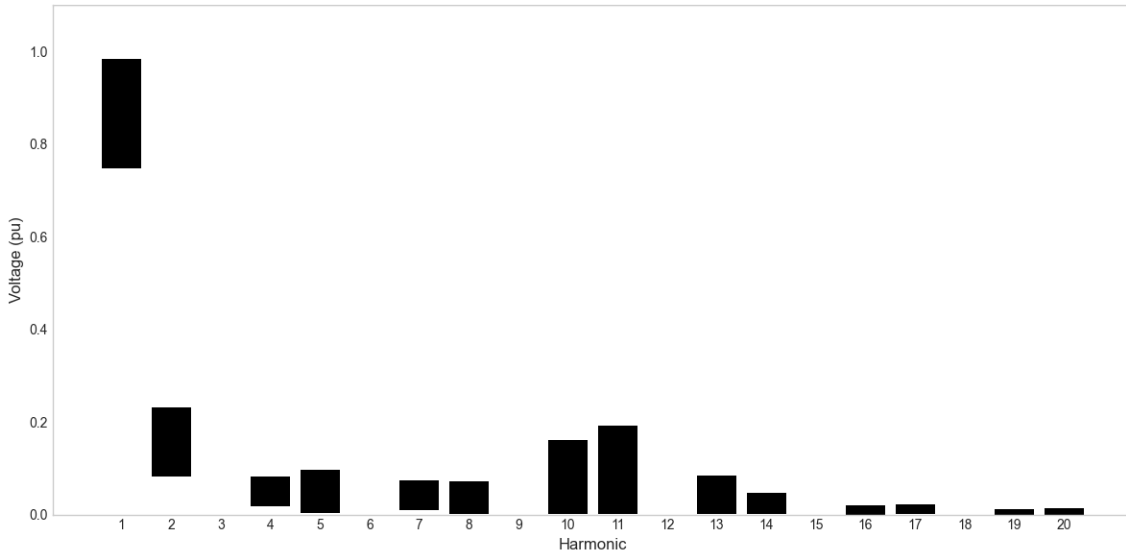

Figure 4.12.-Range of harmonic voltages observed across substation and capacitor bank nodes within the EPRI CKT5 model at 75 amps DC current per phase.

Analysis of the EPRI CKT7 model simulation results showed some amplification between the 8th and 11th harmonics, as expected from the frequency scan results. The frequency scan also showed high values around the 9th harmonic, but triplen harmonic are not present in the field test measurement data. The harmonic components were eliminated in the model output when the wye-delta conversion was applied to account for the delta winding. Therefore, the developed source model does not have any 9th harmonic component and amplification by the feeder circuit in this simulation is not possible.

Again, limit exceedances were observed in the CKT7 model simulation results, including THD, voltage peak, and individual harmonic limits. The response was less severe than seen in the CKT5 model, as can be seen by examining Figure 4.13 through Figure 4.17. The high-side current rating of this substation transformer was higher than that of the CKT5 model, so this transformer did not go as deep into saturation for the 75 amps of DC current.

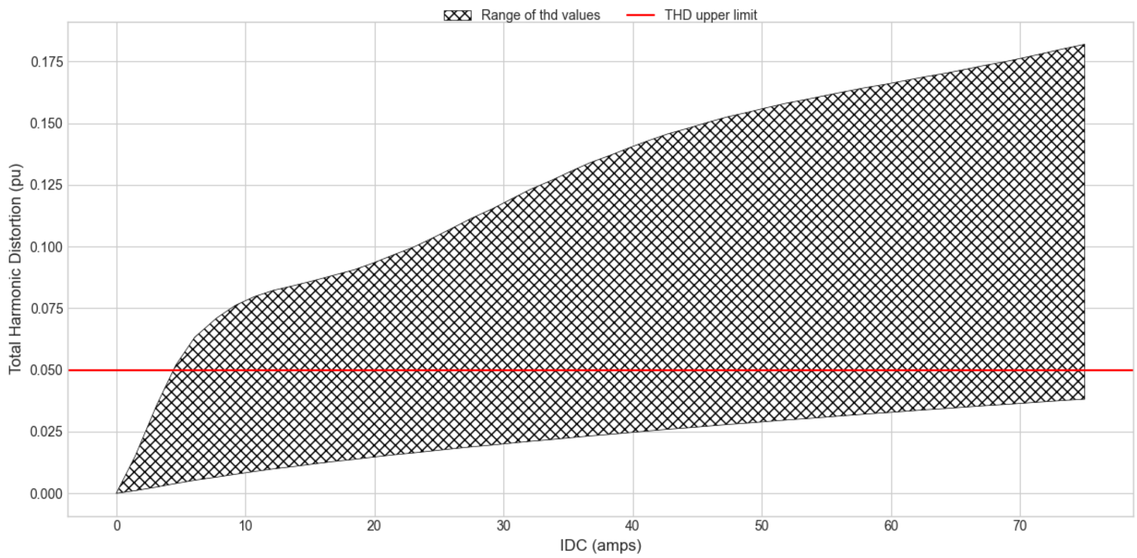

Figure 4.13.-Range of total harmonic distortion observed across substation and capacitor bank nodes within the EPRI CKT7 model.

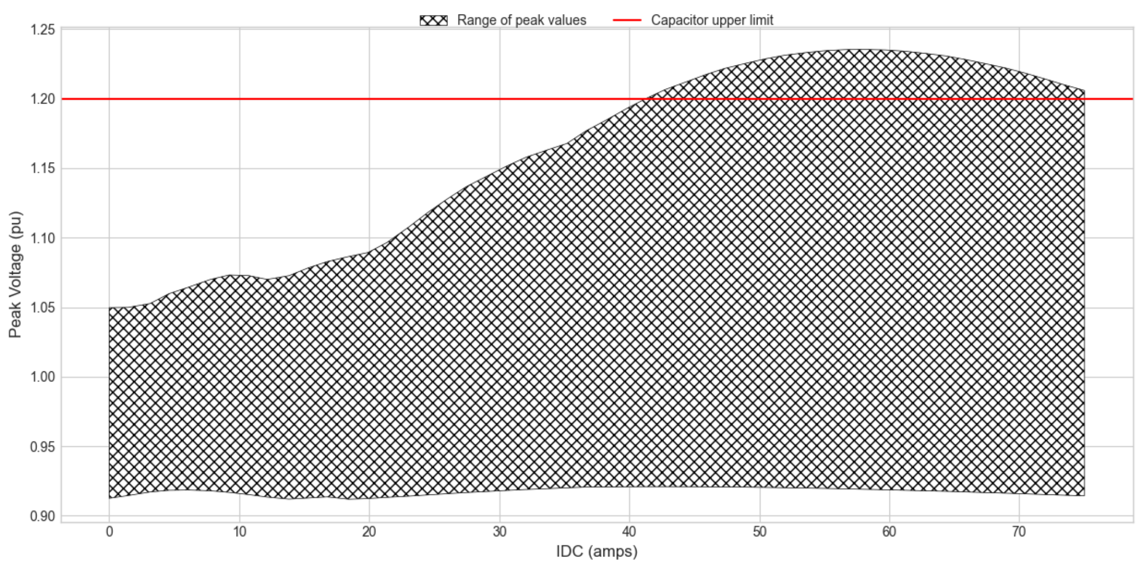

Figure 4.14.-Range of voltage waveform peaks observed across substation and capacitor bank nodes within the EPRI CKT7 model.

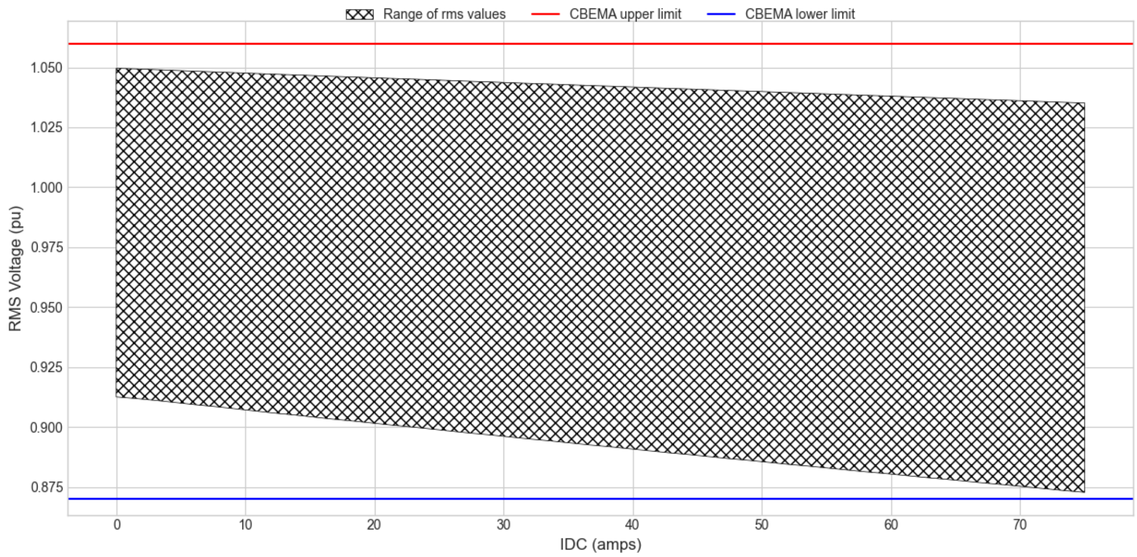

Figure 4.15.-Range of RMS voltage observed across substation and capacitor bank nodes within the EPRI CKT7 model.

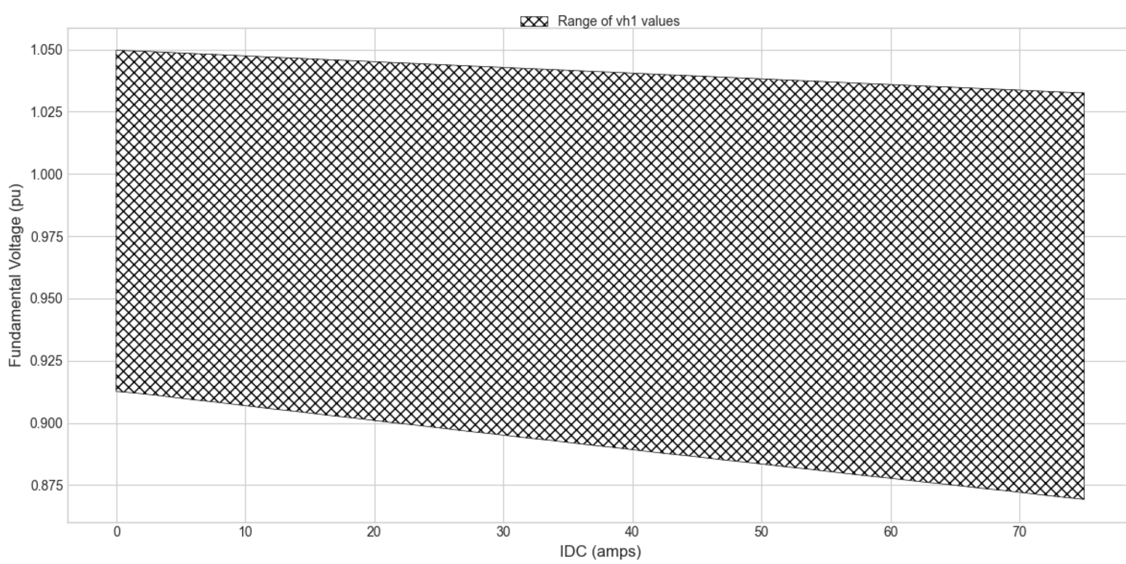

Figure 4.16.- Range of fundamental component of voltage observed across substation and capacitor bank nodes within the EPRI CKT7 model.

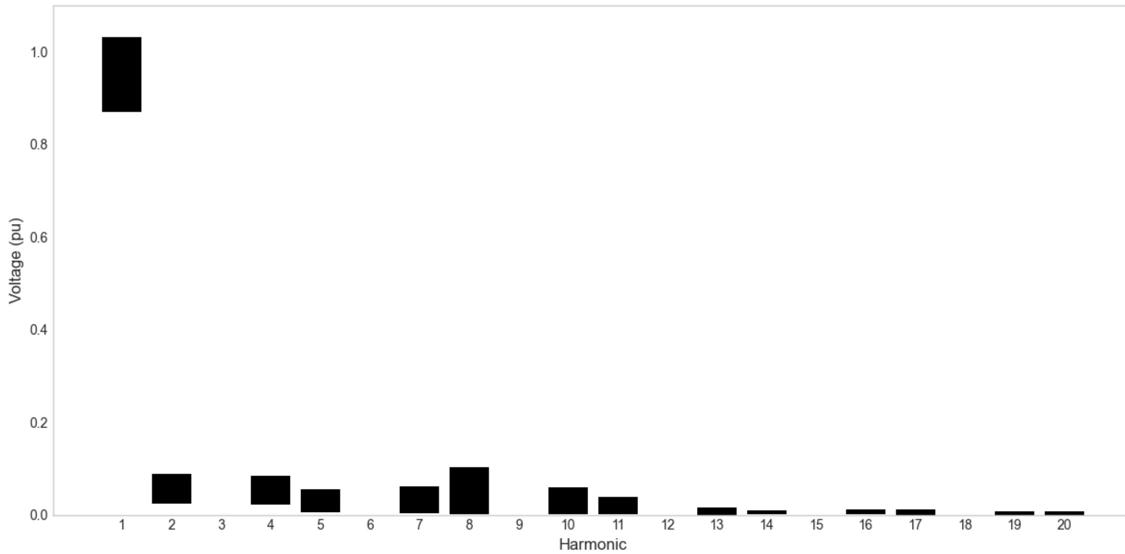

Figure 4.17.-Range of harmonic voltages observed across substation and capacitor bank nodes within the EPRI CKT7 model at 75 amps DC current per phase.

The EPRI CKT24 model response fell between the CKT5 and CKT7 results. Besides the THD limit exceedance beginning at about 5 amps of DC current, the CKT24 model had a small portion of scenarios where voltages fall below the CBEMA lower limit and some scenarios with peak voltages above the capacitor upper limit. The results are summarized by Figure 4.18 through Figure 4.22.

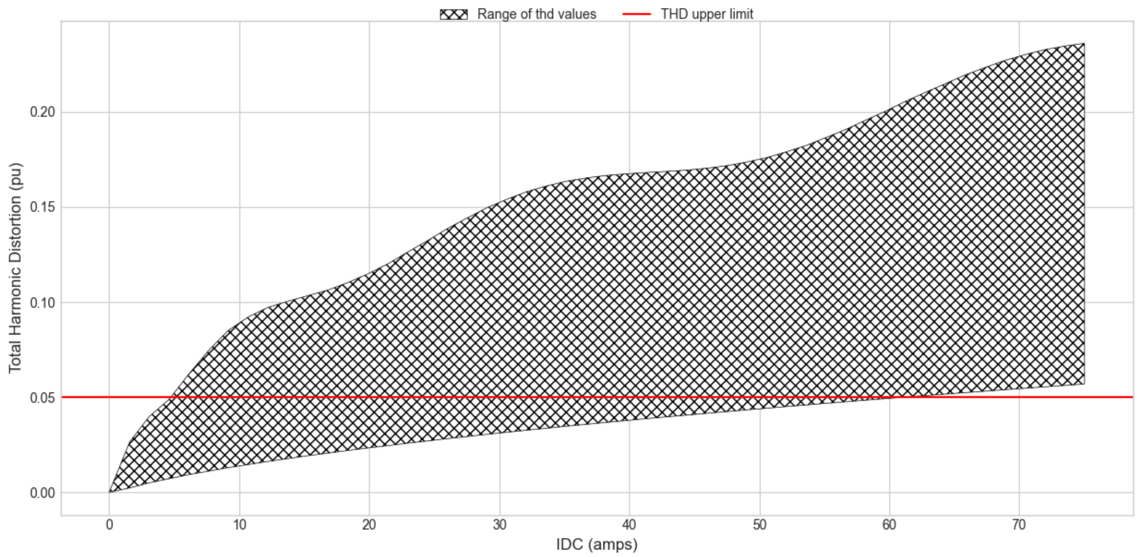

Figure 4.18.-Range of total harmonic distortion observed across substation and capacitor bank nodes within the EPRI CKT24 model.

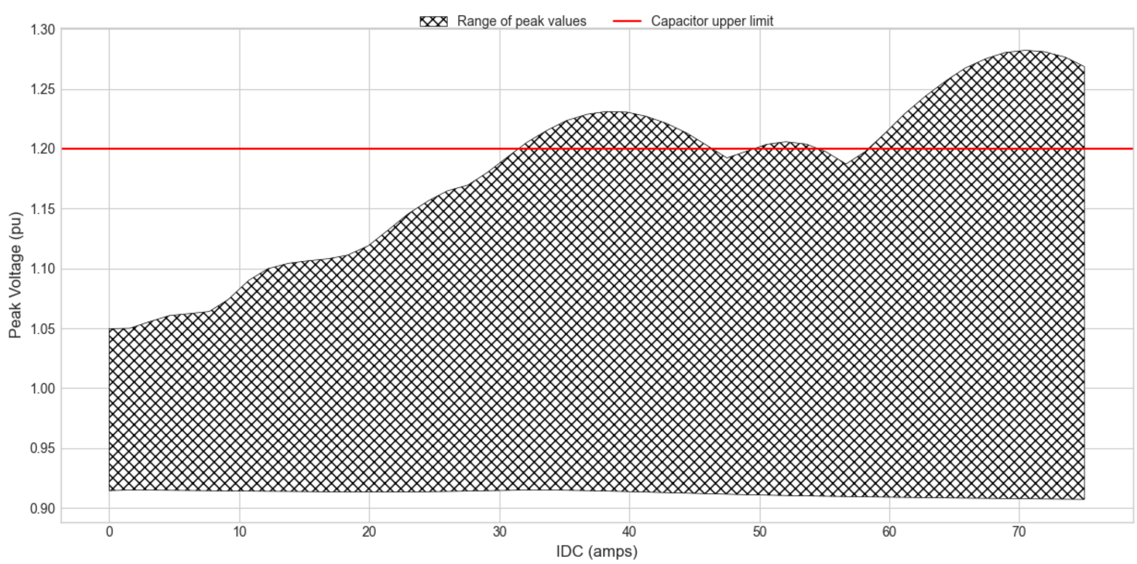

Figure 4.19.-Range of voltage waveform peaks observed across substation and capacitor bank nodes within the EPRI CKT24 model.

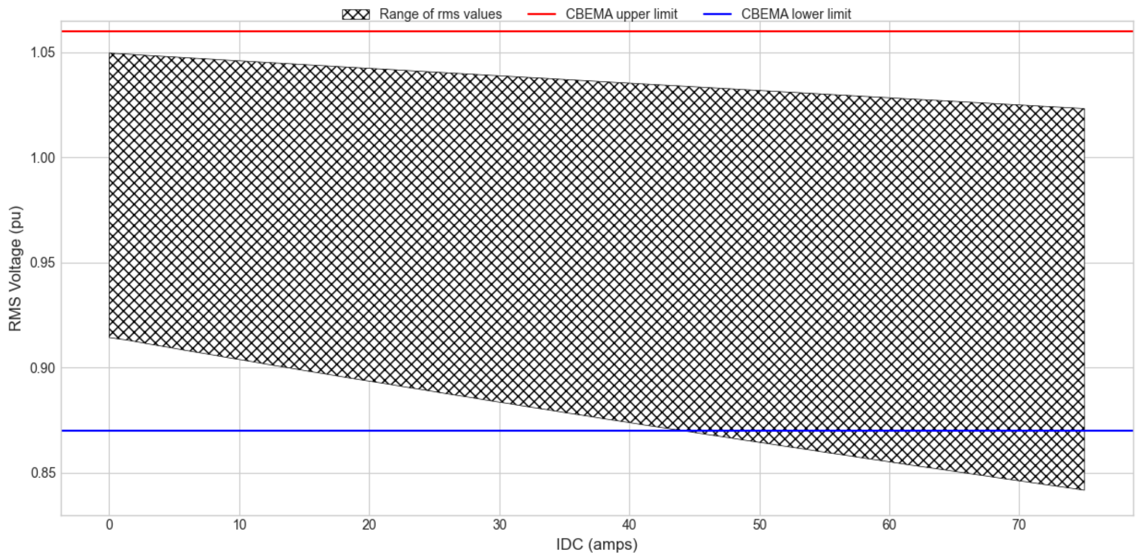

Figure 4.20.-Range of RMS voltage observed across substation and capacitor bank nodes within the EPRI CKT24 model.

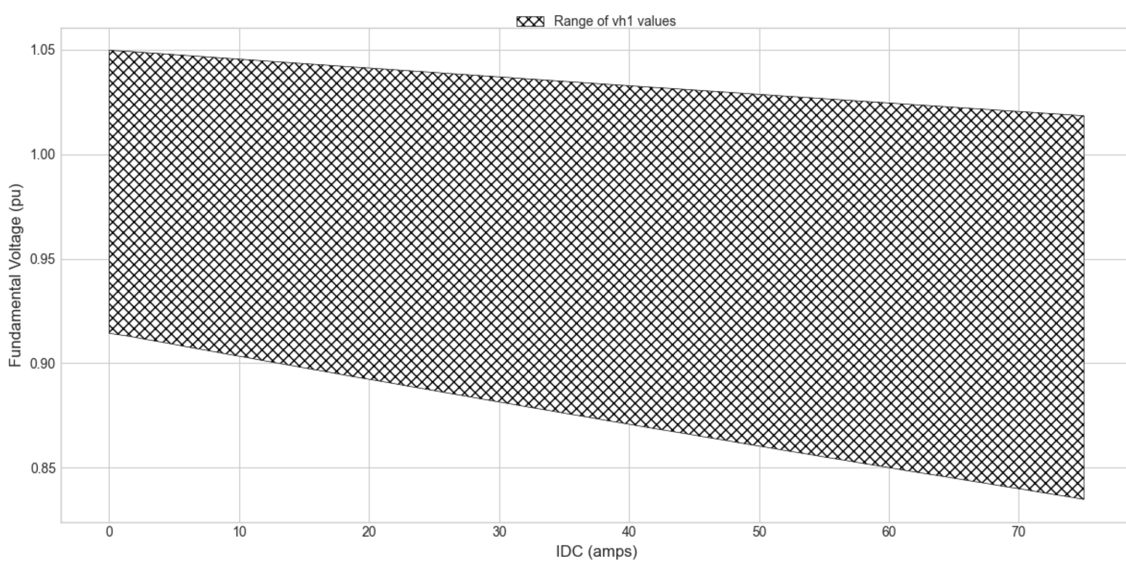

Figure 4.21.- Range of fundamental component of voltage observed across substation and capacitor bank nodes within the EPRI CKT24 model.

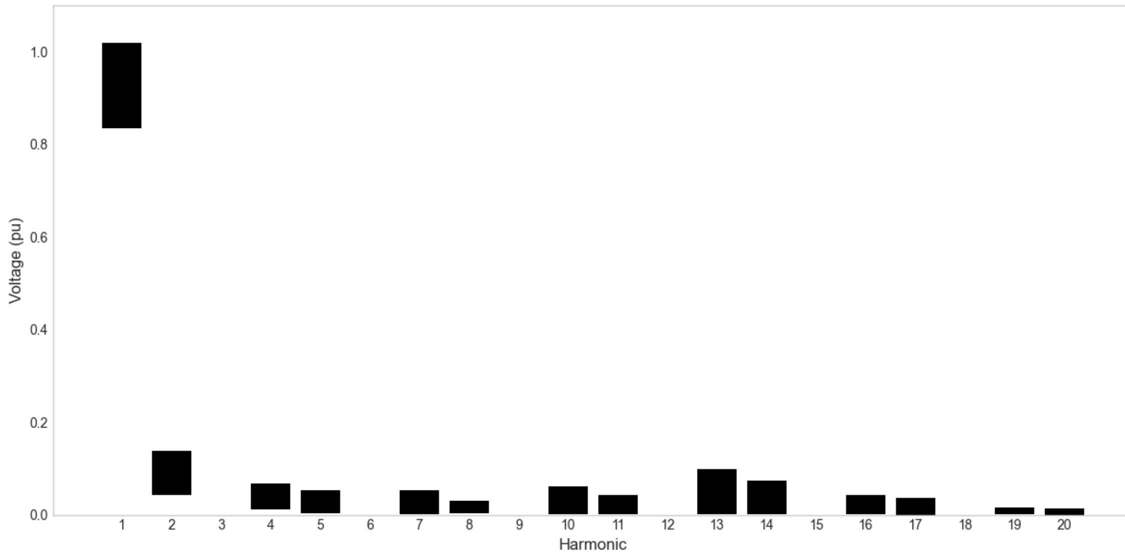

Figure 4.22.- Range of harmonic voltages observed across substation and capacitor bank nodes within the EPRI CKT24 model at 75 amps DC current per phase.

Feeder Response Visualization and Sensitivity Analysis

The general response ranges provided in the previous section evaluated the maximum and minimum values seen at the substation and capacitor nodes across thousands of simulations accounting for transformer parameter variation and different levels of DC current. Because the harmonic load model assumptions are expected to have a significant impact on the simulation results, the EPRI CKT5 model will be used to perform additional simulations to assess the relative impact of the %SeriesRL setting within the OpenDSS load model. The harmonic simulations were performed for one voltage spectrum used in the previous simulations for the CKT5 model that corresponds to 75 amps per phase DC current flowing in the high-side winding of the substation transformer with an observed THD in the middle of the range.

Since only one harmonic spectrum simulation is needed for each scenario in this section, significantly more nodes within the feeder can be monitored. Figure 4.23 shows the monitored locations within the CKT5 model, which are denoted by pink dots. In this diagram, the substation bus is marked with a green square and the feeder capacitor banks are marked with a green cross. For reference, Figure 4.24 highlights the three-phase main primary voltage nodes that are among those monitored. Sensitivity analysis results will be displayed visually using this kind of diagram, where the magnitude of a particular voltage quantity at each bus is indicated by the intensity of the color as compared to a color bar on the right side of the figure.

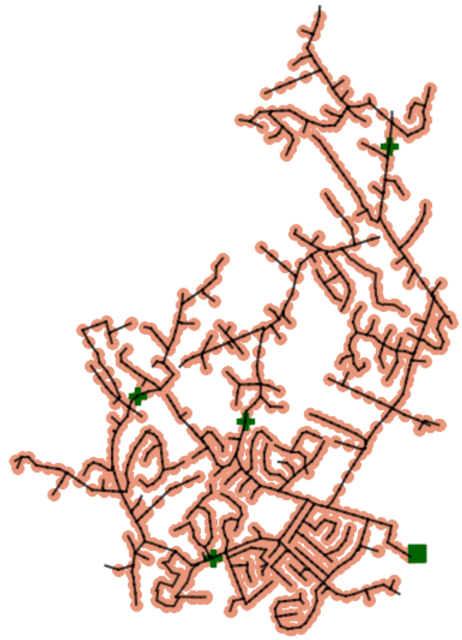

Figure 4.23.-Oneline diagram of the EPRI CKT5 model showing the location of monitored nodes.

Figure 4.24.-Oneline diagram of the EPRI CKT5 model showing the location of monitored three-phase main primary voltage nodes.

Feeder Response with Default Load Parameters and Capacitor Sensitivity Analysis

A simulation with 75 amps of DC current flowing in the substation transformer and the default %SeriesRL setting of 50 will be examined first. The THD across all monitored nodes for this simulation is shown in Figure 4.25. The values are in general agreement with the middle range of THD values at 75 amps DC seen in Figure 4.8. The worst THDs appear on single-phase laterals near capacitor banks.

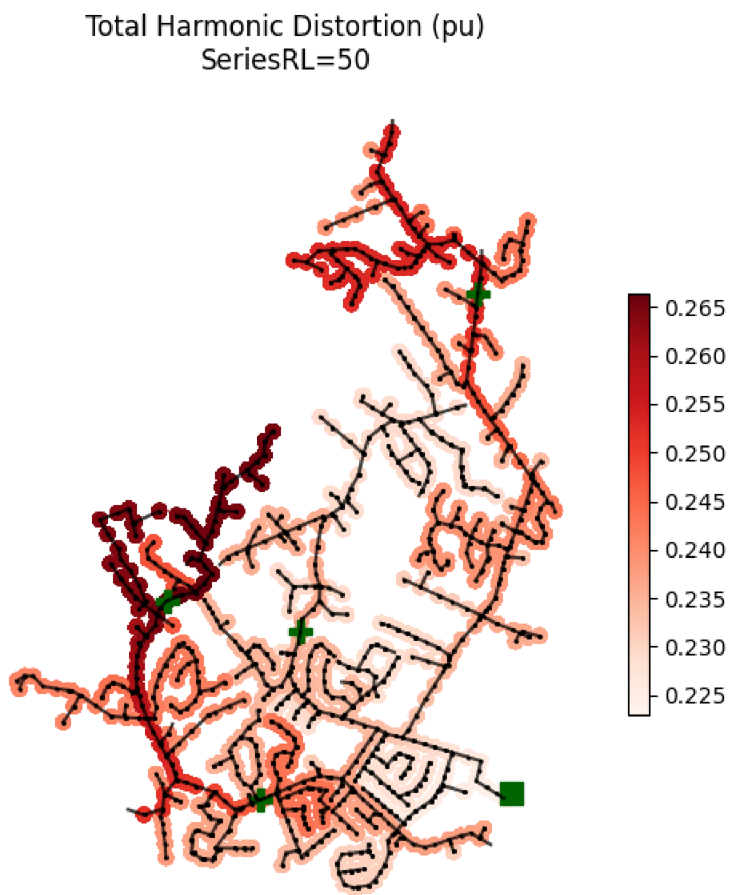

Figure 4.25.-Oneline diagram of the EPRI CKT5 model showing total harmonic distortion of the voltage in per unit along the feeder.

The waveform peak values across the feeder nodes are shown in Figure 4.26. For this simulation, none of the capacitors exceed the 1.2 per unit capacitor voltage limit. However, the impact of capacitor banks trip will be evaluated later.

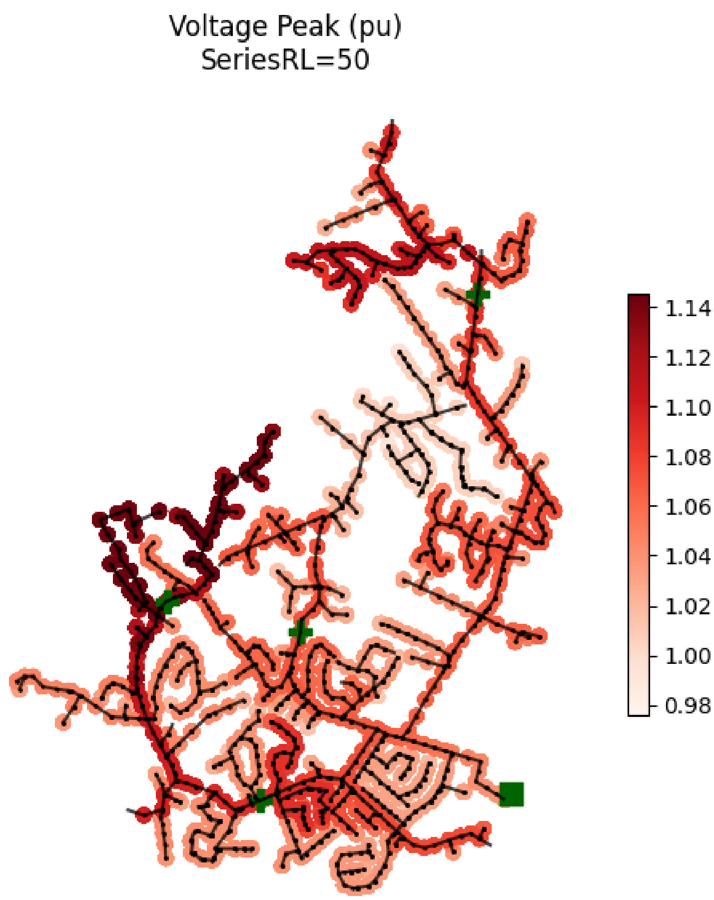

Figure 4.26.-Oneline diagram of the EPRI CKT5 model showing waveform peak voltages in per unit along the feeder.

The RMS values for the simulation are shown in Figure 4.27, where blue indicates nodes with very low RMS voltage. The blue nodes in this diagram are below the lower CBEMA voltage limit, so some load loss may be expected at these points. This is not to say that all other load are expected to ride through the event, but simply that loads near the blue nodes are less likely to ride through.

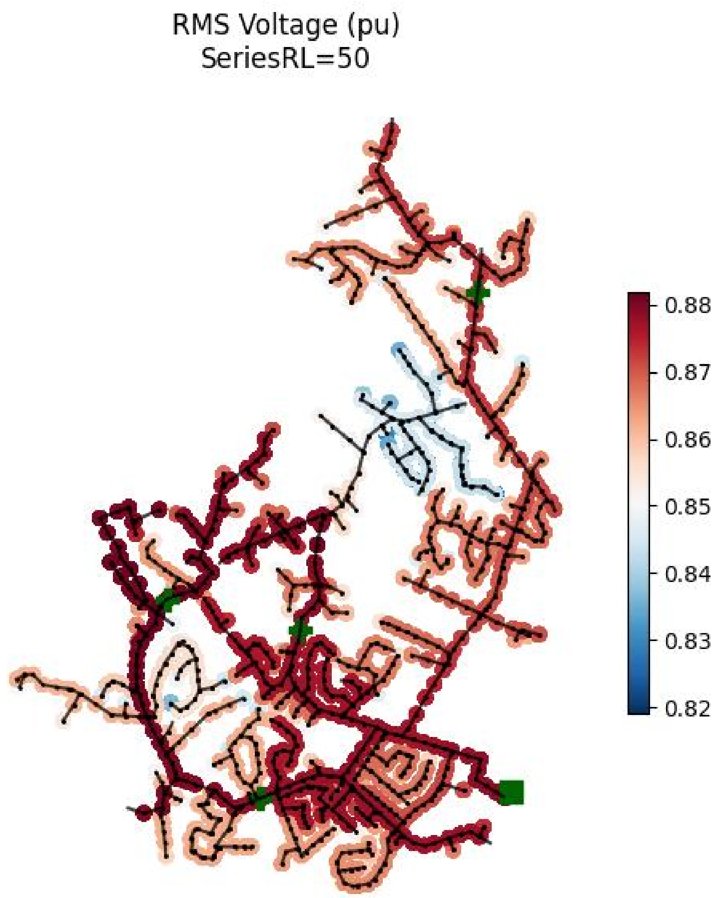

Figure 4.27.-Oneline diagram of the EPRI CKT5 model showing RMS voltages in per unit along the feeder.

The 11th harmonic voltage values for the simulation are shown in Figure 4.28. The amplification is evident in that many feeder nodes have a value about five times that of the substation, where the signal originates. Roughly two-thirds of the nodes exceed the individual harmonic limit.

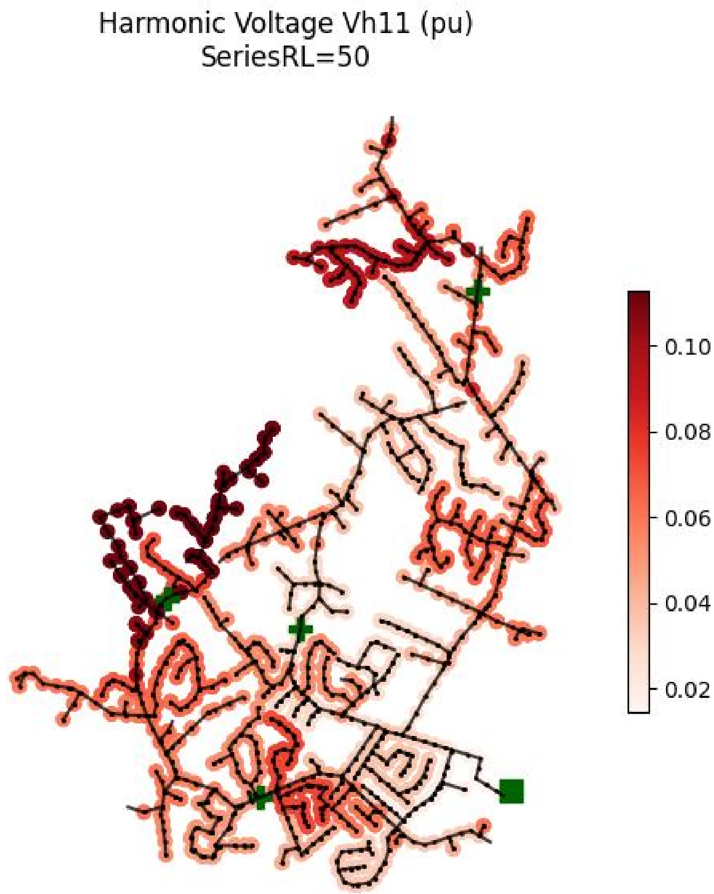

Figure 4.28.-Oneline diagram of the EPRI CKT5 model showing the 11th harmonic voltage in per unit along the feeder.

The 11th harmonic current flow is illustrated in Figure 4.29, where the thickness of each branch indicates the relative amount of current flowing. The thickness of the line was capped to practically produce this diagram, so the higher magnitude of current flowing in the substation exit branch cannot be distinguished visually. This diagram shows that most of the harmonic current flows on each three-phase primary main toward the capacitor banks.

Figure 4.29.- Oneline diagram of the EPRI CKT5 model illustrating the 11th harmonic current along branches of the feeder.

The voltage waveform at each capacitor bank is compared to that of the substation bus in Figure 4.30. The amplification of the 11th harmonic causes increased distortion of the waveform beyond that generated by the voltage source at the substation bus. The resulting increase in peak voltage is visible too.

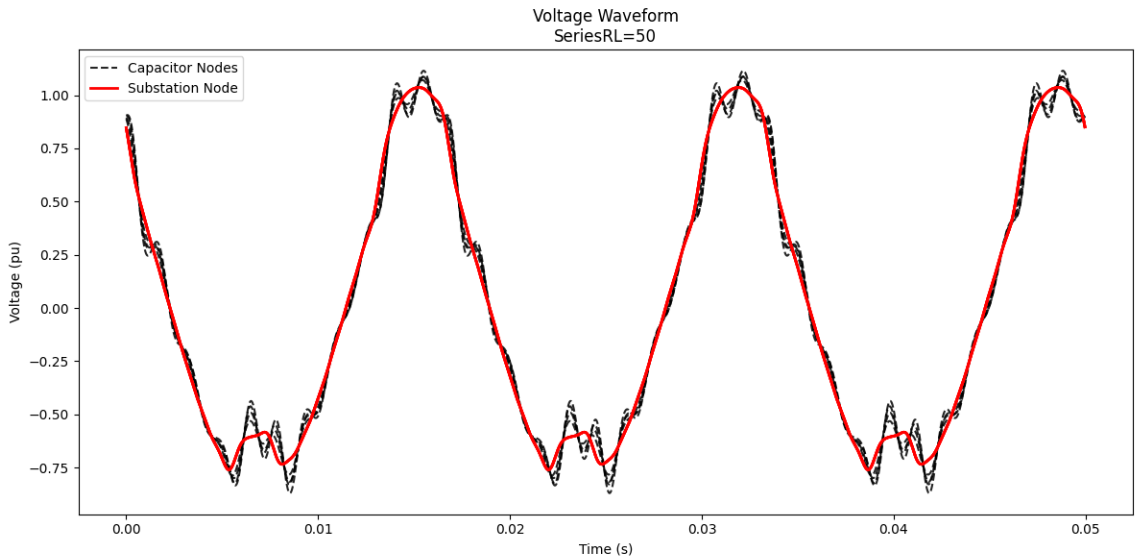

Figure 4.30.-Voltage waveforms at the substation and capacitor bank nodes within the EPRI CKT5 model.

Even though the upper voltage peak limit was not exceeded by any of the capacitor banks in this simulation, the range of values tested in the previous section indicated some possibility of capacitor loss given the right transformer parameters. Even in the absence of a trip, capacitor banks are expected to be offline at different times during the year. The impact of loss of these capacitor banks during an asymmetric saturation scenario can be understood visually in Figure 4.31 through Figure 4.36. The diagram on the right side of each figure represents the scenario with all capacitor banks removed. These side-by-side plots are on the same scale so that differences in feeder performance can be understood visually.

The reduction in 11th harmonic current and voltage along the feeder is prominent. Without the resonance condition created by the capacitor bank, the 11th harmonic voltages across the feeder vary little from the substation value and the currents are reduced. RMS voltages decrease after the capacitors are removed and more of the feeder nodes fall below the lower CBEMA voltage limit. Peak voltages reduce significantly, but the THDs remain much higher than the 5% limit. The full set of criteria are not met even without amplification brought on by capacitor banks. While still distorted, the voltage waveforms at the capacitor nodes return to the shape generated at the substation bus.

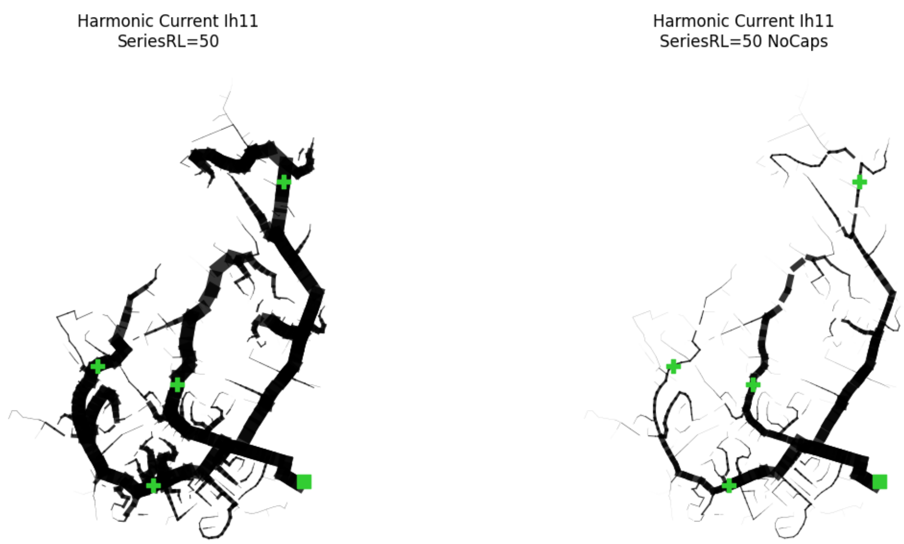

Figure 4.31.-Oneline diagram of the EPRI CKT5 model showing the 11th harmonic current magnitude along the feeder branches with and without capacitor banks online.

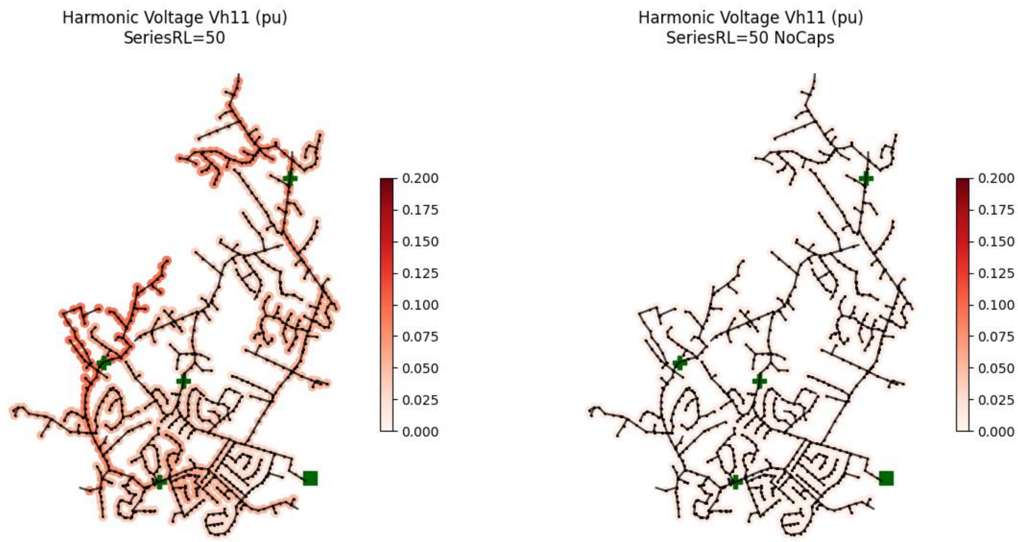

Figure 4.32.-Oneline diagram of the EPRI CKT5 model showing the 11th harmonic voltage magnitude in per unit along the feeder with and without capacitor banks online.

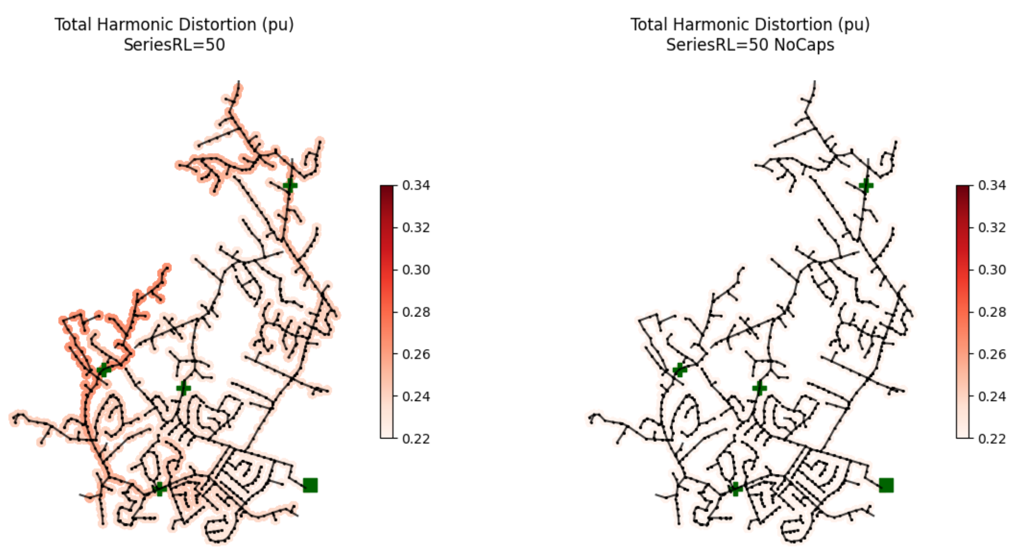

Figure 4.33.-Oneline diagram of the EPRI CKT5 model showing the voltage total harmonic distortion magnitude in per unit along the feeder with and without capacitor banks online.

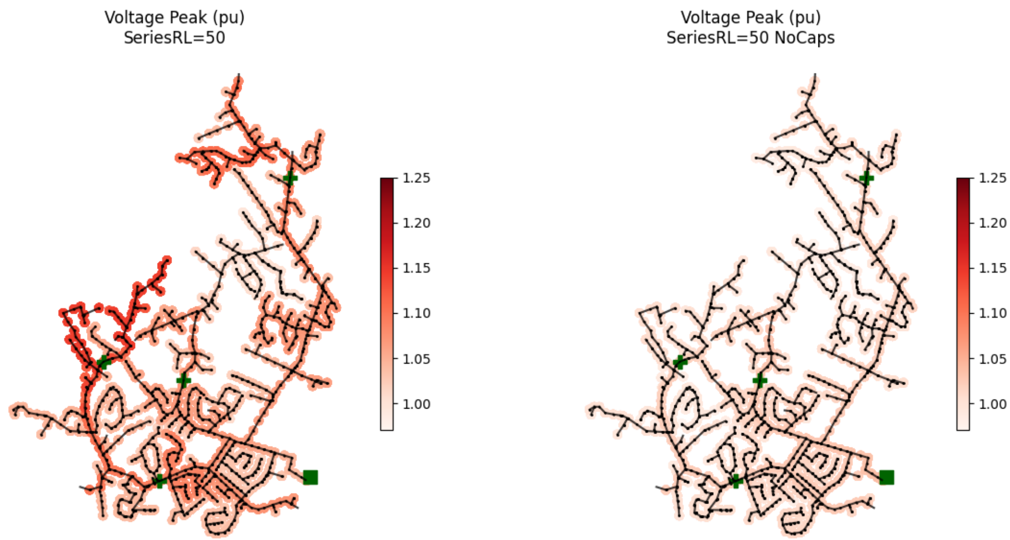

Figure 4.34.-Oneline diagram of the EPRI CKT5 model showing voltage waveform peaks in per unit along the feeder with and without loss of the capacitor banks.

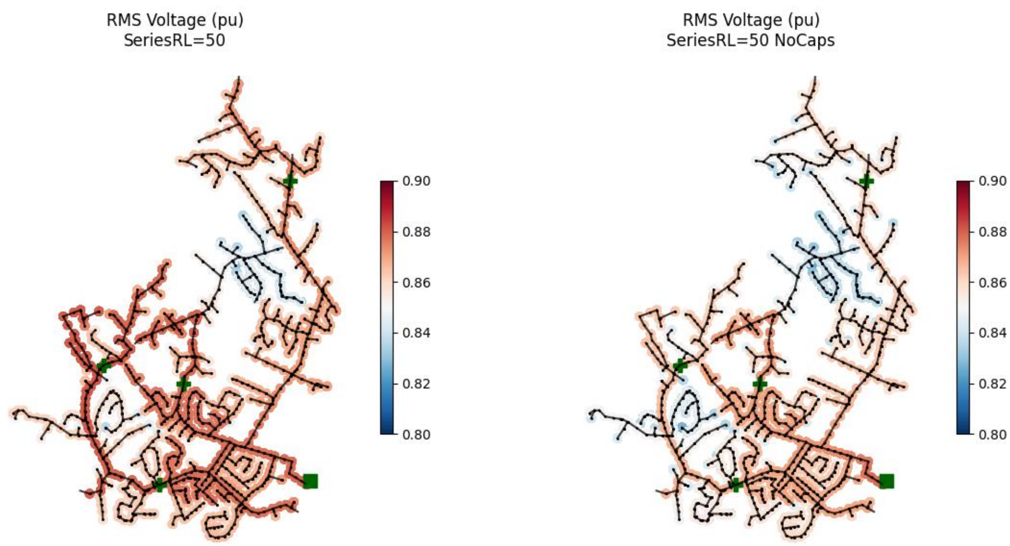

Figure 4.35.-Oneline diagram of the EPRI CKT5 model showing RMS voltages in per unit along the feeder with and without loss of the capacitor banks.

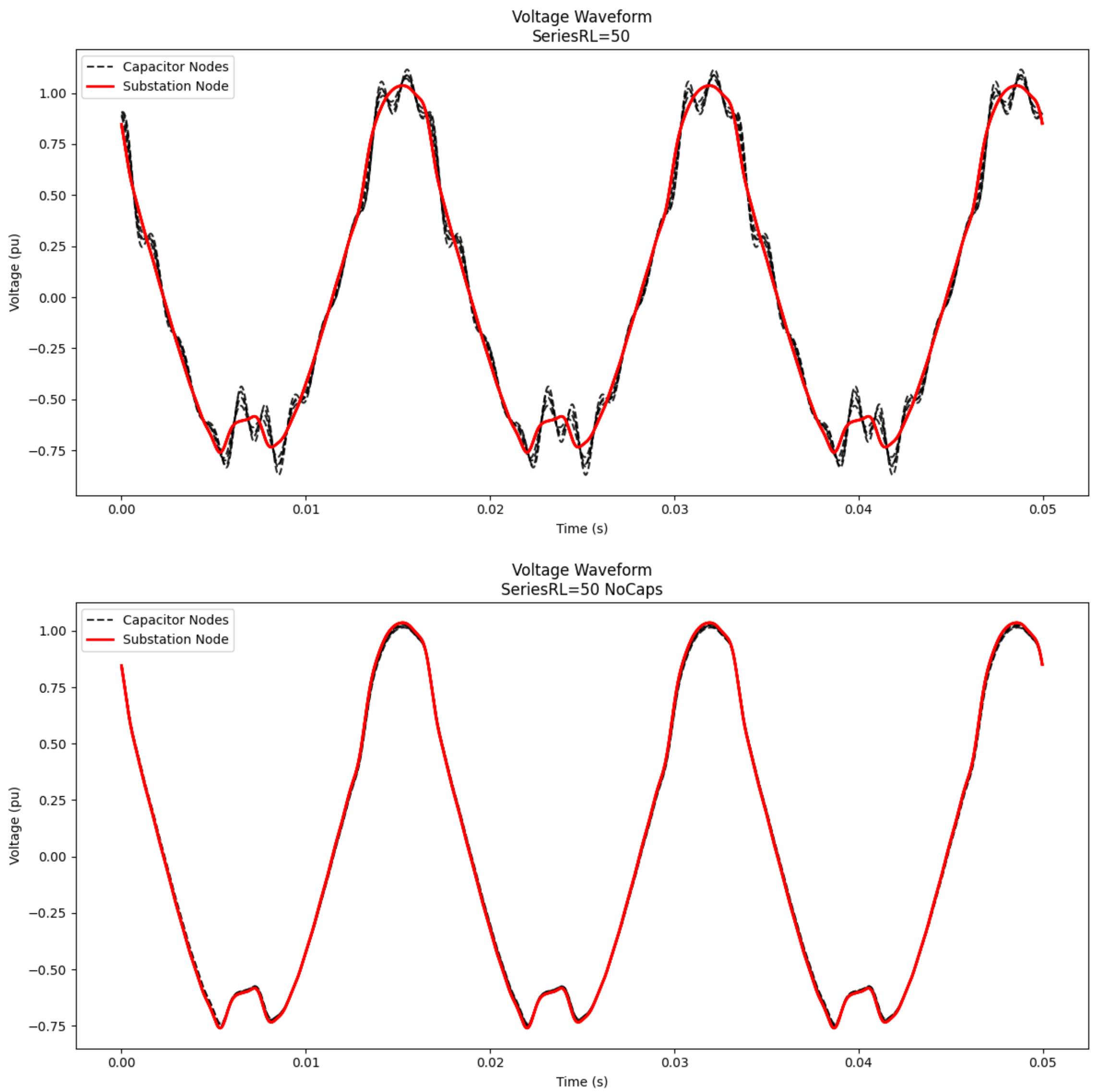

Figure 4.36.-Voltage waveforms at the substation and capacitor bank nodes within the EPRI CKT5 model with and without loss of the capacitor banks.

Harmonic Load Model Settings Sensitivity Analysis

Simulations of this 75 amp DC current scenario with capacitor banks online were performed for two sensitivity cases to evaluate the impact of the %SeriesRL setting to the harmonic simulation result. Settings of 0 and 100 were considered to evaluate performance at the boundaries of the model options. Setting the %SeriesRL setting to 0 forces the solution to use a parallel resistance and inductance to represent the load for harmonic simulations, while a setting of 100 forces a series resistance and inductance representation. The response plots for both simulations are shown side-by-side in Figure 4.37 through Figure 4.40. The color scale for each side-by-side plot is the same so that differences in the magnitude across the two simulations can be understood visually by comparing the intensity of the color.

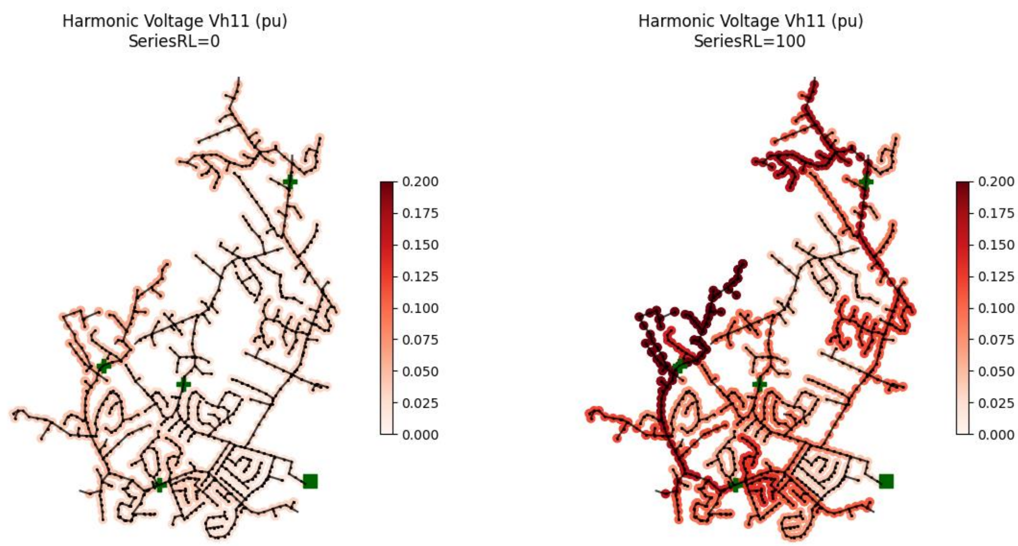

Figure 4.37.-Oneline diagram of the EPRI CKT5 model showing the 11th harmonic voltage magnitude in per unit along the feeder for different %SeriesRL load model settings.

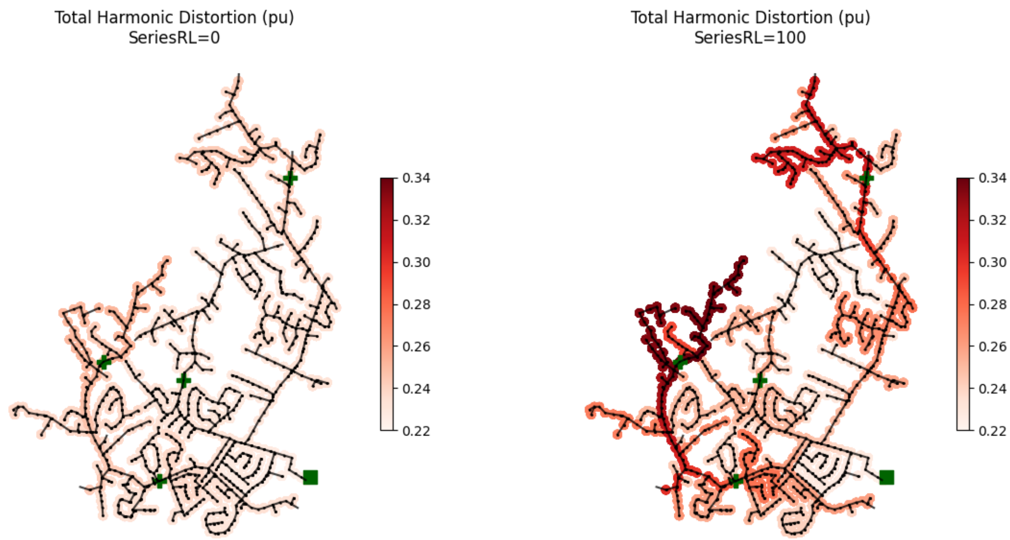

Figure 4.38.-Oneline diagram of the EPRI CKT5 model showing the voltage total harmonic distortion in per unit along the feeder for different %SeriesRL load model settings.

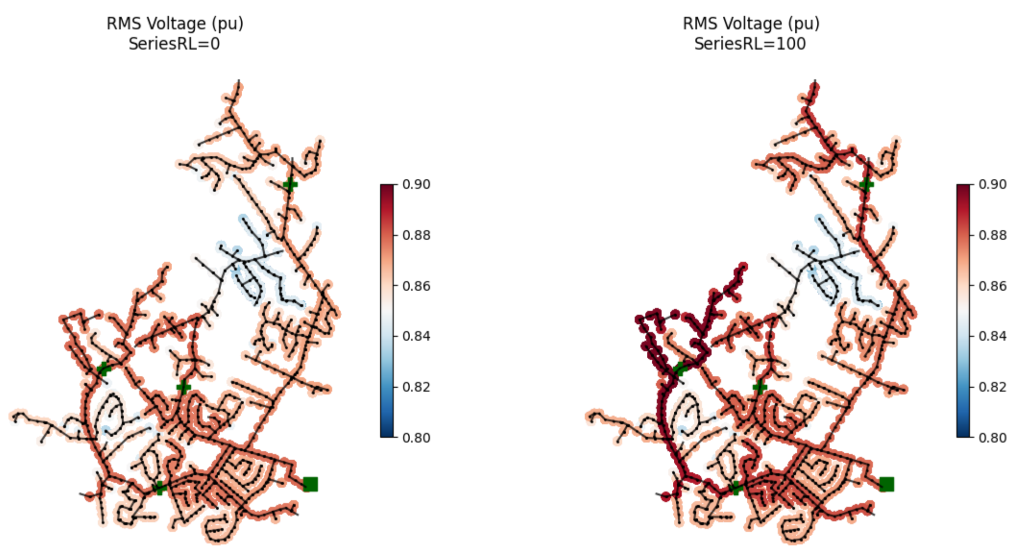

Figure 4.39.-Oneline diagram of the EPRI CKT5 model showing the RMS voltage magnitude in per unit along the feeder for different %SeriesRL load model settings.

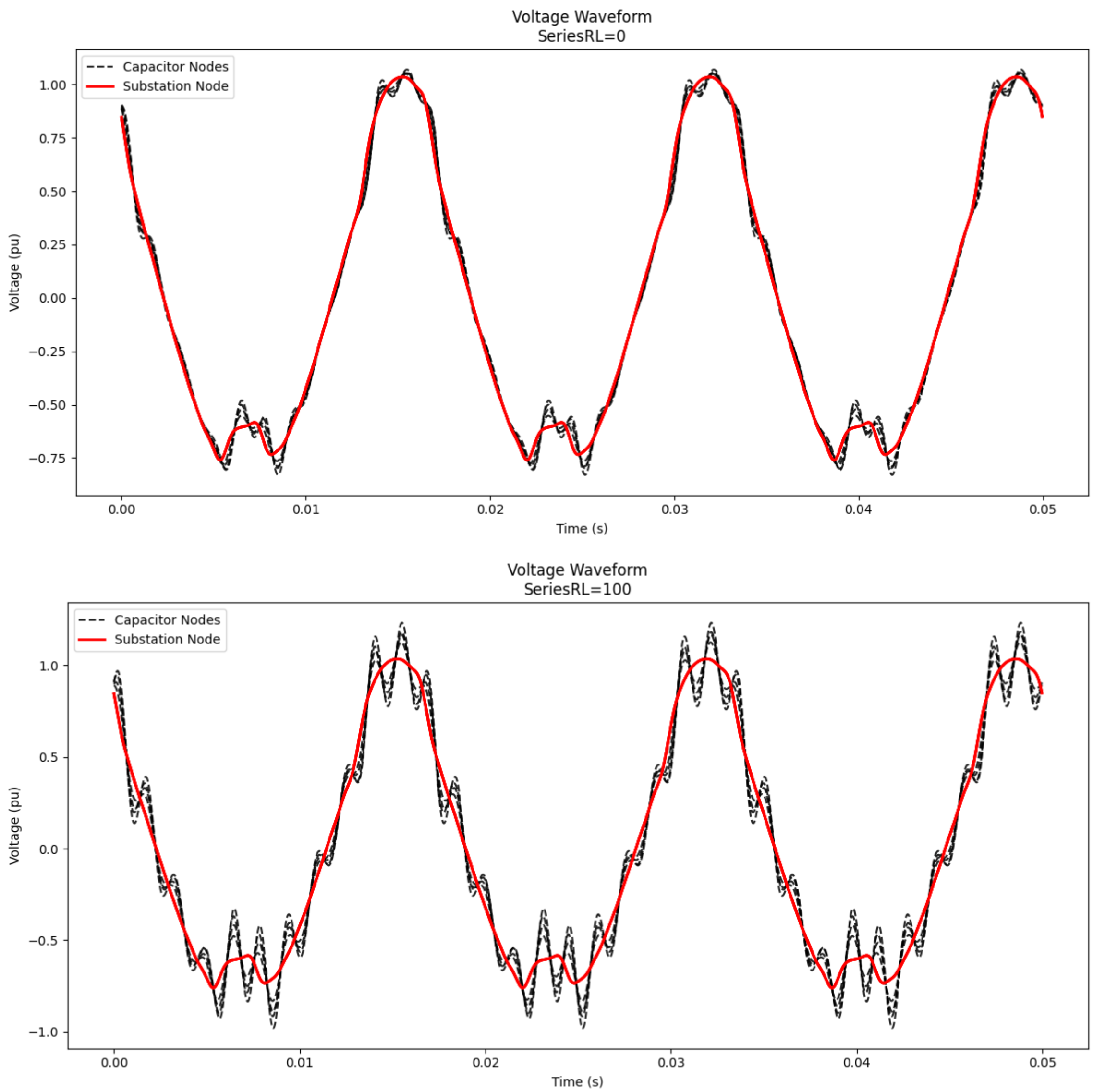

Figure 4.40.-Voltage waveforms at the substation and capacitor bank nodes within the EPRI CKT5 model for different %SeriesRL load model settings.

The sensitivity simulations show that the %SeriesRL can have a significant impact on harmonic powerflow simulation results. The simulated harmonic voltage response was worse for higher %SeriesRL settings. Most actual feeders will have a mixture of load types, which is not evaluated here. Additional work to determine appropriate load model settings may be worthwhile when assessing the harmonic response of actual feeders.

Summary

The steady-state behavior of realistic feeders was examined using powerflow simulation and the transformer secondary terminal voltage source model developed earlier. The simulations were performed to account for DC current flowing in the transformer high-side winding up to 75 amps per phase. Both the individual harmonics and the total harmonic distortion exceeded the IEEE limits in all of the EPRI CKT models examined, and usually at a fairly low value of DC current. Distortion amplification was observed for harmonics overlapping with the feeder resonant points identified using harmonic frequency scans.

One of the distribution system models showed significant distortion amplification and general voltage issues in response to 75 amps of DC current flowing in substation transformer. Apart from the IEEE harmonic limits, the other two distribution system models evaluated showed little exposure up to 75 amps of DC current with respect to the other criteria examined here. Due to the difference in substation transformer high-side current ratings, each transformer evaluated incurred different levels of saturation for the 75 amps of DC current considered. The distribution system substation with the lowest rating exhibited the worst performance.

Sensitivity analysis was performed to assess the influence that capacitor banks and harmonic load model settings have on the simulation results. The impact of harmonic load model settings was evaluated by performing simulations while changing the %SeriesRL setting, and this setting was observed to have a significant impact on the harmonic powerflow simulation results. The presence of capacitor banks was observed to have significant impact on the magnitude of harmonic current flowing out of the voltage source, which caused distortion in the waveforms to be amplified.

CHAPTER FIVE

Conclusion and Future Work

Conclusion

This research was performed to approximate distribution substation transformer secondary voltage response to high-side DC currents and to examine the resulting distribution feeder response. Test measurement data provided for this work were analyzed and used to evaluate the ability of harmonic powerflow simulation to represent the energization of loads by an asymmetrically saturated transformer using a harmonic voltage source, and to guide the development of a more general model. The harmonic voltage source approach was able to produce a reasonable estimate of the harmonic response of the feeder as compared to the field test measurements.

Using the basic relationships inherent in transformer operation and combining the method published in [25] and [26] with the flux-linkage current relationship in [5], a model was developed to approximate the non-linear transformer magnetizing current as a function of DC current flowing in each phase of the substation transformer high-side winding. The magnetizing current source was combined with the transformer t-model to approximate the secondary terminal response of the transformer. The model response was qualitatively compared with field test measurements, where it was found to produce secondary terminal response with similar characteristics to those observed in the field test data.

The steady-state behavior of realistic feeders was examined using harmonic powerflow simulation and the transformer secondary terminal voltage source model developed earlier. Harmonic voltage amplification was observed for harmonics overlapping with feeder resonant points, and the IEEE standard limits for harmonics were exceeded in all test cases. While RMS voltages fell outside of normal operating limits for two of the test cases, this was only observed for a portion of the transformer parameters considered and for fairly magnitudes of high-side DC current. The impact of harmonic load model settings and the presence of capacitor banks were both observed to have a significant impact on the simulation results.

The model developed here cannot represent the complete variety of power transformers in actual operation today. Transformer core and winding configuration influence the transformer response to asymmetric core saturation, so the studies performed in this research may only be representative of a subset of the possible outcomes in an actual power system. Variation in magnetic core configuration of transformers can produce different saturation characteristics than those evaluated here. In addition, substation transformers with a delta connected primary winding will not be exposed to significant high-side DC current as examined here. Therefore, the results obtained using this model are unable to represent the variety of transformer responses that may occur in an actual power system but represent the kinds of feeder response that may occur for one type of transformer.

Potential Future Work

The method and results presented here may be further developed by the following potential future work.

- The response of loads served by the distribution system with respect to waveform distortion are not well known. Of particular interest are the damage limits and drop-out limits of common end-use equipment. Lab testing could be performed to identify approximate boundaries, which would provide more specific criteria for use in harmonic analysis. This would also provide insight for selecting appropriate load model settings for use in harmonic powerflow simulations.
- The impacts of distributed energy resources (DER), power generation resources connected to the distribution system, were not considered in this work. As the amount of DER continue to grow, these resources are becoming more important to the operation of bulk power systems. Evaluation of DER response during E3 or GMD events may be necessary to ensure reliable operation of the system during events causing significant DC currents to flow in the transmission grid.
- The steady-state asymmetrically saturated transformer secondary terminal model developed here could be improved to broaden the use cases. Explicit inclusion of magnetic circuits in this model would allow for representation of different transformer core types and the associated secondary terminal response. Validating the model at DC currents beyond 2 per unit is recommended, especially if continued work on power system response to E3 reveals a likelihood of values much higher than 75 amps per phase. Development to include the effects of hysteresis in the transformer core and distortion of the flux-linkage may allow additional approximations to be made, such as the real power losses of transformers during asymmetric saturation.

REFERENCES

[1] L. Bolduc, “GIC observations and studies in the Hydro-Québec power system,” *J. Atmospheric Sol.-Terr. Phys.*, vol. 64, no. 16, pp. 1793–1802, Nov. 2002, doi: 10.1016/S1364-6826(02)00128-1.

[2] B. Magness, “Review of February 2021 Extreme Cold Weather Event – ERCOT Presentation,” p. 23.

[3] J. R. Legro, N. C. Abi-Samra, J. C. Crouse, and F. M. Tesche, “A Methodology to Assess the Effects of Magnetohydrodynamic Electromagnetic Pulse (MHD-EMP) on Power Systems,” *IEEE Trans. Power Deliv.*, vol. 1, no. 3, pp. 203–210, Jul. 1986, doi: 10.1109/TPWRD.1986.4307994.

[4] “Volume II Recommended E3 HEMP Heave Electric Field Waveform for the Critical Infrastructures | Technical Resources,” *ASPR TRACIE*. https://asprtracie.hhs.gov/technical-resources/resource/5962/volume-ii-recommended-e3-hemp-heave-electric-field-waveform-for-the-critical-infrastructures (accessed Oct. 09, 2022).

[5] M. Salimi, A. M. Gole, and R. P. Jayasinghe, “Improvement of Transformer Saturation Modeling for Electromagnetic Transient Programs,” *Int. Conf. Power Syst. Transients*, p. 6.

[6] M. Lahtinen and J. Elovaara, “GIC occurrences and GIC test for 400 kV system transformer,” *IEEE Trans. Power Deliv.*, vol. 17, no. 2, pp. 555–561, Apr. 2002, doi: 10.1109/61.997938.

[7] F. M. Tesche, P. R. Barnes, and A. P. S. Meliopoulos, “Magnetohydrodynamic electromagnetic pulse (MHD-EMP) interaction with power transmission and distribution systems,” Oak Ridge National Lab., TN (United States); Georgia Inst. of Tech., Atlanta, GA (United States). Dept. of Electrical Engineering, ORNL/Sub-90-SG828/1, Feb. 1992. doi: 10.2172/5559195.

[8] A. P. S. Meliopoulis, *Power System Grounding and Transients: An Introduction*. Marcel Dekker, Inc., 1988.

[9] V. J. Kruse, G. B. Rackliffe, and P. R. Barnes, “Load flow studies in the presence of magnetohydrodynamic electromagnetic pulse,” *IEEE Trans. Power Deliv.*, vol. 5, no. 2, pp. 1158–1163, Apr. 1990, doi: 10.1109/61.53135.

[10] T. J. Overbye, J. Snodgrass, A. Birchfield, and M. Stevens, “Towards Developing Implementable High Altitude Electromagnetic Pulse E3 Mitigation Strategies for Large-Scale Electric Grids,” in *2022 IEEE Texas Power and Energy Conference (TPEC)*, Feb. 2022, pp. 1–6. doi: 10.1109/TPEC54980.2022.9750778.

[11] N. Mohan, J. G. Kappenman, and V. D. Albertson, “Harmonics and Switching Transients in the Presence of Geomagnetically-Induced Currents,” *IEEE Trans. Power Appar. Syst.*, vol. PAS-100, no. 2, pp. 585–593, Feb. 1981, doi: 10.1109/TPAS.1981.316915.

[12] D. P. Carroll, S. Kasturi, M. Subudhi, and W. Gunther, “Harmonic effects of solar geomagnetically induced currents on the electrical distribution system in nuclear power plants,” Brookhaven National Lab., Upton, NY (United States), BNL-NUREG-48242; CONF-921007-16, Jan. 1992. Accessed: Oct. 14, 2022. [Online]. Available: https://www.osti.gov/biblio/6921107

[13] “Assessment Guide: Geomagnetic Disturbance Harmonic Impacts and Asset Withstand Capabilities.” https://www.epri.com/research/products/000000003002017707 (accessed Oct. 11, 2022).

[14] J. W. Nilsson and S. A. Riedel, *Electric Circuits*, Eighth Edition. Pearson/Prentice Hall, 2008.

[15] C. P. Steinmetz, *Theory and Calculation of Alternating Current Phenomena*. W. J. Johnston Company, 1897. [Online]. Available: https://books.google.com/books?id=YrseAAAAMAAJ

[16] D. G. Zill, W. S. Wright, and M. R. Cullen, *Advanced Engineering Mathematics*, Fourth Edition. Jones & Bartlett Learning, 2011.

[17] A. E. Fitzgerald, C. Kingsley, and S. D. Umans, *Electric Machinery*, Fifth Edition. McGraw-Hill, 1990.

[18] T. J. Aprille and T. N. Trick, “Steady-state analysis of nonlinear circuits with periodic inputs,” *Proc. IEEE*, vol. 60, no. 1, pp. 108–114, Jan. 1972, doi: 10.1109/PROC.1972.8563.

[19] F. B. Grosz and T. N. Trick, “Some Modifications to Newton’s Method for the Determination of the Steady-State Response of Nonlinear Oscillatory Circuits,” *IEEE Trans. Comput.-Aided Des. Integr. Circuits Syst.*, vol. 1, no. 3, pp. 116–120, Jul. 1982, doi: 10.1109/TCAD.1982.1270002.

[20] A. Ushida, T. Adachi, and L. O. Chua, “Steady-state analysis of nonlinear circuits based on hybrid methods,” *IEEE Trans. Circuits Syst. Fundam. Theory Appl.*, vol. 39, no. 8, pp. 649–661, Aug. 1992, doi: 10.1109/81.168917.

[21] J. L. Blackburn, *Symmetrical Components for Power Systems Engineering*. CRC Press, 1993.

[22] A. Greenwood, *Electrical Transients in Power Systems*, Second Edition. John Wiley & Sons, Inc., 1991.

[23] "The Classical Approach." https://www.pscad.com/webhelp/EMTDC/Transformers/The_Classical_Approach/the_classical_approach.htm#More (accessed Jan. 16, 2023).

[24] J. D. Kraus and D. A. Fleisch, *Electromagnetics: With Applications*, Fifth Edition. WCB/McGraw-Hill, 1999.

[25] D. H. Boteler, R. M. Shier, T. Watanabe, and R. E. Horita, "Effects of geomagnetically induced currents in the BC Hydro 500 kV system," *IEEE Trans. Power Deliv.*, vol. 4, no. 1, pp. 818–823, Jan. 1989, doi: 10.1109/61.19275.

[26] R. A. Walling and A. N. Khan, "Characteristics of transformer exciting-current during geomagnetic disturbances," *IEEE Trans. Power Deliv.*, vol. 6, no. 4, pp. 1707–1714, Oct. 1991, doi: 10.1109/61.97710.

[27] A. V. Oppenheim, R. W. Schafer, and J. R. Buck, *Discrete-time Signal Processing*, Second Edition. Prentice Hall, 1999.

[28] C. R. Harris *et al.*, "Array programming with NumPy," *Nature*, vol. 585, no. 7825, Art. no. 7825, Sep. 2020, doi: 10.1038/s41586-020-2649-2.

[29] A. R. Bergen and V. Vittal, *Power Systems Analysis*, Second Edition. Prentice-Hall, Inc., 2000.

[30] "EPRI | Smart Grid Resource Center > Simulation Tool – OpenDSS." https://smartgrid.epri.com/SimulationTool.aspx (accessed Oct. 08, 2022).

[31] "p/electricdss/code - Revision 3517: /trunk/Distrib/Doc." http://svn.code.sf.net/p/electricdss/code/trunk/Distrib/Doc/ (accessed Oct. 09, 2022).

[32] M. Grady, "Understanding Power System Harmonics," p. 181, 2012.

[33] "IEEE SA - IEEE 519-2022," *IEEE Standards Association*. https://standards.ieee.org/ieee/519/10677/ (accessed Oct. 09, 2022).

[34] "IEEE SA - IEEE 446-1995," *IEEE Standards Association*. https://standards.ieee.org/ieee/446/669/ (accessed Oct. 09, 2022).

[35] "IEEE SA - IEEE 18-2012," *IEEE Standards Association*. https://standards.ieee.org/ieee/18/4343/ (accessed Oct. 09, 2022).

[36] “Current Planning Guide.” https://www.ercot.com/mktrules/guides/planning/current (accessed Oct. 09, 2022).

[37] W. M. Grady, “Field Test Data.” unpublished, 2022.

[38] M. Rooney, D. Fromme, G. Edmiston, A. Walker, S. West, and S. McBride, “Dtra mhd-e3 phase ivb measured harmonic response of power grid transformers subjected to severe e3/gic currents,” Defense Threat Reduction Agency, 2013. [Online]. Available: https://www.swpc.noaa.gov/sites/default/files/images/u33/INL_GMD_Measured_Harmonic_Response-Public_Release_NOAA.pdf

[39] “Mhd-e3 transmission level power grid test report part i - phase iv test description,” Defense Threat Reduction Agency, Report DTRA-TR-15-46, 2013.

[40] “Mhd-e3 transmission level power grid test report part ii - phase iv test results,” Defense Threat Reduction Agency, Report DTRA-TR-15-47, 2013.

[41] L. Bolduc, A. Gaudreau, and A. Dutil, “Saturation time of transformers under dc excitation,” *Electr. Power Syst. Res.*, vol. 56, no. 2, pp. 95–102, Nov. 2000, doi: 10.1016/S0378-7796(00)00087-0.

[42] J. Arrillaga and N. R. Watson, *Power System Harmonics*, Second Edition. John Wiley & Sons, Ltd, 2003.

[43] R. C. Dugan, M. F. McGranaghan, and H. W. Beaty, *Electrical Power Systems Quality*. McGraw-Hill, 1996.

[44] W. D. Stevenson, *Elements of Power System Analysis*, Second Edition. McGraw-Hill Book Company, Inc., 1962.

[45] A. Ovalle, R. C. Dugan, and R. F. Arritt, “GICharm: A System Level Analysis Tool for Geomagnetic Disturbance Related Harmonics,” *IEEE Trans. Ind. Appl.*, vol. 58, no. 2, pp. 1406–1415, Mar. 2022, doi: 10.1109/TIA.2022.3145770.

[46] R. H.-W. Lee, K. S. Shetye, A. B. Birchfield, and T. J. Overbye, “Using Detailed Ground Modeling to Evaluate Electric Grid Impacts of Late-Time High-Altitude Electromagnetic Pulses (E3 HEMP),” *IEEE Trans. Power Syst.*, vol. 34, no. 2, pp. 1549–1557, Mar. 2019, doi: 10.1109/TPWRS.2018.2878533.

[47] “p/electricdss/code - Revision 3595: /trunk/Distrib/Examples/FreqScan.” http://svn.code.sf.net/p/electricdss/code/trunk/Distrib/Examples/FreqScan/ (accessed Feb. 26, 2023).

[48] R. C. Dugan, M. F. McGranaghan, S. Santoso, and H. W. Beaty, *Electrical Power Systems Quality*, Third Edition. McGraw Hill, 2012.